UNIVERSITÀ DEGLI STUDI DI PADOVA

UNIVERSITÀ DEGLI STUDI DI PADOVA

Dipartimento di Ingegneria Industriale DII

Corso di Laurea Magistrale in Ingegneria dell'Energia Elettrica

ANALYSIS OF SHUNT CURRENT EFFECTS AND REDUCTION METHODS IN VANADIUM FLOW BATTERIES

Relatore: Prof. Andrea Trovò

Laureando: Mirco Passarella

Anno Accademico 2023/2024

Sommario

La progettazione di una batteria a flusso richiede un approccio multidisciplinare che coinvolge competenze in ingegneria elettrica, elettrochimica, chimica e modellazione numerica. Svariati fenomeni influenzano le prestazioni dello stack, tra cui le correnti di shunt e le perdite idrauliche, che devono essere ridotte al minimo. Le correnti di shunt sono generate dalle differenze di potenziale elettrico tra le celle, che spingono le specie cariche lungo i canali di flusso verso celle adiacenti, provocando correnti elettriche indesiderate (conosciute come "shunt") e le relative perdite dovute all'effetto Joule.

La tesi descrive un'analisi dettagliata del fenomeno delle correnti di shunt nelle batterie a flusso, i loro effetti sulle performance di sistemi industriali e le soluzioni volte alla loro mitigazione attraverso una ricerca brevettuale e commerciale.

La prima parte della tesi approfondisce i meccanismi fisico/chimici alla base delle correnti di shunt e gli effetti negativi sulle performance di batterie a flusso di vanadio. In particolare, si è esaminato come tali correnti possono variare in base alle specifiche del sistema e alle sue condizioni di funzionamento con riferimento alle indesiderate cadute di tensione, generazione interna di calore e riduzione dell'efficienza complessiva.

Nella seconda parte si sono analizzati i principali brevetti e articoli disponibili nelle banche dati accessibili dall'Università degli Studi di Padova assieme alle varie soluzioni commerciali che i produttori di batterie a flusso propongono. Ciascuna fonte è stata analizzata in modo critico, sia dal punto di vista del principio fisico di funzionamento e sia dal punto di vista della sua effettiva applicabilità in sistemi industriali. Questo lavoro ha inoltre fornito spunti concreti su ulteriori idee volte a mitigare il fenomeno.

Abstract

The flow battery design requires a multidisciplinary approach involving expertise in electrical engineering, electrochemistry, chemistry and numerical modeling. Various phenomena affect stack performance, including shunt currents and hydraulic losses, which must be minimized. Shunt currents are generated by differences in electrical potential between cells, which push charged species along flow channels towards adjacent cells, causing unwanted electrical currents ("shunts currents") and related losses due to the Joule effect.

The thesis describes a detailed analysis of the phenomenon of shunt currents in flow batteries, their effects on the performance of industrial systems and the solutions aimed at their mitigation through patent and commercial research.

The first part of the thesis delves into the physical/chemical mechanisms underlying shunt currents and the negative effects on the performance of vanadium flow batteries. In particular, it was examined how these currents can vary based on the specifications of the system and its operating conditions with reference to unwanted voltage drops, internal heat generation and reduction in overall efficiency.

In the second part, the main patents and articles available in the databases accessible by the University of Padua were analyzed together with the various commercial solutions that flow battery manufacturers propose. Each source was critically analyzed, both from the point of view of the physical operating principle and from the point of view of its actual applicability in industrial systems. This work also provided concrete insights into further ideas aimed at mitigating the phenomenon.

Contents

1. Introduction

One of the key factors in the evolution of humankind is energy; all industrial infrastructures need energy. However, in the last few decades, we have realized that anthropic activities cause dangerous emissions of greenhouse gases into the atmosphere that may compromise the environment of the earth. Unfortunately, the energy sector is one of the main contributors to carbon dioxide (the main greenhouse gas emitted through human activities) emissions, as shown in the following chart:

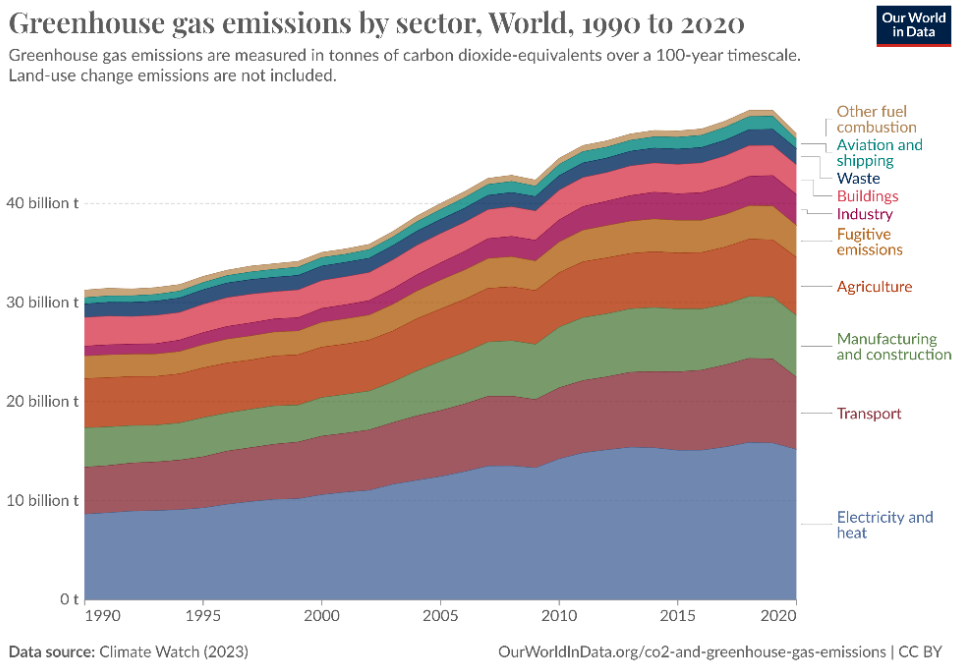

Figure 1.1: Carbon dioxide emissions 1990-2020. Source: Our World in Data

Figure 1.1 provides a clear statement: the electricity and heat sectors emitted in 2020 around 15 billion tones equivalent of CO_2.

This is the reason why, in recent years and at present, the objective worldwide is to switch to clean energy sources, mainly wind and solar energy, but also biofuels and nuclear energy. This is not necessarily true for all the countries, due to socio-political reasons. For example, developing countries tend to use more fossil fuels than developed ones, or in some countries, nuclear power plants are deemed unsafe by the public. Besides all of these, the trend is towards renewables.

According to Eurostat, in the European Union in 2021, renewable energy had the highest share of primary energy production (43.2%), followed by nuclear energy (27.6%). In the last decade, traditional energy sources in the EU, like fossil fuels and natural gas, have seen a significant decrease (-38.7% and -64.9% respectively), and the opposite can be said for renewable energy sources (+32.6%). The following chart shows this trend:

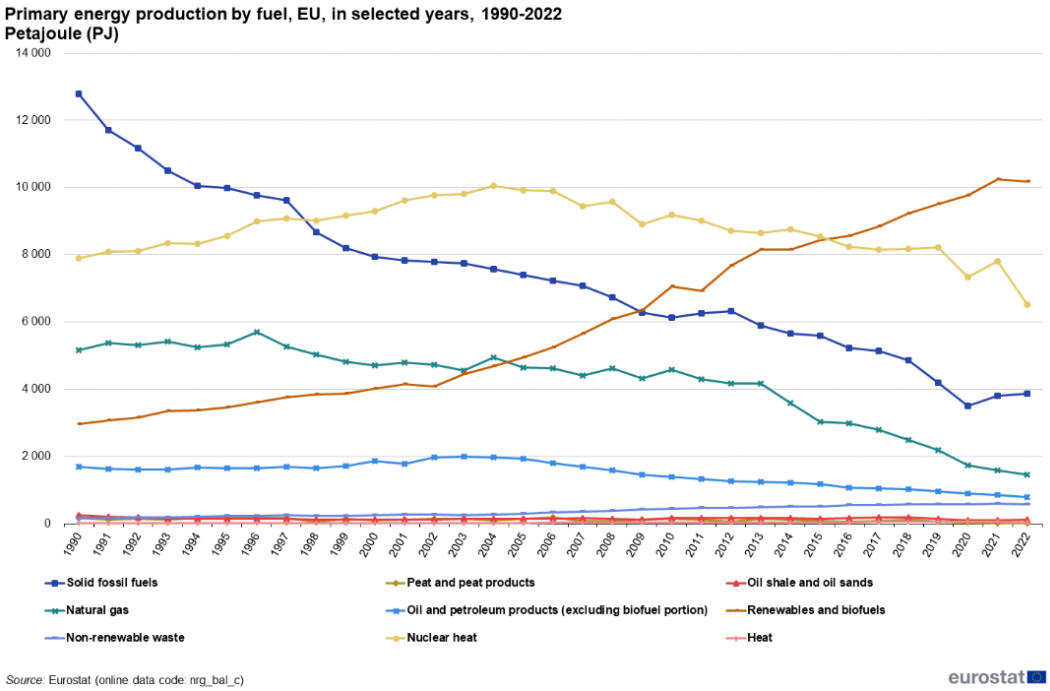

Figure 1.2: Primary energy production in the EU. Source: Eurostat

But in a world where the production of energy is more than ever achieved thanks to renewable energy sources, new solutions are necessary to provide stability and continuity to the services offered by the electrical grid. The non-continuity of wind and solar energy generation highlights the mismatch between production and the request for energy. In this scenario, one of the main solutions to this issue is the implementation of energy storage systems.

2. Energy storage systems

2.1 Types of energy storage systems

When it comes to energy storage systems (ESSs), the multitude of solutions available is outstanding. However, there is still work to be done when it comes to the efficiency and, most importantly, the longevity of the presently available technology.

There are different types of energy storage systems, and they are differentiated by the methods used to store energy. The following are presented:

- Electrical or electrochemical energy storage

  This category includes the most commonly used and known batteries, in which energy is stored thanks to a reversible chemical reaction. Other technologies are supercapacitors and superconducting magnets (SMES).

- Thermal energy storage (TES)

  Usually, this type of storage can store excess thermal energy from solar or other renewable sources, industrial processes, for example, in a combined plant, or even during periods of low demand to be used during peak demand periods.

- Mechanical energy storage

  Mechanical energy storage includes pumped storage hydropower (PSH), for example, hydroelectric power plants; then there are also flywheels and compressed air energy storage (CAES).

Of all the above-mentioned ESSs, the focus worldwide is on batteries, since they are the most promising technology for many reasons.

2.2 Batteries

The rise in interest in the energy storage industry is demonstrated by the increasing investment in the field. This is due to the fact that nowadays batteries are present in countless devices (cellphones, laptops, etc.), the switch of the automotive industry to hybrid and electric vehicles, and also the pairing of energy storage with wind turbines and photovoltaic plants in order to provide a continuous energy source to the grid.

In 2022, the European Union saw a new deployment of utility-scale energy storage of 3.3 GWh, and the International Energy Agency (IEA) estimated an increase from 2023 to 2028 of 56% of the global storage capacity. In the following charts, provided by the World Energy Investment 2024 [1], it is possible to see the rapid increase in investments in battery storage:

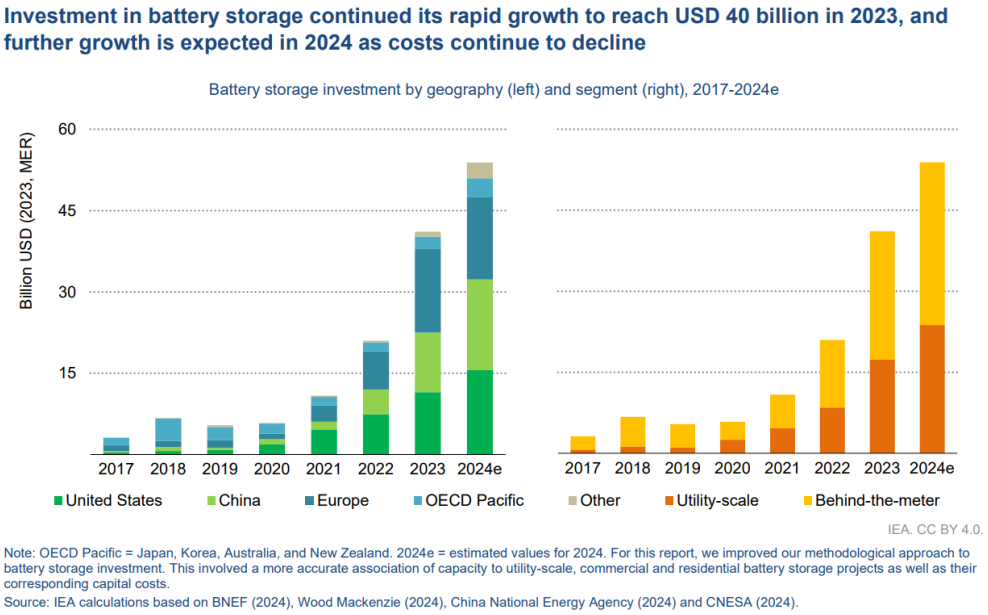

Figure 2.1: Investment in batteries 2017-2024 [1]

In today's world, technology heavily depends on batteries, which provides portable energy for electronic devices. These batteries are essential for powering gadgets like laptops and smartphones, as well as critical equipment such as electric vehicles and medical devices. Understanding the types of batteries is important not only for keeping up with advancements in energy storage technology that drive innovation across industries but also for choosing the most suitable power supply based on specific needs.

Battery storage is characterized by many different technological approaches, many of which are differentiated by the chemical reactions that occur. First and foremost, there are two macrocategories of batteries: primary and secondary batteries. Primary batteries are single-use batteries that cannot be recharged. Once depleted, they must be disposed of and replaced. They are typically used in devices with low power consumption or infrequent use. On the other hand, secondary batteries are rechargeable, making them suitable for applications where long-term cost-effectiveness and sustainability are important. A synthetic listing of all the different types of batteries is now presented:

- Alkaline battery

  Widely used in household items like remote controls, flashlights, and clocks. They are known for their long shelf life and reliability.

- Lithium battery

  Used in high-energy-demand devices such as cameras and medical equipment. They have a higher energy density and a longer life compared to alkaline batteries.

- Lithium-ion (Li-ion) battery

  Dominant in portable electronics and electric vehicles due to their high energy density, lightweight, and long cycle life. They have revolutionized the tech industry by enabling longer device runtimes and faster charging.

- Nickel-metal hydride (NiMH) battery

  Often found in rechargeable household batteries and hybrid vehicles. They are environmentally friendly and have a moderate energy density.

- Lead-acid battery

  Used primarily in automotive starter batteries and backup power systems. They are cost-effective and reliable, but heavy and less energy-dense compared to other rechargeable batteries.

- Nickel-cadmium (NiCd) battery

  Known for their robustness and ability to deliver high discharge rates. Commonly used in power tools, emergency lighting, and aviation.

- Zinc-air battery

  Primarily used in hearing aids and other medical devices. They have a high energy density and are lightweight.

- Silver oxide battery

  Utilized in small electronic devices like watches, calculators, and some medical devices due to their stable output voltage and compact size.

- Solid-state battery

  Promise higher energy densities, faster charging times, and improved safety compared to liquid electrolyte batteries.

- Flow battery

  Ideal for large-scale energy storage systems due to their scalability and ability to provide long-duration energy storage.

- Lithium-sulfur (Li-S) battery

  Potentially offer higher energy densities than Li-ion batteries, which could extend the range of electric vehicles and other applications.

Considering what was just mentioned, the market is mainly dominated by lithium-ion batteries, due to their use in electronic devices, and by lead-acid batteries, used in the automotive industry. In the following chart, it is possible to see the market size of each battery type:

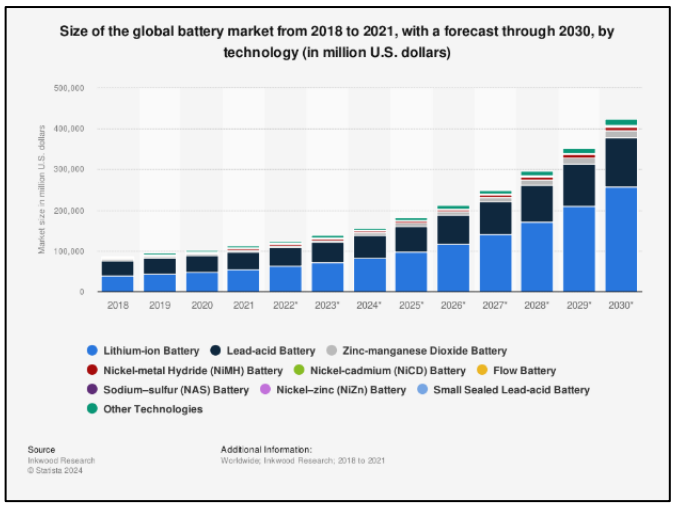

Figure 2.2: Market size of the different types of batteries 2018-2021. Source: Statista

Although this is the current state of the battery market, there are some technologies that are very promising. One type of these batteries is the so-called flow battery, which is going to be the next subject.

2.3 Flow batteries

The history of flow batteries can be traced back to 1880, when John Doyle issued a patent that represented a galvanic battery. Although this is not a flow battery, the chemical reaction occurring is the same as the one in a zinc-bromine flow battery (Zn-Br2).

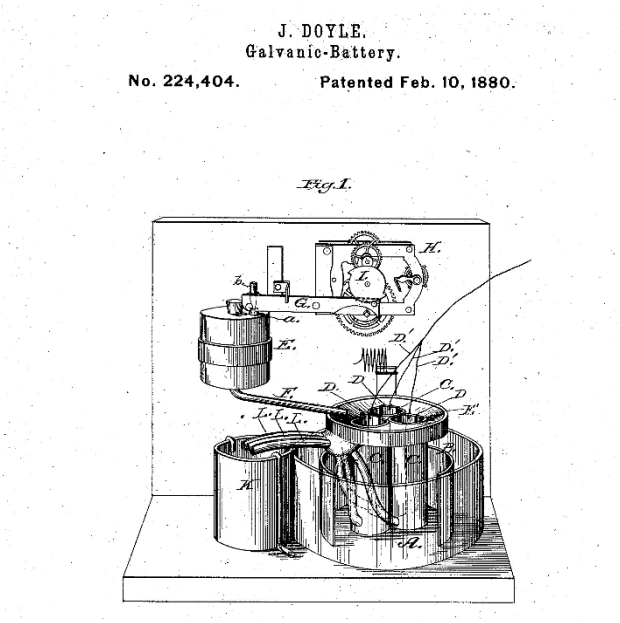
J. DOYLE.
Galvanic-Battery.
No. 224,404. Patented Feb. 10, 1880.
Fig. 1.

Figure 2.3: Patent US 224404A. Source: Google Patents

Unlike a traditional battery, in which energy is stored in the electrode without the need for any external parts, in a flow battery, it's necessary to have two tanks storing the positive and negative electrolytes. Flow batteries are also called redox flow batteries (RFBs) due to the processes of reduction and oxidation that occur during their operation.

The two tanks host the positive and negative electrolytes, and they are respectively called catholyte and anolyte. Two pumps pump the two chemical components into the usually porous electrode, where the reaction occurs, and the current collectors provide the current to the load attached to the flow battery. A flow battery is like a combination of a combustion engine and a battery. Like in a combustion engine, the energy vector is provided by an external tank, but the electrochemical reactions occurring are like those that take place in batteries. In the

following images, both a generic layout of a flow battery and a system with a stack of flow batteries are presented:

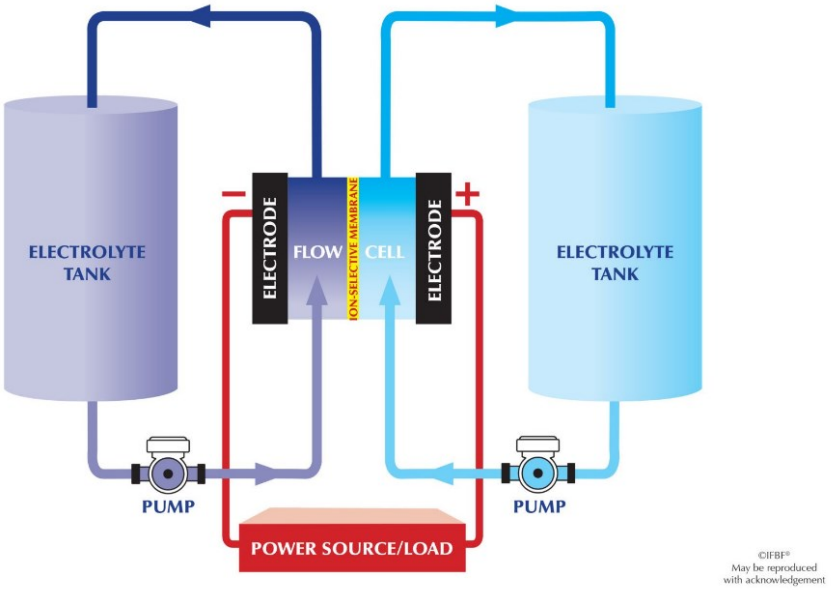

Figure 2.4: Flow battery scheme. Source: IFBF

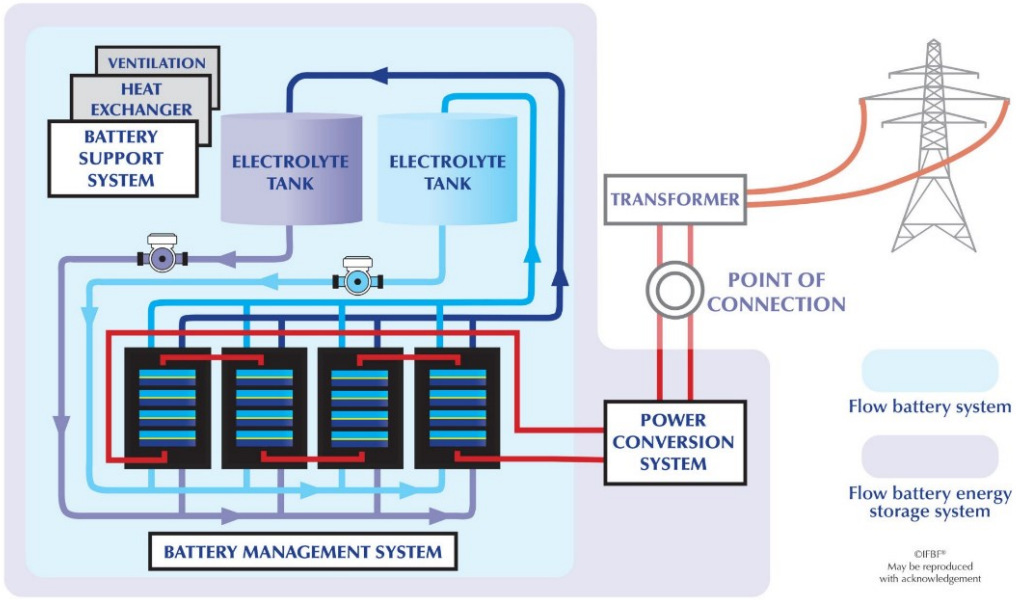

Figure 2.5: Stack of flow batteries implemented in the grid. Source: IFBF

Flow batteries nowadays are mainly used to make up for the intermittency of renewable sources. They are considered life-long storage systems, which are a key component of the grid to manage the demand for electricity. The following graph will provide a visual explanation:

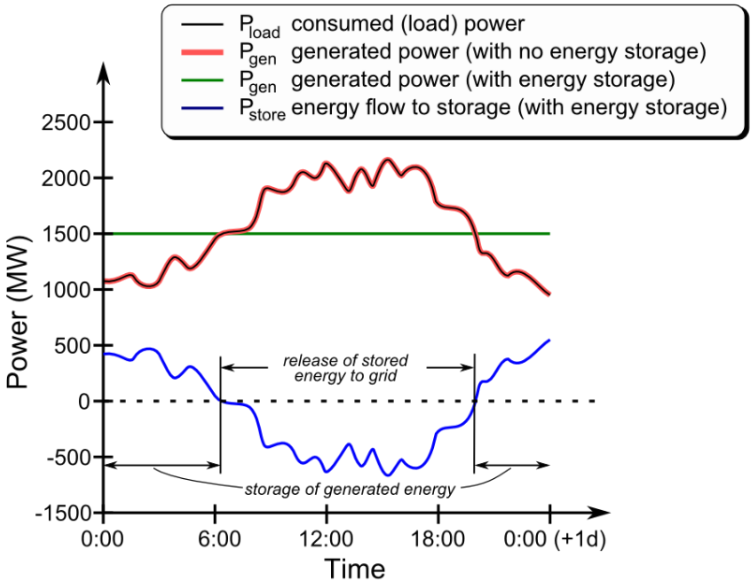

Figure 2.6: Mismatch between generation and demand of power. Source: Wikipedia

Basically, when the power generated is higher than the demand for electricity, energy is stored in the ESS. Then the energy stored is used when the demand is higher than the generation. For example, in a photovoltaic plant, most of the energy is produced during the day, so a portion of such energy is stored. Whereas during the night, the energy produced is nearly zero, so the energy previously stored is delivered to the grid.

Some other advantages of these batteries are:

- The durability of the stored energy, this is due to the low self-discharge. This characteristic makes flow batteries perfect for their integration in renewable power plants.
- High safety, thanks to their modularity, low degradation, and low risk of fire, all these features also guarantee a long service life.
- Raw materials availability and recyclability. This is very important to take into consideration the sustainability of the technology.

Now we will see the different types of flow batteries available and some of their features:

- Vanadium redox flow battery (VRFB)

  The vanadium redox flow battery utilizes vanadium ions in various oxidation states to store and release energy. It is known for its high efficiency, long cycle life, and the ability to discharge fully without damage, making it ideal for grid energy storage, renewable energy integration, and large-scale backup power. A more detailed description will be given in the next chapter.

- Zinc-bromine flow battery (ZBFB)

  Positive electrode: $Br_2 + Br^- \rightleftharpoons Br_3^-$
  Negative electrode: $Zn \rightleftharpoons Zn^{2+} + 2e^-$
  The zinc-bromine flow battery uses zinc and bromine as active materials in the electrolyte. This type of battery boasts high energy density and can operate over a wide range of temperatures. It is commonly used in residential energy storage, commercial applications, and utility-scale storage. Zinc is in a solid state during the charge, and it melts during the discharge. Bromine, both during charge and discharge, is always melted in an aqueous solution. The voltage obtained for a single cell is 1.8V, and the energy density is around 50Wh/l. The main drawbacks of zinc-bromine flow batteries are the costs due to the ion exchange membrane and the toxicity of bromine.

- Iron-chromium flow battery

  Positive electrode: $Fe^{2+} \rightleftharpoons Fe^{3+} + e^-$
  Negative electrode: $Cr^{3+} + e^- \rightleftharpoons Cr^{2+}$
  This flow battery type stores energy using iron and chromium in the electrolyte. They were first developed by NASA in the 1970s for photovoltaic applications. The catholyte presents an aqueous solution with iron ions, and the anolyte is composed of a solution with chromium ions acidified with hydrochloric acid (HCl). It features low-cost and environmentally friendly materials, making it suitable for large-scale energy storage applications, particularly in the utility and industrial sectors. However, iron-chromium flow batteries present a low voltage for a single cell, just 1V, and considerable degradation due to the poisoning of the ionic species.

- Hybrid flow battery

  Hybrid flow batteries combine elements of flow batteries and traditional batteries, often using a solid electrode alongside a liquid electrolyte. These batteries can offer improved energy density and lower costs compared to traditional flow batteries, catering to various energy storage needs, including residential and industrial applications.

- Hydrogen-bromine flow battery

  Positive electrode: $Br_2 + 2e^- \rightleftharpoons 2Br^-$
  Negative electrode: $H_2 \rightleftharpoons 2H^+ + 2e^-$
  The hydrogen-bromine flow battery utilizes hydrogen and bromine to store energy, releasing it through a reversible chemical reaction. It is characterized by high power density and relatively low material costs, making it suitable for grid energy storage, renewable integration, and industrial applications. The active reactant material, in this case, hydrobromic acid (HBr), is used as the supporting electrolyte. Even though the materials are low-cost, the components are not, for example, platinum catalysts. Even in this case, the single cell voltage is around 1 V.

- Polysulfide-bromine flow battery

  Positive electrode: $3Br^- \rightleftharpoons Br_3^- + 2e^-$
  Negative electrode: $2S_2^{2-} \rightleftharpoons S_4^{2-} + 2e^-$
  This battery uses polysulfide and bromine in its electrolyte solutions. It has a high energy density and is easily scalable for large storage needs, making it suitable for utility-scale energy storage and renewable energy integration. Only anions are involved in this process, so in this case, it's necessary to have a membrane that allows a cationic exchange to avoid the blending of the solution, which may cause the formation of hydrogen sulfide (H_2S), which is a highly toxic and flammable gas. The voltage of the single cell ranges between 1.7V and 2.1V.

- Organic flow battery

  The organic flow battery uses organic molecules in the electrolyte for energy storage. These batteries have the potential for lower costs and improved sustainability compared to metal-based flow batteries and are used in renewable energy storage, grid storage, and backup power systems.

- Cerium-zinc flow battery

  Positive electrode: $Ce^{3+} \rightleftharpoons Ce^{4+} + e^-$
  Negative electrode: $Zn \rightleftharpoons Zn^{2+} + 2e^-$
  Utilizing cerium and zinc in the electrolyte solutions, the cerium-zinc flow battery offers high energy efficiency and a long cycle life. It is mainly applied in large-scale energy storage and industrial applications.

- Vanadium-bromine flow battery

  Positive electrode: $Br_2 + 2e^- \rightleftharpoons 2Br^-$
  Negative electrode: $V^{2+} \rightleftharpoons V^{3+} + e^-$
  Combining vanadium and bromine electrolytes for energy storage, the vanadium-bromine flow battery features high energy density and good scalability. It is used for utility-scale storage, renewable energy integration, and grid stabilization.

3. Vanadium redox flow battery

Vanadium flow batteries were first patented in 1986 by chemical engineer Maria Skyllas-Kazacos at the University of New South Wales. Since then, such technology has developed and the research on vanadium batteries is still ongoing.

Commercial applications and large-scale systems are already present worldwide. The most imponent one in terms of power and capacity is located in the city of Dalian, China. The Dalian VFB Energy Storage Peak-shaving Power Station, developed by Rongke Power and Pu Jian, stands as one of the largest vanadium redox flow battery installations globally. With a power of output of 200 MW and a capacity of 800 MWh, this facility plays a crucial role in stabilizing the grid by providing peak shaving and load leveling services. It helps balance the intermittent supply from renewable sources, such as wind and solar, ensuring a steady and reliable power flow. This project underscores the scalability and efficiency of VRFB technology, demonstrating its potential for large-scale energy storage applications and enhancing grid stability.

Figure 3.1: Dalian VFB Energy Storage Peak-shaving Power Station. Source: Rinnovabili.it

Before entering into the details of the electrochemical reactions occurring inside the cell of a VRFB, it is important to understand the structure of the battery, how it works and analyze each component.

3.1 VRFB structure and components

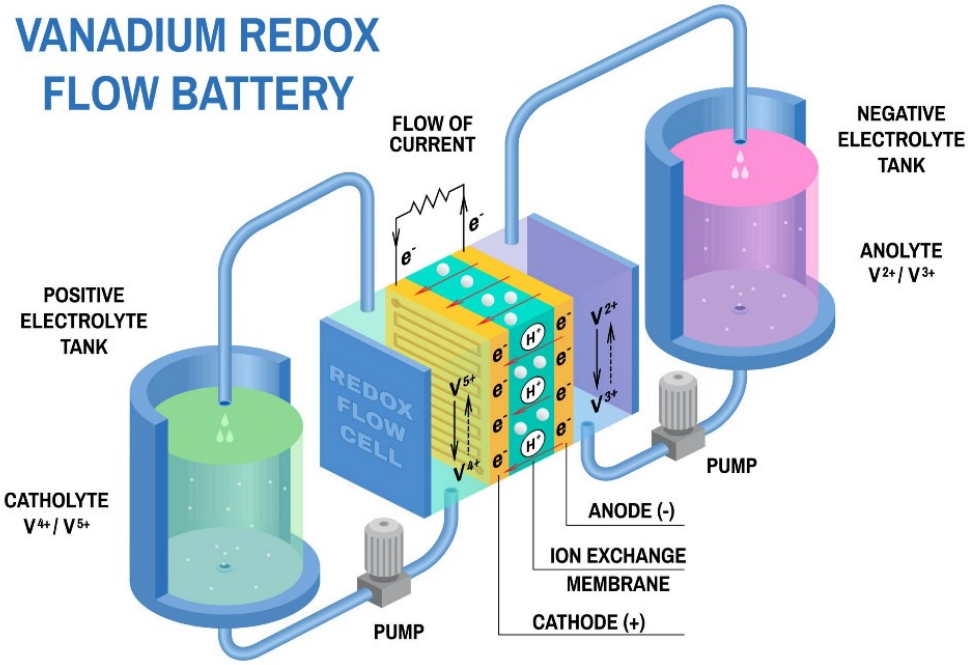

Figure 3.2: Schematic of a single cell of a VRFB. Source: BE&R Consulting

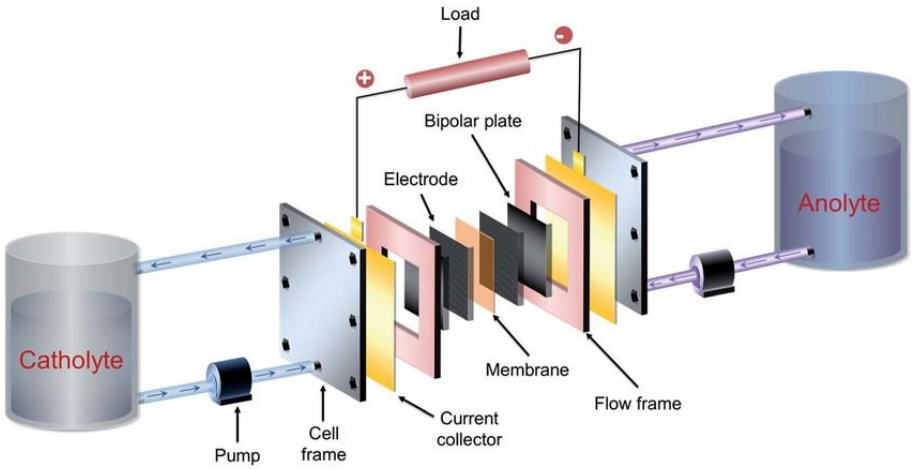

Figure 3.3: Detailed schematic of a single cell with its components [2]

Figures 3.2 and 3.3 offer a detailed schematic of a single-cell VRFB; however, most vanadium batteries are designed with multiple cells in order to provide a higher power output. Cells are collected in a stack, and a single stack can contain multiple cells. For example, a stack can be composed of 20 or 40 cells, as shown in figure 3.4. There is no specific number, but practically the number is limited by the overall voltage of the stack because higher voltages might increase the costs. Cells in the same stack share the same cell frames and current collectors. VRFBs composed of multiple stacks are called multi-stack VRFBs.

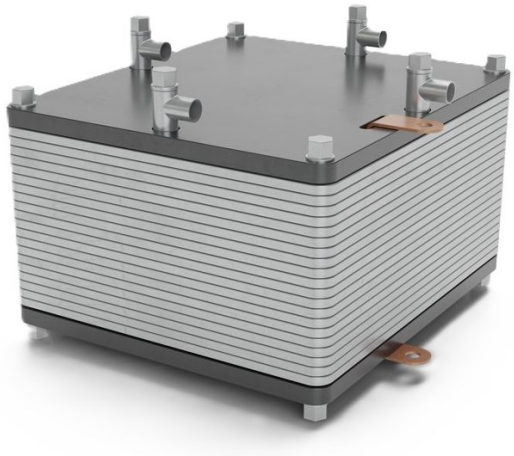

Figure 3.4: A 20-cells stack. Source: Marposs

3.1.1 Tanks and pumps

The two tanks in a VRFB have the primary function to store the electrolytes solutions, the anolyte and the catholyte. Thanks to the tanks the two solutions are kept apart, to avoid unwanted chemical reactions. The tanks are connected to the battery stack through a system of pumps and pipes. During operation, the electrolytes are pumped from the tanks into the stack where the electrochemical reactions occur, and then they return to the tanks. Proper circulation of the electrolytes is crucial for the efficient functioning of the VRFB. The design of the tanks and the pumping system ensures that the electrolyte flows smoothly and consistently through the battery stack. The tanks must be made from materials that are chemically resistant to acidic vanadium electrolyte solutions. Common materials include high-density polyethylene (HDPE), polyvinyl chloride (PVC), and other chemically resistant plastics. The capacity of the tanks directly affects the energy storage capacity of the VRFB. Larger tanks can store more electrolyte, thereby increasing the battery's overall energy capacity. The size is typically determined by the application and the required energy storage

duration. Given the acidic nature of the electrolytes, the tanks must be designed with safety in mind. This includes features like leak detection systems and secondary containment to capture any spills. The rate at which the electrolyte is pumped through the battery stack affects the power output and efficiency. Optimizing flow rates is essential for balancing performance and minimizing energy consumption by the pumps. This procedure is usually automated thanks to a feedback system regulated by a battery management system (BMS).

3.1.2 Cell frames, current collectors and bipolar plates

Cell frames provide structural support to the individual cells within the battery stack. They are responsible for holding the various components of a cell (such as the electrodes and membranes) in place, ensuring proper alignment and sealing to prevent electrolyte leakage. The frames must be robust enough to handle the pressures exerted during assembly and operation, maintaining the structural integrity of the stack.

Current collectors serve the critical function of conducting electrical current from the electrodes to the external circuit. They are placed adjacent to the electrodes and facilitate the transfer of electrons generated during the redox reactions within the cell. Of course, high electrical conductivity is essential to minimize electrical resistance and energy losses, improving the overall efficiency of the battery. Given the corrosive nature of the vanadium electrolytes, current collectors must be designed to resist degradation over time to ensure long-term performance and reliability.

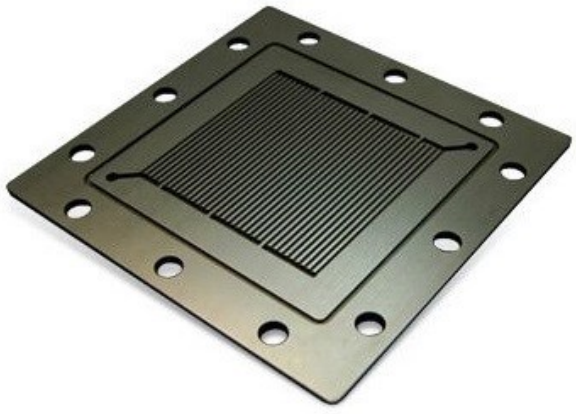

Figure 3.5: A bipolar plate. Source: JP Carbons

Bipolar plates help distribute the electrolyte solutions uniformly across the electrode surfaces. They contain channels, as visible in figure 3.5, that guide the electrolyte flow, enhancing the contact between the electrolyte and the electrode, which is vital for efficient electrochemical

reactions. These plates physically separate the positive and negative electrolyte solutions, preventing them from mixing while allowing the flow of ions through the membrane. This separation is crucial for maintaining the chemical integrity and efficiency of the redox reactions. Bipolar plates are also responsible for conducting electrical current between adjacent cells in a stack. They provide a pathway for electrons to flow from the positive electrode of one cell to the negative electrode of the next, ensuring the series connection of multiple cells. Bipolar plates provide mechanical support to the overall structure of the battery as they help maintain the alignment and compression of the cell components. Figure 3.5 shows just one design that a bipolar plate can have. Channels can be designed differently, with other patterns from the one shown. We will see how this design can affect the value of shunt currents in the channels. The holes on the frame of the bipolar plate in figure 3.5 provide the passage of components like the bolts of the cell frames.

3.1.3 Electrodes and membranes

Electrodes and membranes are key components of VRFBs, there are many different possible solutions and applications, as shown respectively in the papers by J. Kim and H. Park [3] and by C.H.L. Tempelman et al. [5].

The choice of the electrode material is crucial since it must possess high electrical conductivity to ensure efficient electron transfer and, at the same time, be chemically stable to withstand the highly acidic vanadium electrolyte environment. Commonly used materials include carbon-based substances like graphite felt or carbon paper, which offer a large surface area to facilitate the redox reactions. There are many factors to take into account during the development of electrodes. Some of them are: porosity, permeability, operating temperature, compression rate and tortuosity. Figure 3.6 shows a microscopic view of felt-type electrodes.

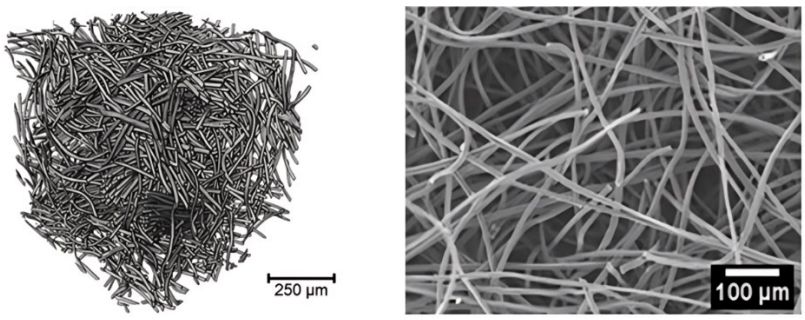

Figure 3.6: Microscopic visualization of felt-type electrodes [4]

The membrane is a crucial component, and the main two functions it provides are ion exchange and the prevention of cross-contamination. The ion exchange membrane facilitates the flow of ions between the two half-cells of the battery. During charging and discharging, it allows protons (H^+ ions) to move through it, balancing the charge as electrons flow through the external circuit. One of the membrane's most important roles is to prevent the mixing of the positive and negative electrolyte solutions. Any cross-contamination can lead to a loss of efficiency and capacity. There are three main categories of membranes, as explained in the paper by C.H.L. Tempelman et al. [5].

- Cationic exchange membranes (CEMs)

  In these membranes, a porous support is combined with an ion-exchange resin or polyelectrolyte and a cross-linking agent. This mixture is then cured to trigger the cross-linking process. These membranes were initially made from sulfonated porous polyethylene and polystyrene materials. Nowadays, many solutions are available.
- Anion exchange membranes (AEMs)

  Their positively charged functional groups repel positively charged vanadium species from the membrane, an effect known as the Donnan effect. Despite the reduced vanadium permeability that makes AEMs appealing, they have significant drawbacks for use in VRFBs. AEMs exhibit lower proton conductivity and poor chemical stability, which hinders their commercial viability in VRFB applications.

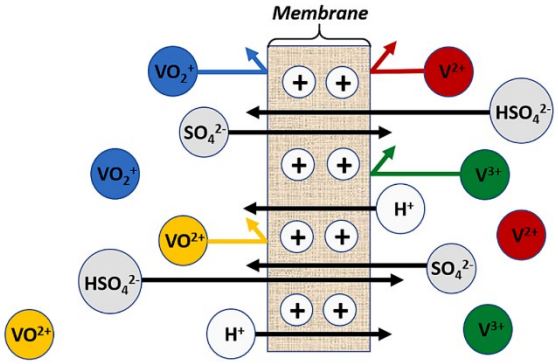

Figure 3.7: Schematic representation of an anion exchange membrane [5]

- Amphoteric ion-exchange membranes (AIEMs)

  Amphoteric ion-exchange membranes include both anionic and cationic exchange groups, combining the properties of AEM and CEM membranes. CEMs offer superior stability against chemical degradation and higher conductivity, while AEMs exhibit lower rates of vanadium crossover. However, both types of membranes face issues with water transfer through the membrane due to the crossover of vanadium, SO_4^{2-}, and HSO_4^- species.

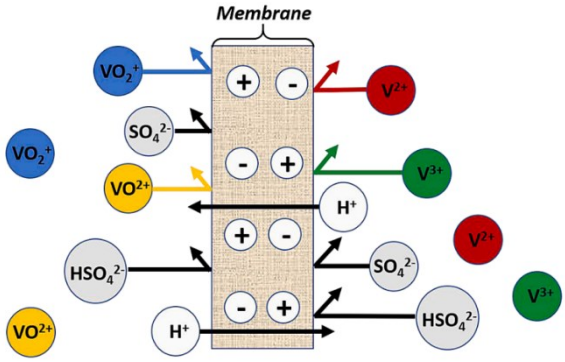

Figure 3.8: Schematic representation of an amphoteric ion-exchange membrane [5]

3.2 VRFB electrochemical reactions

3.2.1 G1 technology

This technology is based on the use of V^{2+}/V^{3+} redox pairs at the negative electrode and V4+/V5+ redox pairs at the positive electrode, all diluted in an aqueous solution of HCl or a mixture of HCl/H_2SO_4. The reactions that occur are:

Positive electrode: $V^{2+} \rightleftharpoons V^{3+} + e^-$

Negative electrode: $VO_2^+ + 2H^+ + e^- \rightleftharpoons VO^{2+} + H_2O$

As mentioned earlier, in this configuration, any mixing of the two electrolyte solutions does not have severe consequences for the battery. It is sufficient to remix the two electrolytes to regenerate the solution. Problems affecting this battery include the instability of V^{4+} in NaOH solution and V^{5+} in HCl solution, as well as the reaction kinetics of the VO_2^+/VO^{2+} pair, which tend to be quite slow due to the strong bonds with oxygen.

This can be improved by varying the material of the electrode, such as using carbon-based materials. The cell voltage is around 1.26V at 25°C (though it can reach 1.4V in practice), with

a current density of 120-150 mA/cm^2 (up to 1000 mA/cm^2) and an energy density range of 25-35 Wh/l.

3.2.2 G2 technology

Unlike G1, this technology does not use only vanadium in the two half-cells but rather a vanadium/bromine solution with hydrochloric acid. The redox reactions involved are:

Positive electrode: $V^{2+} \rightleftharpoons V^{3+} + e^-$

Negative electrode: $ClBr_2^- + 2e^- \rightleftharpoons 2Br^- + Cl^-$

or $BrCl_2^- + 2e^- \rightleftharpoons Br^- + 2Cl^-$

This technology offers the advantages of the G1 solution (absence of cross-contamination issues) and also allows for higher concentrations of vanadium ions, resulting in higher energy density levels. Additionally, due to the high solubility of the vanadium-bromine compound, the operating temperature range is extended (0-50°C) compared to G1 technology. However, problems include the production of toxic bromine vapors during the discharge process, which must be mitigated using chemical agents, leading to increased costs. The cell voltage is about 1.3V, and the energy density ranges from 35-70 Wh/l.

4. Shunt current

Considering the composition of a vanadium redox flow battery the electrolyte flows between the cells thanks to channels and manifolds and when there is a stack the electrolyte flows through pipes that are in fact electrically conductive. During the operation of the battery there is a voltage difference between the cell and the stacks, and this voltage difference causes the generation of shunt currents. Knowing this information it's clear that shunt currents are dependent from the connections between cells and the stack structure. In order to understand the behavior of shunt currents we first need to understand how to model to an electrical circuit the vanadium flow battery stack.

4.1 VRFB equivalent circuit

The modelling of a general electrical circuit for VRFBs is not simple, since there are many factors that have to be taken into account, like the temperature and the connections between stacks. According to research by X. Zhao et al. [6] for a single cell the following circuit is valid:

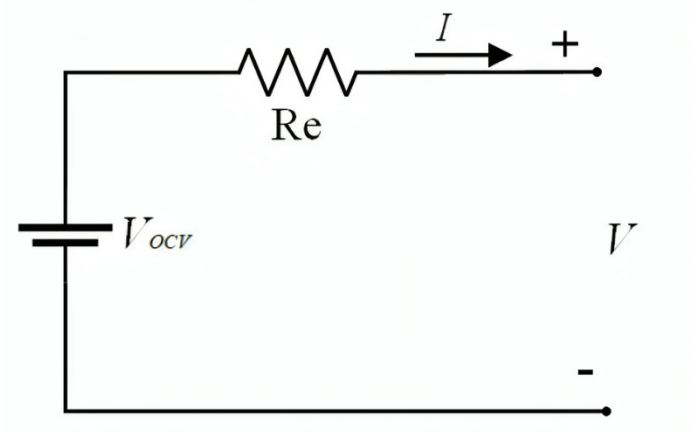

Figure 4.1: Equivalent circuit for a single cell in VRFBs [6]

In the circuit of figure 4.1 the resistance Re is the internal resistance of the cell and it depends on the resistance of the components, its connections and the state of charge (SOC). In series to the internal resistance there is a controlled voltage source which can be defined with the Nernst equation as:

$$V_{OCV} = V_O + \frac{2RT}{F} ln\left(\frac{SOC}{1-SOC}\right) \quad (4.1)$$

In the equation (4.1) V_0 is the open circuit voltage, which is also the equilibrium potential, so V=1.225V, R is the gas constant, T is the temperature, F is the Faraday constant and SOC is the state of charge. Now the cell voltage can be defined in equation (4.2) and also the voltage of the stack in equation (4.3):

$$V_{cell} = V_{OCV} - R_e I \quad (4.2)$$

$$V_{stack} = \sum_{i=1}^{n} V_{cell,i} \quad (4.3)$$

It is clear that there is a dependance of the voltage of the cell from the temperature and the state of charge, so, to continue the analysis on a stack composed of multiple cells and a multi-stack structure, some assumptions need to be done:

1. The value of the temperature is considered constant; this means that we have to consider a uniform temperature distribution in the whole battery and also a uniform electrolyte concentration.

2. The value of the state of charge is considered constant, to avoid any borderline condition, usually the SOC considered is 50%.

3. The shunt current does not increase or decrease along the stack or the pipes, in other words the shunt current is the same at the inlet and the outlet of the single channel.

4. The electrical potential of the single cells is uniform throughout the active area.

Now we consider for example a stack composed of three cells described in a paper by Alasdair Crawford and Vilayanur Viswanathan [7], the equivalent circuit is as follows:

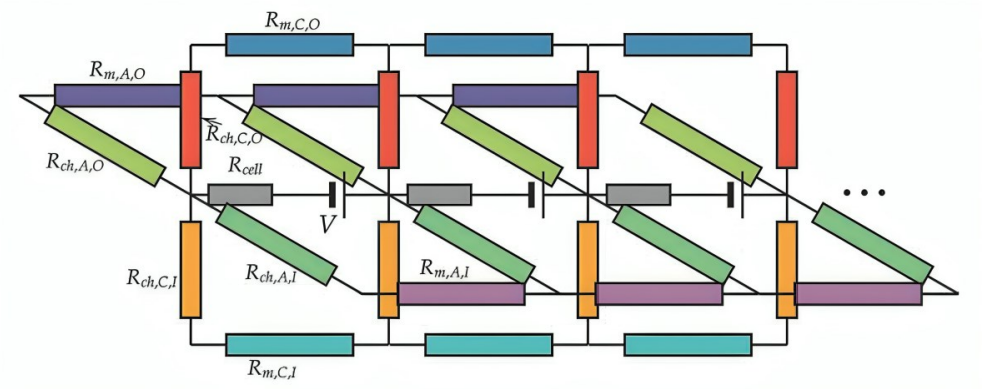

Figure 4.2: Equivalent circuit for a stack composed by three cells in VRFBs [7]

First and foremost, for clarity, the $R_{cell} = R_e$ and $V = V_{cell}$, all the resistances in figure 4.2 (besides R_{cell}) are calculated with the equation (4.4):

$$R = \frac{l}{\sigma A} \tag{4.4}$$

where l is the length of the considered channel, σ is the electrolyte conductivity that is dependent on the state of charge, however as already mentioned, the SOC is fixed, and A is the cross-section are of the channel. The subscripts of the resistances have the following meanings:

1. The channel and the manifold are represented by the two subscripts *ch* and *m*.

2. The catholyte and the anolyte are represented by the two subscripts *C* and *A*.

3. The inlets and the outlets are represented by the two subscripts *I* and *O*.

Now that the stack is defined, the next step is to understand how in a multi-stack structure the different stacks are connected one to each other, to then understand how different configurations affect shunt currents. For simplicity figures 4.3, 4.4 and 4.5 represent the connections between five stacks, without the pipes from the tanks, a more complex configuration will be seen in figure 4.6.

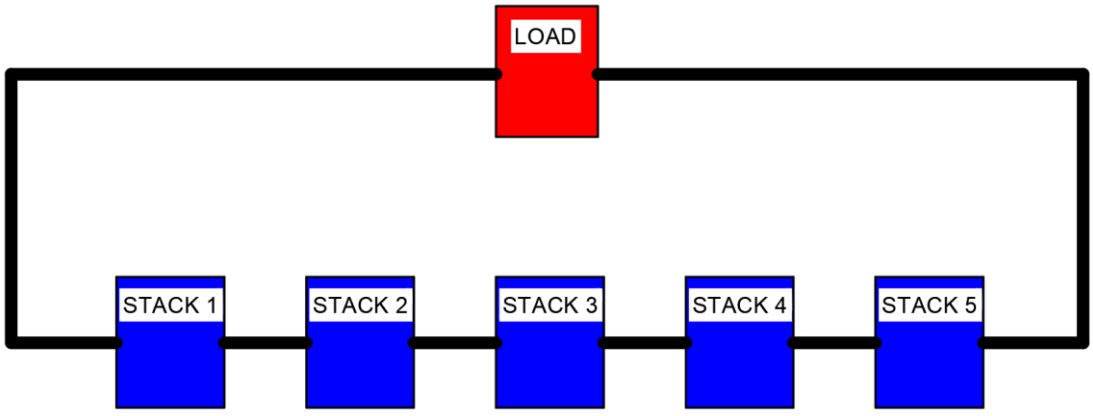

Figure 4.3: Series connection configuration of a multi-stack VRFB

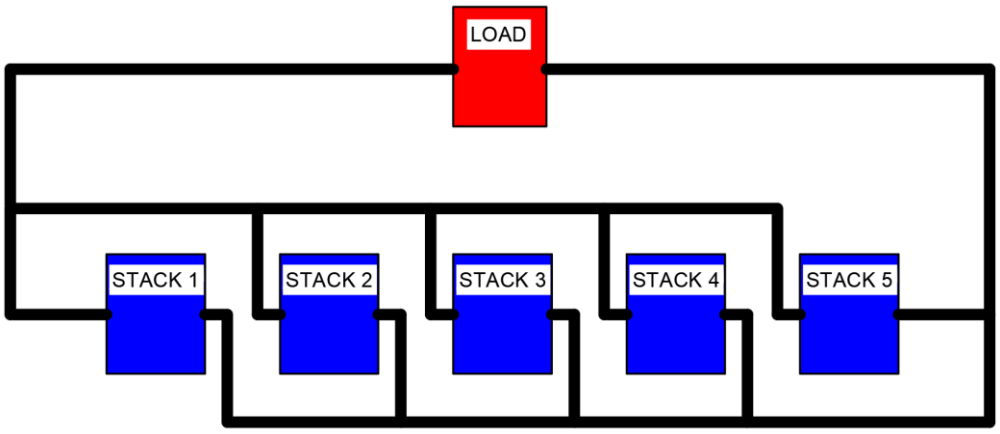

Figure 4.4: Parallel connection configuration of a multi-stack VRFB

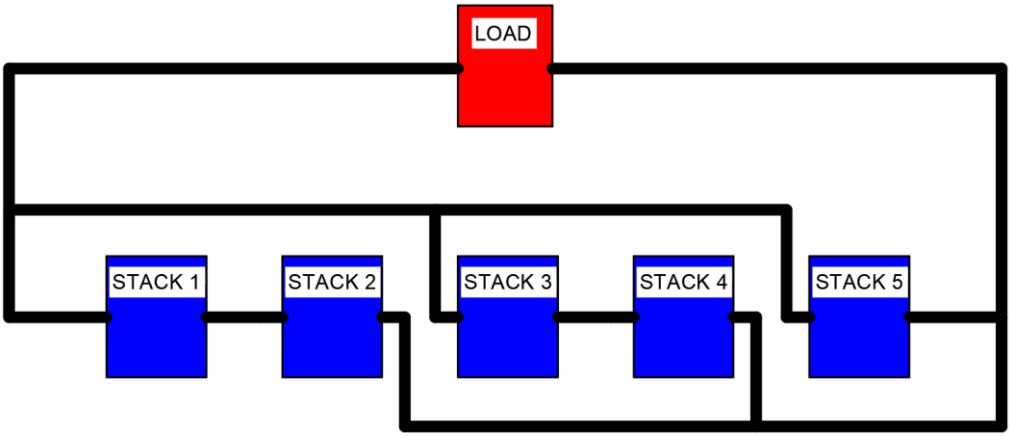

Figure 4.5: Mixed connection configuration of a multi-stack VRFB

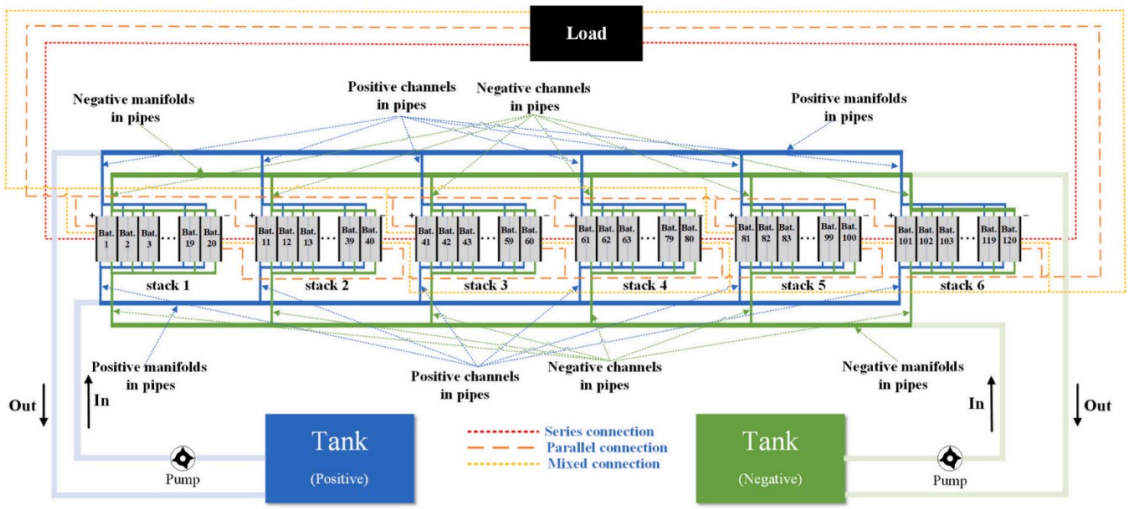

Figure 4.6: Schematic of a multi-stack VRFB system [6]

Now that the structure of a VRFB system is well defined, it is possible to study the behavior of shunt currents.

4.2 Shunt current mathematical models

In order to obtain the trend of shunt currents both experimental simulations and mathematical models (they can be both differential and based on linear algebra) are valid, the latter will be now studied.

4.2.1 Linear algebra mathematical model

This mathematical model described in an article by Y.-S. Chen et al. [8] is based on the equivalent circuit that we have already seen before in figure 4.2, also the subscripts are still the same, but in this case since both charge and discharge are considered instead of cathode and anode, we consider the positive and negative electrode, with the subscripts respectively being *P* and *N*. Let us consider a VRFB stack composed of *M* cells in this case connected in series and the assumption that were mentioned in paragraph 4.1 are still valid. Lastly, we also consider a generic *i*-th cell.

As a result of all of this there are (5*M* - 2) equations that are required to solve this mathematical model. Applying the Kirchoff's current and voltage laws we obtain the following five linear algebraic equations:

$$I_i - I_{i-1} - 2I_{P,ch,i} - 2I_{N,ch,i} = 0 \tag{4.5}$$

$$I_{P,ch,i} + I_{P,m,i} - I_{P,m,i-1} = 0 \tag{4.6}$$

$$I_{N,ch,i} + I_{N,m,i} - I_{N,m,i-1} = 0 \tag{4.7}$$

$$V_i - R_{P,ch}I_{P,ch,i} + R_{P,m}I_{P,m,i} + R_{P,ch}I_{P,ch,i+1} = 0 \tag{4.8}$$

$$V_i - R_{N,ch}I_{N,ch,i} + R_{N,m}I_{N,m,i} + R_{N,ch}I_{N,ch,i+1} = 0 \tag{4.9}$$

A consideration that can be made is that the first cell has no complete negative electrolyte circuit, so now, defining I_{app} as the applied current during charge or discharge, we have just three linear algebraic equations:

$$I_1 - I_{app} - 2I_{P,ch,1} = 0 \tag{4.10}$$

$$I_{P,ch,1} + I_{P,m,1} = 0 \tag{4.11}$$

$$V_1 - R_{P,ch}I_{P,ch,1} + R_{P,m}I_{P,m,1} + R_{P,ch}I_{P,ch,2} = 0 \tag{4.12}$$

Furthermore, there is no complete positive electrolyte circuit for the M-th cell, necessitating modifications to the linear equations:

$$I_M - I_{M-1} - 2I_{P,ch,M} - 2I_{N,ch,M} = 0 \tag{4.13}$$

$$I_{P,ch,M} - I_{P,m,M-1} = 0 \tag{4.14}$$

$$I_{N,ch,M} + I_{N,m,M} - I_{N,m,M-1} = 0 \tag{4.15}$$

$$V_M - R_{N,ch}I_{N,ch,M} + R_{N,m}I_{N,m,M} + R_{N,ch}I_{N,ch,M+1} = 0 \tag{4.16}$$

In the last cell is also true that:

$$I_{N,ch,M+1} - I_{N,m,M} = 0 \tag{4.17}$$

Now that a total of $(5M - 2)$ linear equations are available and those equations written in a matrix form and the following results are obtained for a 20 cells stack, at a state of charge of 50% with an applied current of 54 A:

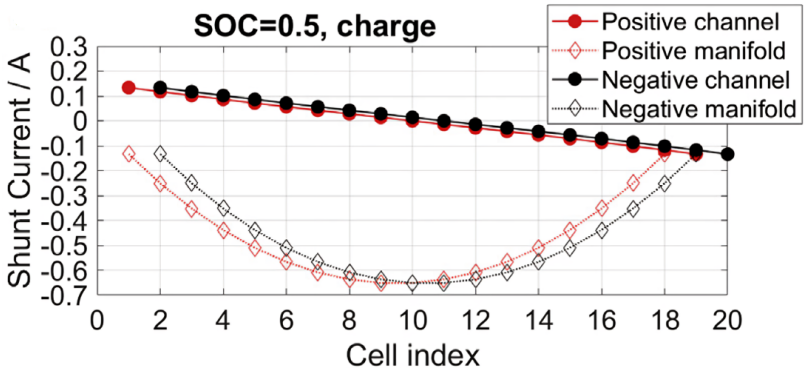

Figure 4.7: Shunt current trend during charge [8]

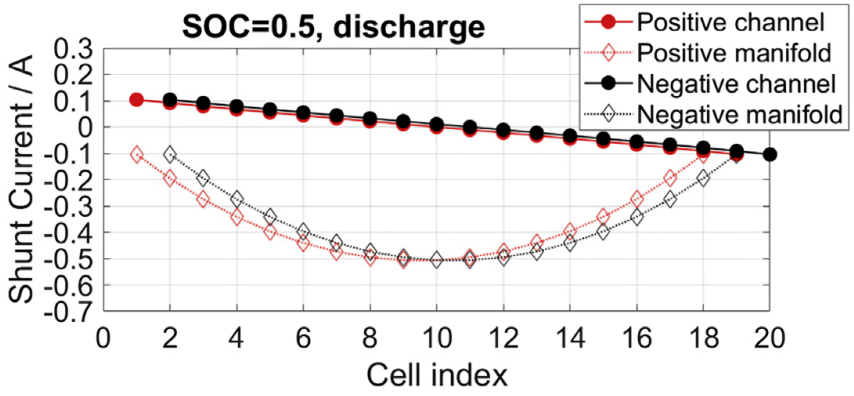

Figure 4.8: Shunt current trend during discharge [8]

Now the shunt current distribution for a stack composed by 40 cells:

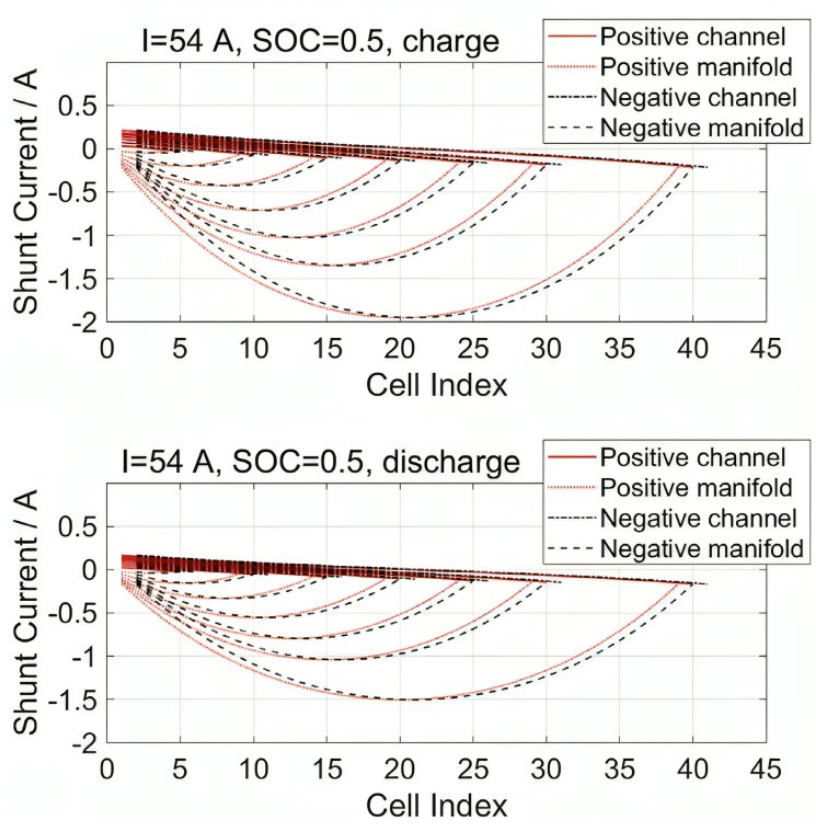

Figure 4.9: Shunt current distribution in 40 cells during charge and discharge [8]

These graphs provide valuable insights regarding the behavior of shunt currents. Specifically, shunt currents exhibit higher values in the central cells when considering the manifolds. Whereas, within the channels, shunt currents tend to decrease linearly from the first to the last cell. Additionally, the number of cells in the stack significantly influences the magnitude of shunt currents, as the number of cells in the stack increases, the magnitude of shunt currents rises correspondingly in both channels and manifolds.

4.2.2 Differential mathematical model

The mathematical model now analyzed is another approach to study shunt currents, but the results obtained are the same as the previous model and the experimental values.

The first consideration that needs to be made is that in figure 4.2 can be identified four sections, that are anolyte in and out and catholyte in and out. These four sections can be simplified in the following repeating circuit:

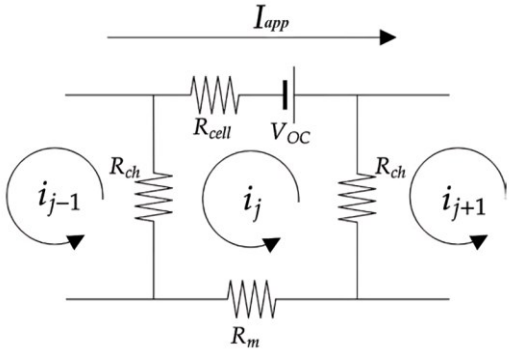

Figure 4.10: Considered circuit for each cell [7]

R_m is the resistance of the manifold, R_{ch} is the resistance of the channel, R_{cell} is the intrinsic resistance of the cell, V_{OC} is the voltage of the cell, calculated in the equation (4.1), I_{app} is the applied current and lastly i_j is the current of the j-th loop. For the cells at the very beginning and at the very end of the stack, this current is equal to zero. Using Kirchoff's law we obtain:

$$\left(V_{OC} + I_{app}R_{cell}\right) - (4R_{cell} + R_m)i_j + R_{ch}\left(i_{j+1} + i_{j-1} - 2i_j\right) = 0 \qquad (4.18)$$

The factor of four is due to the fact that we are considering the four sections mentioned above. Now it is possible to convert this equation into a derivative form, providing an analytical solution for shunt currents, which is also easy to implement. From the second derivative definition we have:

$$1 - \frac{4R_{cell}+R_m}{V_{OC}+I_{app}R_{cell}} i(j) + \frac{R_{ch}}{V_{OC}+I_{app}R_{cell}} \frac{d^2 i}{dj^2} \qquad (4.19)$$

Nondimensionalizing equation (4.19) it results in:

$$\frac{4R_{cell}+R_m}{V_{OC}+I_{app}R_{cell}} i = I \qquad (4.20)$$

$$j\sqrt{\frac{4R_{cell}+R_m}{R_{ch}}} = J \qquad (4.21)$$

These two equations provide two characteristic constants, the characteristic cell number *r* and the characteristic current I_K:

$$\sqrt{\frac{R_{ch}}{4R_{cell}+R_m}} = r \tag{4.22}$$

$$\frac{V_{OC}+I_{app}R_{cell}}{4R_{cell}+R_m} = I_K \tag{4.23}$$

The nondimensionalization results in:

$$1 - I(J) + \frac{d^2I}{dJ^2} = 0 \tag{4.24}$$

The general analytic solution is:

$$I(J) = C_1 \cosh(J) + C_2 \sinh(J) + 1 \tag{4.25}$$

Knowing the stack's cell structure, applying the boundary conditions and inserting the constants of equations (4.22) and (4.23) we obtain an equation providing the shunt current distribution across the stack:

$$i(j) = I_K(1 - \operatorname{sech}\left(\frac{n}{2r}\right) cosh\left(\frac{j}{r}\right)) \tag{4.26}$$

where *n* is the number of cells in the stack.

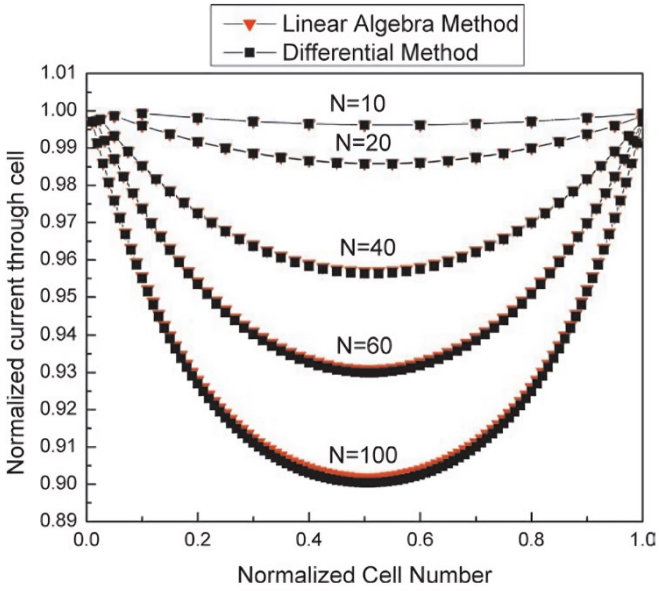

Figure 4.11: Shunt current trends for both mathematical methods [7]

4.3 Shunt current behavior

In order to understand how shunt currents behave, it is important to verify the mathematical models with experimental measurements. The following papers provide more detailed aspects involving shunt currents.

The first writing considered is by C. Yin et al. [9]. This paper introduces a coupled three-dimensional (3D) electrochemical model that aligns with the real dimensions of the experimental cell stack. The study aims to explore the distribution of shunt current and its effect on coulombic efficiency. To assess shunt current losses and confirm the model, experimental investigations were carried out using a single VRFB cell and a short stack of five cells. For the VRFB cell stack performance evaluation, the initial electrolyte solutions for the positive and negative vanadium half-cells are 1.5 mol/l vanadyl sulfate $VOSO_4$ and 1.5 mol/l vanadium tri-sulfate $V_2(SO_4)_3$, respectively, with both sides using 2 mol/l sulfuric acid H_2SO_4. The performance of the single-cell and five-cell short stack is assessed during charge and discharge cycles with a constant flow rate of 6 ml/s and 30 ml/s, respectively, at a current density of 60 mA/cm^2. The manifold's cross-sectional area is 1.64 cm^2, and the electrolyte flow channel depth, designed into the PVC frame, is 2 mm.

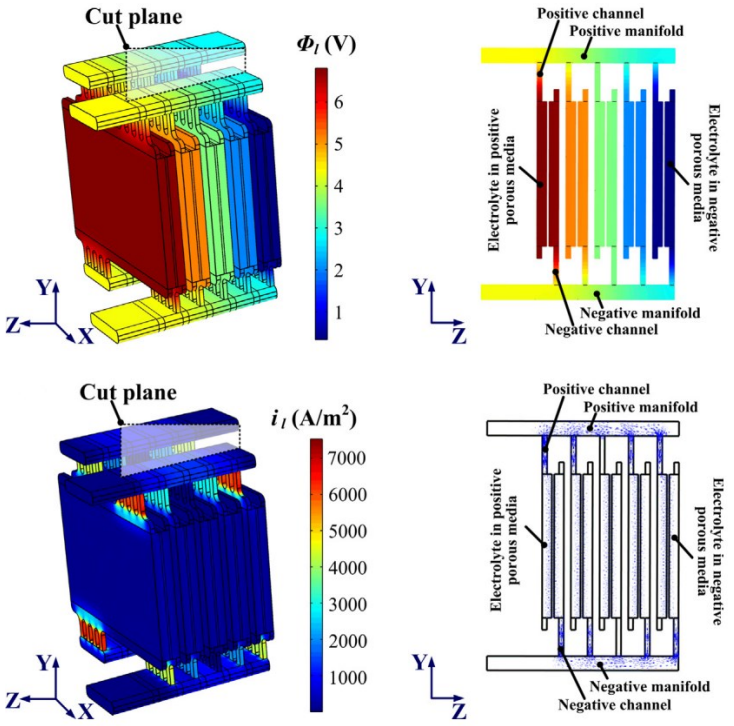

Figure 4.12: 3D/2D model representation with electrolyte potential and current density distribution [9]

A significant challenge emerged during the testing of the five-cell short stack, which allowed for shunt currents to pass between the cells. The experimental findings revealed a drop in the short stack's coulombic efficiency to 73.1%, signifying a considerable loss attributed to shunt currents. The simulation outcomes were in close agreement with the experimental observations, with the model estimating a coulombic efficiency of 72.3%. The researchers examined the cell voltage distribution and internal currents within the stack, discovering that the cells at the extremities of the stack were subject to higher voltages and increased shunt currents compared to the central cells. This discrepancy was linked to the non-uniform distribution of electrolyte resistances across the manifold and channel regions, resulting in the outer cells bearing a higher current load.

The research continued to examine the impact of adding more cells to a stack by modeling both a 10-cell and a 20-cell stack. It was observed that shunt current losses rose with the cell count, yet not in a direct proportion. Specifically, the shunt current loss was 47.9% in the 10-cell stack and 48.5% in the 20-cell stack. This suggests that as the stack size increases, the growth rate of shunt current losses diminishes, likely due to the rising resistance in the electrolyte solutions.

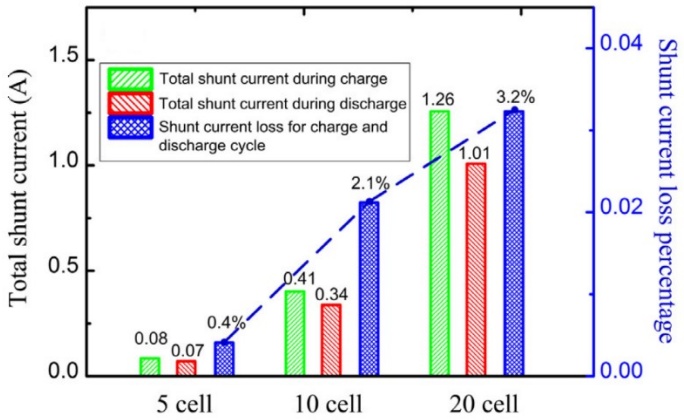

Figure 4.13: Shunt current trend with a high resistance varying cells number [9]

Additionally, it studied how changes in electrolyte conductivity within the manifold and channel areas affected performance. It was found that increasing the resistance in these areas could significantly decrease shunt current losses. For instance, a thirtyfold increase in resistance brought the shunt current loss down from 47.9% to 2.1% in the 10-cell stack. The results of the study demonstrate that shunt current losses are a critical factor in the design of VRB systems, especially as the stack size increases. The paper suggests that one approach to minimizing these losses is to increase the resistance of the electrolyte solutions in the manifold and channel regions. Figure 4.14 shows the original values of shunt current then, in order, with

an increased channel resistance, an increased manifold resistance and both channel and manifold resistances increased.

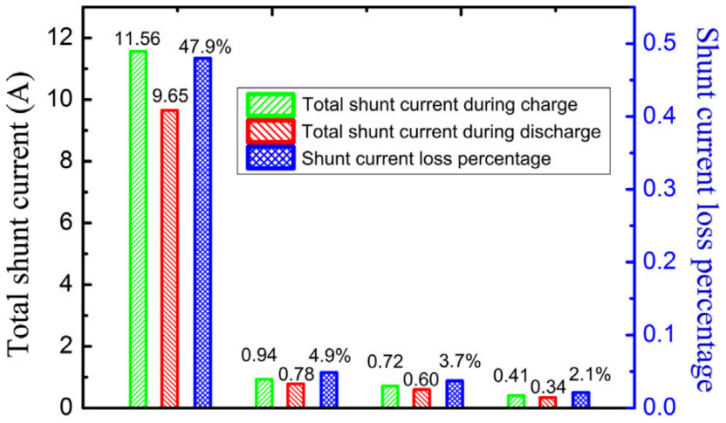

Figure 4.14: Shunt current decrease by decreasing the electrolyte conductivity [9]

However, it is also true that this must be done carefully, as increasing the resistance too much could result in other issues, such as increased pressure drops, uneven electrolyte distribution and increased temperatures, as we will see in the next section. It is also recommended optimizing the stack design to achieve a balance between minimizing shunt currents and maintaining efficient electrolyte flow.

Lastly the paper also presents charts showing the trends of shunt currents varying with the state of charge. For the manifold, with a higher SOC shunt current values increase and vice versa, as shown in figure 4.15:

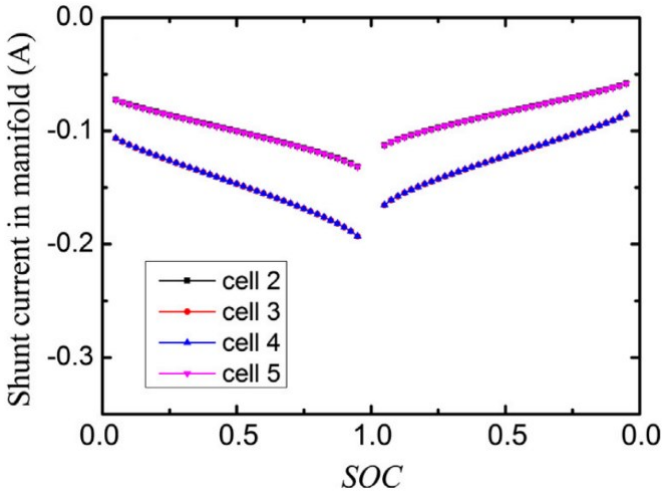

Figure 4.15: Shunt current during charge and discharge in the manifold [9]

Another useful paper is the one published by F.T. Wandschneider et al. [10]. This study analyzes with a model consisting of three stacks electrically connected in series the behavior of shunt currents. Each stack is composed of 10 cells. The equivalent circuit considered is the one already seen in figure 4.2. The initial electrolyte for both vanadium half-cells was an aqueous solution containing 0.8 mol/l vanadyl sulfate $VOSO_4$, 0.4 mol/l di-vanadium tri-sulfate $V_2(SO_4)_3$, 2 mol/l sulfuric acid H_2SO_4, and 0.05 mol/l phosphoric acid H_3PO_4. A vanadium redox flow battery with an anion exchange membrane was used to prepare the anolyte and catholyte solutions. Electrodialysis was conducted on an electrolyte with a current density of 25 mA/cm^2. Anolyte and catholyte solutions were formulated to correspond to states of charge of zero and one, respectively. Subsequently, these solutions were employed to generate mixtures of electrolyte solutions to attain diverse states of charge for each half-cell. In the model used for the calculations a time-dependency was implemented, as well as a variable electrolyte conductivity based on the state of charge and temperature.

In the initial configuration, the stacks are isolated, lacking any fluidic connections (no-pipe configuration). Subsequently, fluidic links are introduced between the stacks. In this second setup, the electrolyte flows in and out of the stack from the same side (same-side configuration). In the third variation, the electrolyte is fed into the stack on one side and discharged from the opposite side (opposite-side configuration), with inlets and outlets situated on opposing sides of the stacks. Each configuration undergoes three sequential galvanostatic charge and discharge cycles at current densities of 25, 50, and 75 mA/cm². The electrolyte's initial state-of-charge (SOC) is 0.05, charging continues until the SOC hits 0.95, followed by discharging back to an SOC of 0.05. The paper offers a view of shunt current trends during three charge and discharge cycles in these configurations, observable in figure 4.16:

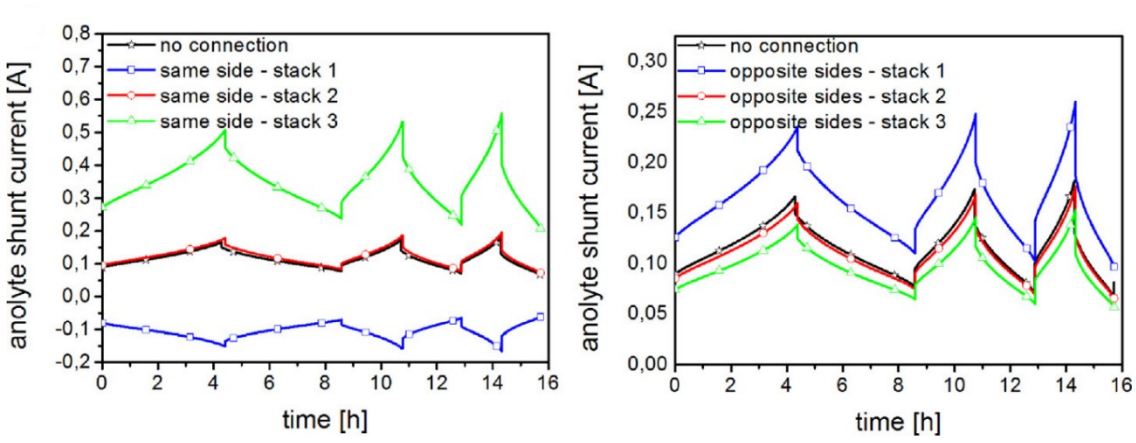

Figure 4.16: Shunt currents during battery operation for the different configurations [10]

Compared to previous papers, figure 4.16 shows shunt current with a variable state of charge, like figure 4.15, but with multiple charges and discharges. The model shows that the magnitude of the shunt currents increases with the SOC. At a high SOC, the ionic conductivity is greater, leading to lower resistances in the electrolyte pathways and higher shunt currents. This is particularly problematic during the discharge phase, where the shunt currents cause a faster depletion of the charged species, reducing the overall discharge time.

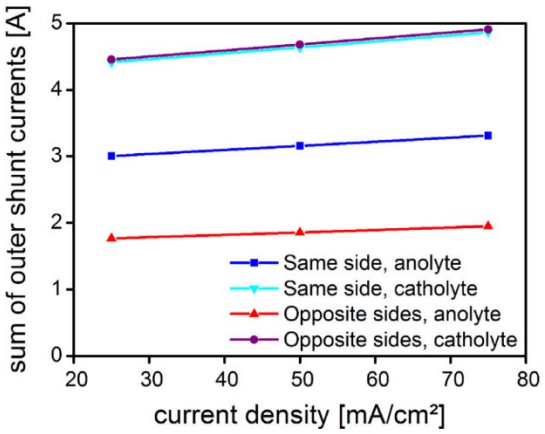

Figure 4.17: Shunt current trend changing the current density [10]

The research assesses the system's Coulombic and energy efficiencies at varying current densities. Coulombic efficiency reaches a peak of 99.1% when there are no pipe connections between the stacks, this is due to the lack of shunt currents. On the other hand, the introduction of pipe connections leads to a reduction in Coulombic efficiency, dropping to 95.3% in the same-side configuration and 95.9% in the opposite-side configuration. Energy efficiency diminishes more significantly than Coulombic efficiency because shunt currents bypass the electrochemical conversion and also dissipate energy as heat. As the current density increases, the drop in efficiency becomes more pronounced, with energy efficiency decreasing to as low as 68.6% in the same-side configuration at higher current densities. So, for the round-trip efficiency lower current densities are better, because with higher ones the Coulombic efficiency increases slightly, but the energy efficiency decreases significantly.

In conclusion, the study explores different charging cycles and the effect of pipe configurations connecting the stacks. The findings highlight that as the state-of-charge increases, so does the shunt current, which can double at high states of charge. External pipe connections introduce additional shunt currents, leading to a loss in Coulombic efficiency, particularly as more cells are added to the stack. Simulated results also suggest that pipe connections cause unequal shunt current distribution, which may result in corrosion (the details regarding the issue of corrosion will not be discussed), as also highlighted in an article by W.R. Bennett et al. [11].

A paper published by F. Xing et al. [12] confirms the findings of the last considered study [10] even for a different model, mentioning other useful considerations.

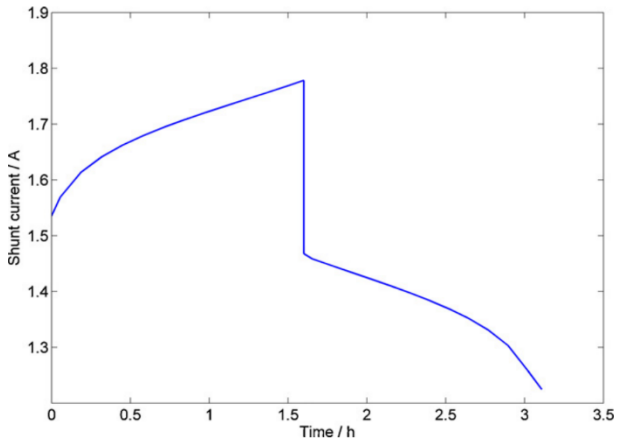

Figure 4.18: Shunt current charge/discharge cycle with a current density of 80 mA/cm^2 [12]

The shunt current is affected by the voltage of a single cell, the series arrangement of cells, and the resistances present in the manifold and channel. Figure 4.18 illustrates the variation of shunt current during the charge/discharge cycle (similar to the one seen in figure 4.16) at a current density of 80 mA/cm², indicating a correlation with the voltage of an individual cell. With an increase in the number of cells connected in series, there is also an increase in the circuit loops contributing to the shunt current. This phenomenon was analyzed by calculating the shunt current in a stack of 20 cells and comparing it with the internal current in a stack of 10 cells. Thus, reducing the number of cells in series proves to be an effective way to minimize shunt current.

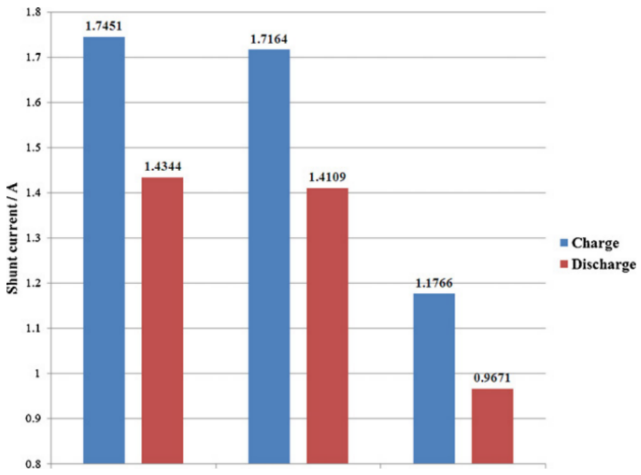

Figure 4.19: In order, shunt current values with the original resistance, with increased manifold resistance, and with increased channel resistance [12]

The shunt current diminishes as the resistances of the manifold and channel rise. Research investigating the impact of resistance on shunt current revealed that a 50% increment in the resistances of both the manifold and channel results in a decrease in shunt currents by 1.64% and 32.57%, respectively, as shown in figure 4.19. This suggests that a comparable percentage rise in resistance exerts a greater influence on the reduction of shunt currents in the channel than in the manifold. This result may seem like contradicting the results of the last paper, visible in figure 4.14, but it is not true since in the previous case the resistance was increased by 30 times and not just 50% and the overall setup of the two VRFB may differ. Figure 4.20 describes the shunt current loss across different applied current densities. With the increase in current density, there is a decrease in both the absolute value of shunt current loss and its share of the overall Coulombic loss. This decrease in shunt current loss is attributed primarily to the reduced duration of charge and discharge cycles at elevated current densities. Concurrently, the diminished proportion of total Coulombic loss corresponds to the enhanced power output from the stack. In this experiment, shunt current loss contributes to less than 17% of the total Coulombic loss. Keeping the number of cells and the electrode area constant, increasing the applied current density is an effective strategy for minimizing shunt current loss.

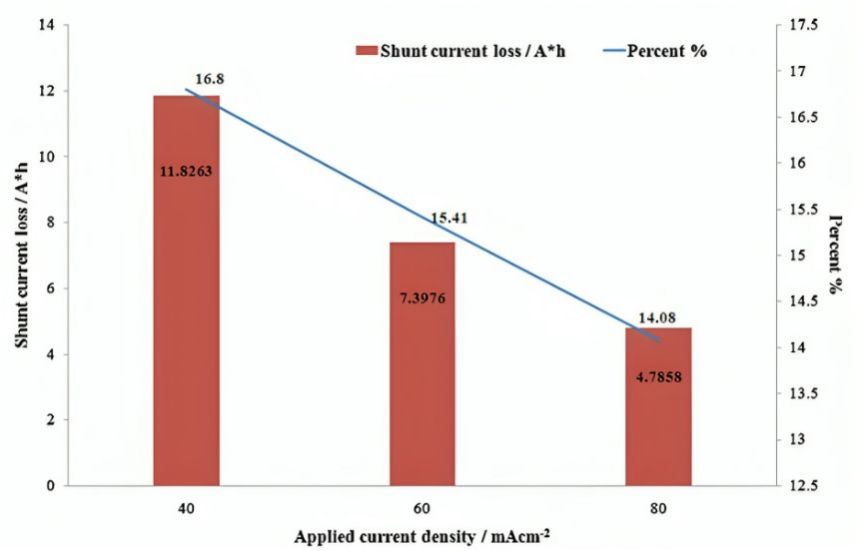

Figure 4.20: Shunt current losses increasing current density [12]

In conclusion, the paper published by F. Xing et al. [12] offered even more insight into shunt current behavior considered in the paper by C. Yin et al. [10].

As already seen and mentioned pipe connections and dimensions play a key role in the magnitude of shunt currents and the following paper puts into correlation the dimensions of the piping system (for a total of 21 different hydraulic designs) with the Coulombic efficiency and the overall system efficiency. The paper, written by S. Konig et al. [13], provides lots of interesting considerations about the hydraulic circuit of a VRFB system, crucial for understanding some of the variables that affect shunt currents. While the minimum pipe lengths are dictated by the physical size of the system's components, such as tanks and equipment, there is more flexibility in selecting pipe diameters. Increasing the length of pipes could help reduce certain undesired effects, but it would also require more space and complicate the system's layout, so this approach is not considered here. A generic hydraulic model, based on classic industrial configurations, is used to determine the lengths of both main and branch pipes, as well as the number of bends and junctions (useful information to consider the pressure drops). The dimensions of the system components are taken from established references. To calculate pipe diameters, it is essential to know the maximum required flow rate of fluid through the system, which depends on the maximum operational output. There is a distinction between main pipes and branch pipes: the main pipe connects to the primary fluid reservoir and handles the total flow, while the branch pipes, which connect individual components to the main pipe via junctions, are responsible for supplying each component individually. The maximum output is determined at the operational point when the system is functioning at peak demand. At this stage, the operational voltage is at its lowest, requiring the highest flow rate to maintain the specified output. Based on simplified calculations that consider only resistance losses, the necessary flow rate at this critical point can be determined. It is important to note that, as the system approaches the end of its operational cycle, certain parameters may fall below their minimum limits. For example, concentration changes in the fluid may lead to a lower limit for the system's performance, requiring adjustments in the model. In this case, the system needs to deliver a specific power output, which translates into a calculated flow rate of fluid for each unit in the system. Using the hydraulic model, different pipe diameters are evaluated to find an optimal configuration. A design is considered appropriate if it ensures that all components receive the required flow rate without exceeding the maximum power capacity of the pumps, and ideally, all components should receive an equal flow. Achieving the required flow rate is not feasible with branch pipe diameters below a certain threshold if the main pipe is also undersized, due to the limited power available to the pumps. For larger pipe diameters, the power required by the pump closely aligns with the power needed to overcome the resistance in the system. Differences in fluid distribution across the system should also be taken into consideration. When the main pipe diameter exceeds a

certain value, the variation in flow rate between the best and worst-supplied components remains minimal, representing only a small percentage difference relative to the total flow rate. From a fluid dynamics perspective, a main pipe diameter of 250 mm and a branch pipe diameter of 80 mm appear optimal for minimizing pump power losses while avoiding excessively large pipes. Additionally, several other design variations are assessed, using combinations of different main and branch pipe diameters, to explore alternatives and confirm the optimal setup. The results of the simulation are observable in the following figures:

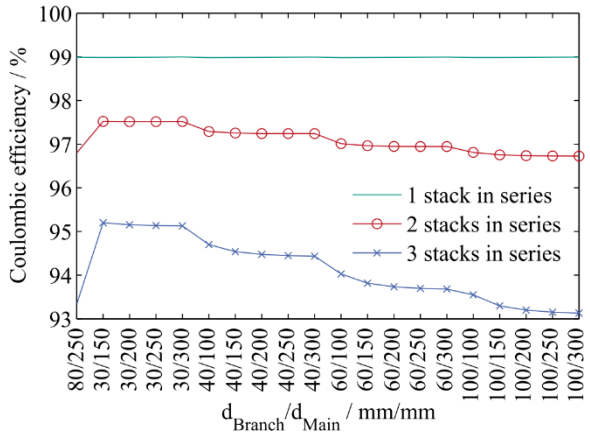

Figure 4.21: Coulombic efficiency depending on the pipes diameter and number of stacks [13]

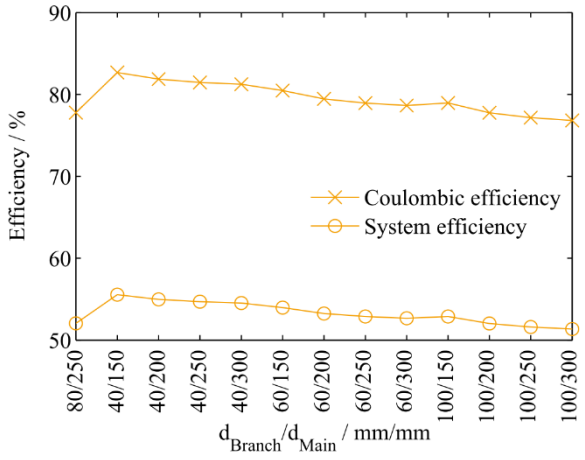

Figure 4.22: Efficiency depending on the pipe's diameter [13]

Figures 4.21 and 4.22 illustrate the average Coulombic and system efficiencies across all valid designs. Systems with six stacks in series are highlighted separately due to their significant efficiency trend deviation from other configurations. The average efficiencies were calculated

by taking the means of round-trip efficiencies at 25%, 50%, 75%, and 100% of rated power, assuming a uniform distribution of battery power levels during operation. Different probability distributions could yield different optimization outcomes. Variations in pipe diameter, dictated by the volumetric flow rate, minimally impact the efficiency of systems that do not have stacks in series. Although narrower pipes marginally increase pump losses, the system efficiency variance between the smallest and largest pipe designs is negligible, about 0.1%. The reference design, with main and branch pipe diameters of 250 mm and 80 mm respectively, is considered optimal. In systems that have multiple stacks in series, the hydraulic circuit design becomes increasingly critical. However, the impact is relatively minor when only two stacks are in series. The effect is more significant with a greater number of stacks, particularly when connecting three stacks in series.

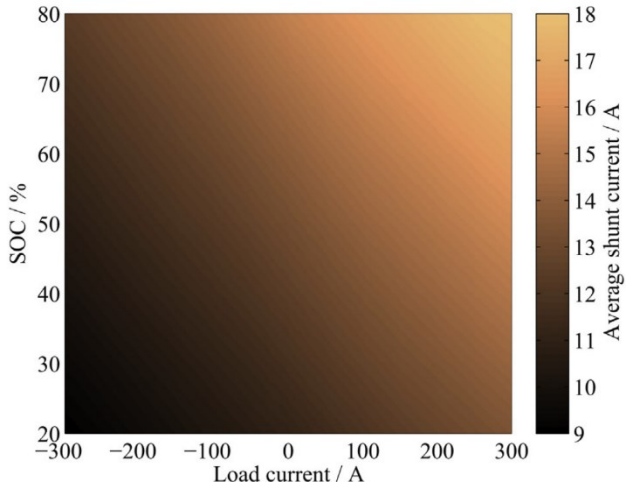

Figure 4.23: Shunt current for six stacks in series over SOC and load current [13]

Shunt current losses are anticipated to be significantly affected by the series connection of battery stacks, with losses increasing in a near-quadratic fashion as additional stacks are connected in series. The correlation between shunt currents, state of charge, and load current is depicted in figure 4.23 for a system comprising six stacks. The data indicate that the average shunt current escalates with SOC. Shunt currents rise with higher load currents during charging, whereas they diminish as load currents increase during discharge. At low power levels, cycling operations do not see substantial shunt current reductions due to inherently lower load currents. Furthermore, the impact of shunt currents is more evident as the ratio of load current to shunt current deteriorates at lower load currents, thus becoming a more significant consideration during cycling at reduced power levels.

To sum up, the paper demonstrates that is necessary to find a break-even point between hydraulic and shunt current losses, as also highlighted in another article by A. Trovò et al. [14].

Another useful publication for expanding shunt current knowledge is the one by H. Fink and M. Remy [15]. The article directly examines the shunt currents in a five-cell mini-stack vanadium flow battery equipped with an external hydraulic system. The setup allows for the integration of current sensors to accurately measure the shunt currents. Moreover, the shunt currents between cells can be halted by clamping the tube couplings, which blocks the individual bypass channels when the pumps are not in operation. This method facilitates the independent assessment of losses attributed to cross-contamination and shunt currents via charge conservation measurements. Besides considerations that were already seen in previous papers, the article studies how shunt currents affect the voltage distribution between single cells. Figure 4.24 illustrates such phenomena, where OCP stands for open circuit potential, which refers to the equivalent circuit seen in figure 4.1:

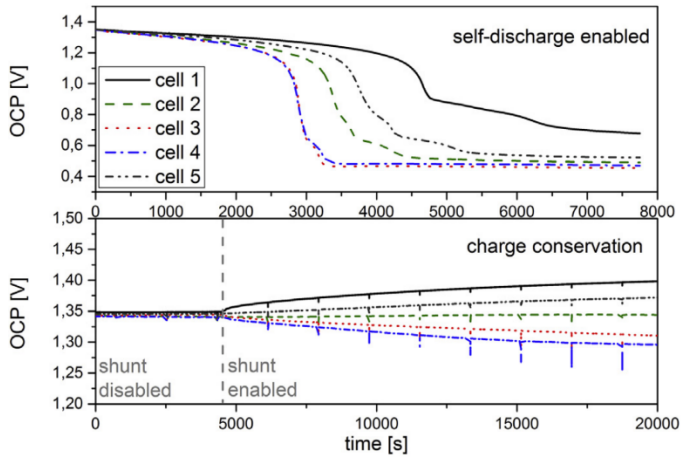

Figure 4.24: Open circuit potential with the presence of shunt current [15]

The potentials of individual cells in the mini stack were evaluated at different operational states to assess the influence of shunt currents on cell performance, as shown in figure 4.24. By securing or releasing the external fluid connections, the shunt connections between the cells could either be deactivated or activated, with pumps turned off during these measurements. The observations indicated that internal cells discharged more quickly. Furthermore, self-discharge appeared to be reversible in the absence of shunt currents. However, shunt currents caused an irreversible ion redistribution within the stack, resulting in fluctuating potentials of individual cells while the total stack potential stayed unchanged. This irregularity in cell potentials is likely a consequence of the cells' non-ideal characteristics. In scenarios where charge is conserved, internal cells are prone to discharging, whereas external cells accumulate

charge. In a galvanically isolated stack, all cells discharge, but central cells do so at a faster pace than peripheral ones. The simulation model corroborates this interpretation, forecasting similar balancing currents during charge conservation.

This paper also provides shunt current trends for high numbers of cells, thanks to the applied model. The results are shown in figures 4.25 and 4.26:

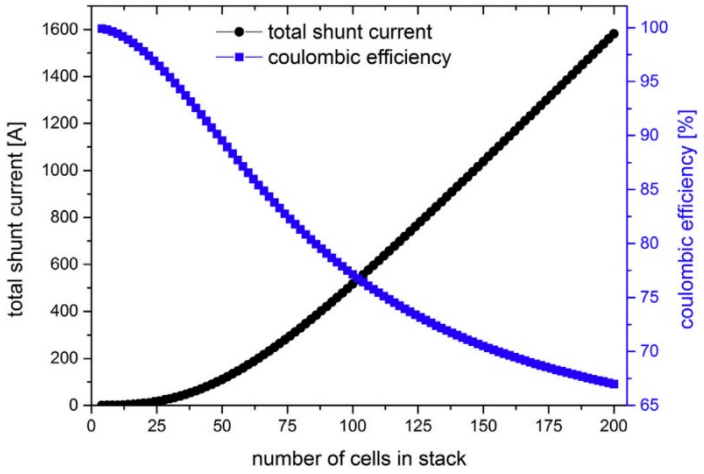

Figure 4.25: Shunt current and coulombic efficiency depending on the number of cells [15]

Figure 4.25 illustrates the total shunt current for the standard resistance values across stacks containing between five and 200 cells. Coulombic efficiency was calculated based on an active cell area of 1000 cm² and an operational current density of 40 mA/cm². The assessment focused solely on losses attributed to shunt currents, without factoring inside reactions or cross-contamination.

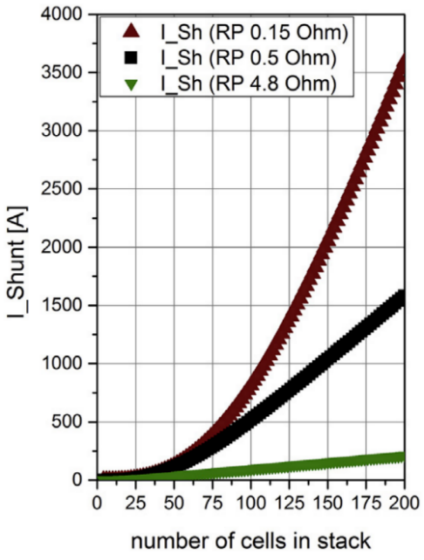

Figure 4.26: Shunt current values with different channel resistance [15]

The study by N.M. Delgado, R. Monteiro, J. Cruz et al. [16] deserves mention since not only it utilized artificial intelligence in the research but also introduced a strategy to increase the resistance of the manifold, which is the use of "dumping cells", that are non-electrochemical cells inserted into the stack. These cells assist in "dumping" shunt currents, preventing their circulation through the electrochemical cells, thus diminishing their effect on overall performance by extending the manifold's length. While the design of these cells may resemble that of a bipolar plate, their functions are distinct. The research indicated that incorporating dump cells could significantly reduce shunt current losses without affecting the stack's power output even though they produce pressure drops.

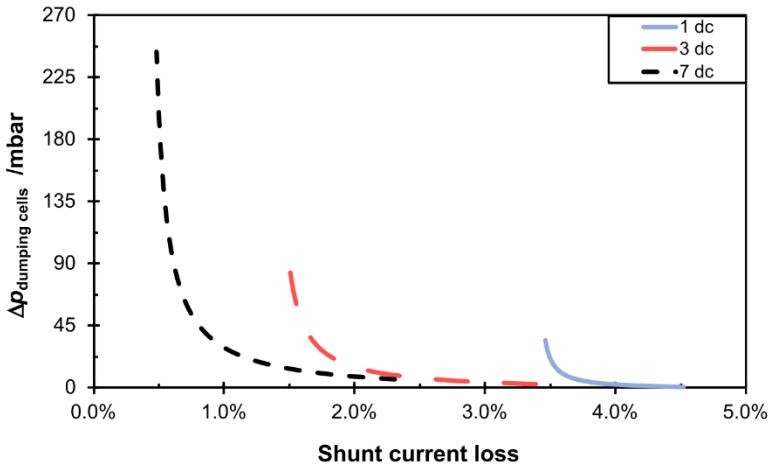

Figure 4.27: Shunt current loss and pressure drop for different number of dumpling cells [16]

Additionally, a sensitivity analysis was performed to determine the most influential factors on shunt currents. It was examined the effects of external resistances (R_c and R_m) on shunt currents to improve stack design. It takes into account critical factors such as the operating current (I) and the number of cells in a stack (N), both of which determine the shunt current levels. However, compared to previous paper, this study also introduces a sensitivity index (SI) correlated with the average rate of change ($\overline{m}$) of shunt current loss. By employing an equivalent circuit model (figure 4.1), the analysis simulates a stack with N cells at a uniform state of charge of 50%, during both charging and discharging phases. The internal resistance of each cell is fixed at 0.0045 Ω, indicating its negligible impact on shunt currents. Shunt current losses were assessed for different R_m, R_c, I, and N combinations, yielding results from a mere 5.0×10^{-4}% to a significant 99.9%. Remarkably, about 60% of the simulations showed shunt current losses below 1%. Such low losses occurred when R_m was over 327 Ω, or through specific R_m, R_c, I, and N combinations. A stack with an R_m exceeding 327 Ω could streamline flow frame design and manufacturing. Nonetheless, a conventional stack with an R_m above

327 Ω might be unfeasible, necessitating either a too-large gap between cells or a very narrow manifold. Therefore, investigating alternative stack designs becomes imperative.

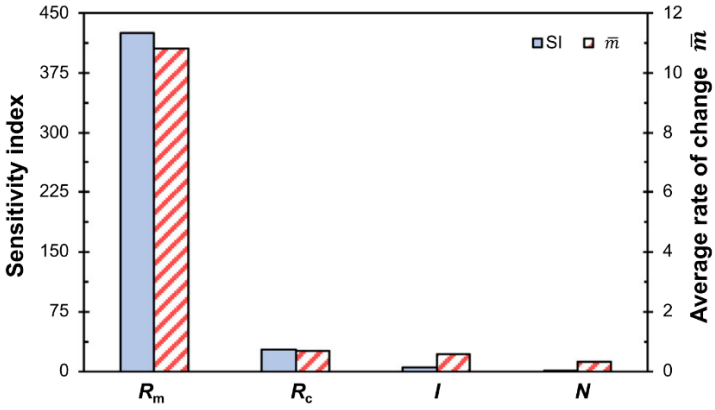

Figure 4.28: Sensitivity index for different parameters [16]

The analysis revealed that manifold resistance has the most significant effect on shunt currents, with the resistance of the flow frame channels and the operating current also being important factors. Notably, the number of cells in the stack plays a crucial role, as larger stacks are prone to higher shunt currents. This increase is due to the greater potential difference between the first and last cells in the stack as the number of cells grows, resulting in increased shunt currents.

4.4 Thermal effect of shunt currents

The typical night temperature in the considered environment ranges from 5°C to 15°C depending on the season. For the simulation, it is assumed that the room temperature remains constant at 10°C, and the initial temperature of the stack electrolyte is set to 15°C.

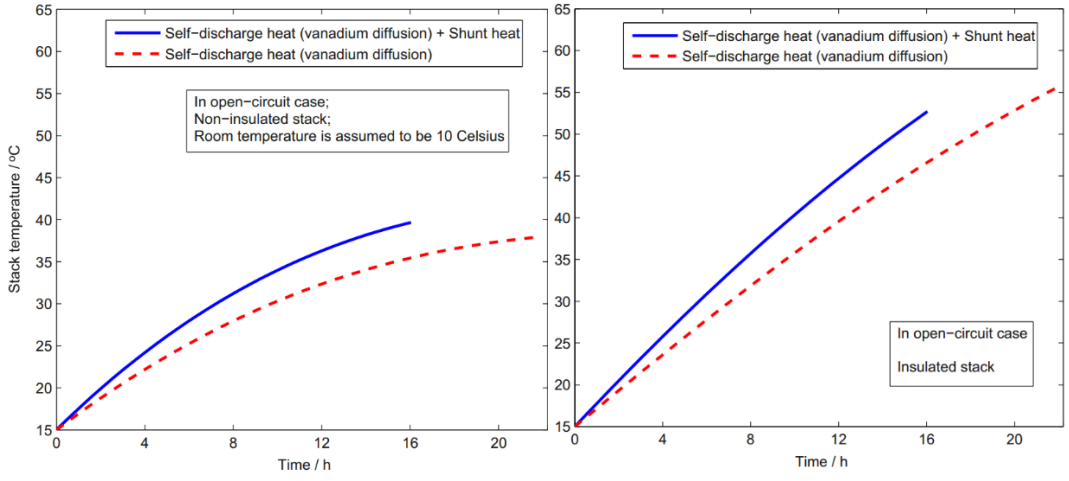

Figures 4.29 and 4.30: Stack temperature variation at open circuit without and with insulated stack [17]

Based on these assumptions, simulations were conducted to observe the variations in stack temperature for both non-insulated and insulated stacks, as shown in figures 4.29 and 4.30. Figure 4.29 demonstrates that in a non-insulated stack, the temperature can rise to 40°C after 16 hours and will continue to increase until the V_2^+ and VO_2^+ are fully depleted. Considering the thermal effects of shunt current in the model, it is predicted that the stack temperature will rise more quickly than in cases where only self-discharge heat from vanadium diffusion is generated.

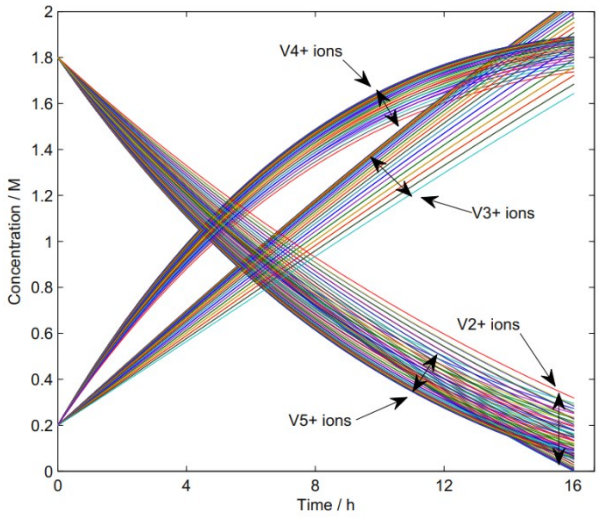

Figure 4.31: Ion concentration variations due to discharge in all cells at open circuit [17]

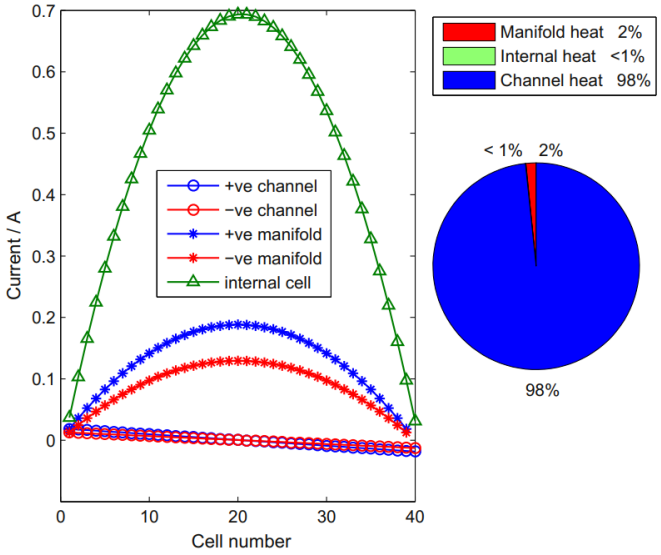

Figure 4.32: Current distribution in the stack at 50% SOC [17]

Figure 4.30 presents the temperature variations in an insulated stack. Without environmental heat exchange, stack temperatures can exceed 50°C in both cases. The stack temperature in the complete model reaches its maximum faster due to shunt current ohmic loss and internal discharge heat. Figure 4.31 illustrates the variation in vanadium ion concentrations across all 40 cells in open-circuit conditions, showing that central cells experience self-discharge faster than the end cells due to the presence of shunt current. This is further depicted in figure 4.32, which shows the currents in channels, manifolds, and cells at 50% SOC. The stack temperature will continue to rise until all V_2^+ and VO_2^+ are depleted in individual cells.

By comparing the cell temperatures in figures 3.29 and 3.30 with the VO_2^+ concentration profiles in figure 4.31, it is possible to predict the VO_2^+ ion concentration when the stack temperature reaches 40°C, which is the threshold for thermal precipitation of V_2O_5. Under the current design, thermal precipitation is not expected because the VO_2^+ concentration will have decreased to a low level by the time the stack electrolyte temperature reaches 40°C.

Figure 4.32 also shows the contribution to ohmic dissipation at 50% SOC in open circuit, indicating that heat from channel resistances to shunt currents plays a dominant role despite the smaller current flow compared to manifold and internal cell currents. This is attributed to the long length and small cross-sectional area of the channel in the flow-frame design, which results in significant ionic resistance. Alongside ohmic heat dissipation, both internal discharge and self-discharge heat contribute to the rise in stack temperature in open-circuit conditions.

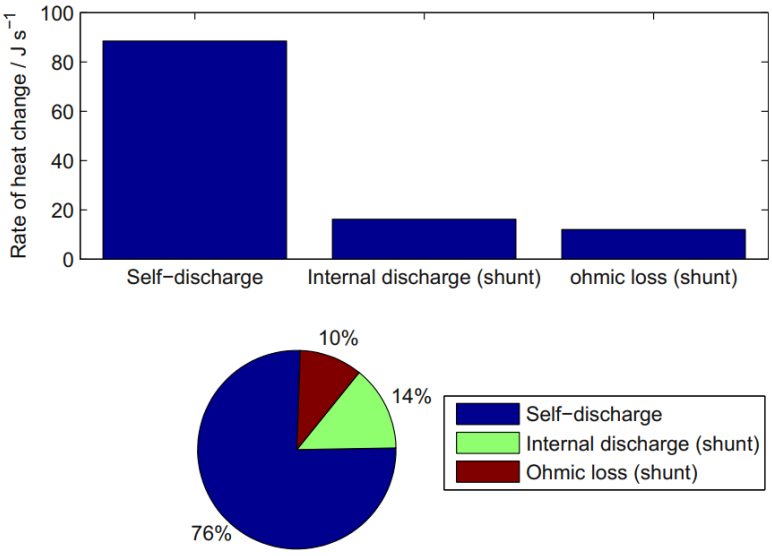

Figure 4.33: Different sources of heat generation at 50% SOC [17]

Figure 4.33 compares the three factors contributing to heat release in the stack by both the rate of heat change and proportions at 50% SOC, showing that self-discharge due to vanadium ion diffusion is the major contributor to the increase in stack temperature among the three factors. Shunt current impacts (internal discharge and ohmic loss) are also significant, though their relative contributions can change significantly with a poor flow-frame design, highlighting the importance of shunt current reduction in bipolar stacks.

By using predictions from the complete thermal model along with a battery management system, control actions can be implemented to lower the stack temperature before it exceeds the VO_2^+ thermal precipitation point, which varies with the electrolyte composition in open circuit. This might involve restarting the pumping system briefly to circulate the electrolyte between the tanks and stack. Additionally, the complete thermal model could aid in designing an advanced temperature control system to assist in cooling the electrolyte in the reservoirs when necessary, during charging or discharging.

Another study [18], reported by A. Trovò et al., provides a stand-by thermal model for vanadium redox flow batteries. In this paper also shunt current effects are considered and those will be analyzed now. The heat generation in the stack is due to the presence of shunt currents that cause Joule losses in the pipes and manifolds. Another important aspect is that the generation of shunt currents due to electrochemical reactions causes an additional self-discharge in the VRFB. Numerical results show that shunt currents affect the temperature in the stack and can be responsible for local increases of cell temperatures up to 10 °C if the solutions are initially at high state of charge. This effect can be critical if standby occurs after a period of operation, with the electrolyte stack temperature markedly higher than air temperature. In addition, results show that shunt currents can play a major role in the thermal behavior of compact stacks, based on new materials capable of high-power density and low ion crossover. The model presented here can constitute the basis for advanced cooling strategies.

A common side effect in standby mode is the occurrence of shunt currents. These are often overlooked in single-cell configurations but are unavoidable in parts of hydraulic circuits in stacks with bipolar connections. The cause is the conductivity of the electrolytic solutions that supply the cells in parallel via manifolds and pipes, which have different electrical potentials. Shunt currents lead to Joule losses, which cause an increase in temperature. Furthermore, sustaining these shunt currents requires electrochemical reactions inside the cells, contributing to both self-discharge and additional heat production.

The VRFB in question is a 9 kW stack composed of 40 cells, presently operational at the Electrochemical Energy Storage and Conversion Laboratory at the University of Padua and is appropriate for industrial production and commercialization. In a high-power-density stack such as this, shunt currents can significantly influence the standby thermal behavior. Validation was performed using a thermal imager, which facilitated the comparison of numerical and experimental temperature distribution values on the stack's lateral surface. The mathematical and circuit models considered are the ones already mentioned previously. The main equations, reported by the paper, in order to calculate shunt current losses in terms of power and heat Joule losses are the following, where the subscripts refer to the channel (c), the manifold (m), the positive and negative electrodes (+ and -) and n refers to the n-th manifold or channel:

$$P_{c+,n} = I_{c+,n} v_{c+,n} \tag{4.27}$$

$$P_{c-,n} = I_{c-,n} v_{c-,n} \tag{4.28}$$

$$P_{m+,n} = I_{m+,n} v_{m+,n} \tag{4.29}$$

$$P_{m-,n} = I_{m-,n} v_{m-,n} \tag{4.30}$$

$$Q_{sc} = P_{m+,n-1} + P_{m-,n-1} + P_{c+,n} + P_{c-,n} + P_{i,n} \tag{4.31}$$

In the last equation (4.31) $P_{i,n}$ is the power lost due to the intrinsic resistance of the cell, seen in the equivalent circuit in figure 4.1. So, we can define a general P_i as:

$$P_i = R_{cell} I_{cell}^2 \tag{4.32}$$

The next graphs provide the trend of shunt currents in the manifolds and channels, demonstrating that even in industrial-scale applications, these trends are very similar to the ones obtained from mathematical models:

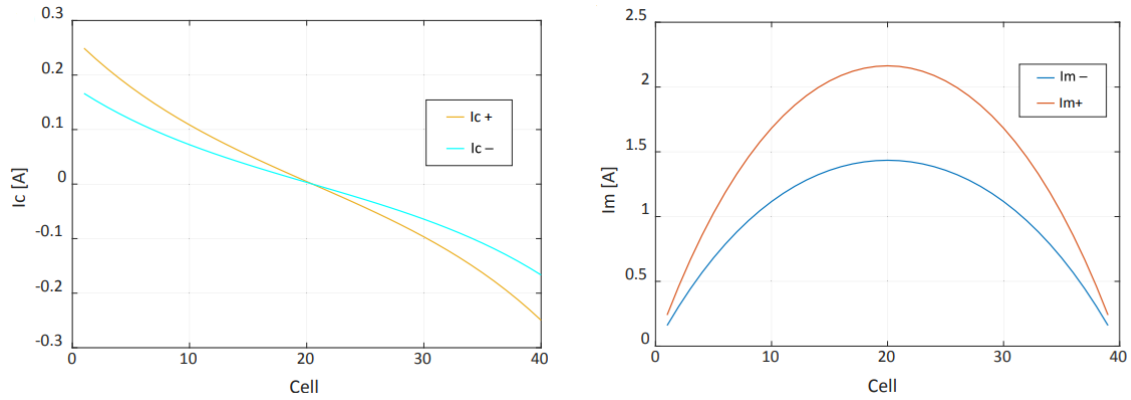

Figure 4.34: Shunt current values in the channels and the manifolds respectively [18]

Even in this paper, as in the studied previous one, it is shown how ion concentration differs with the presence of shunt current. However, the main takeaway of this paper is present in figure 4.35:

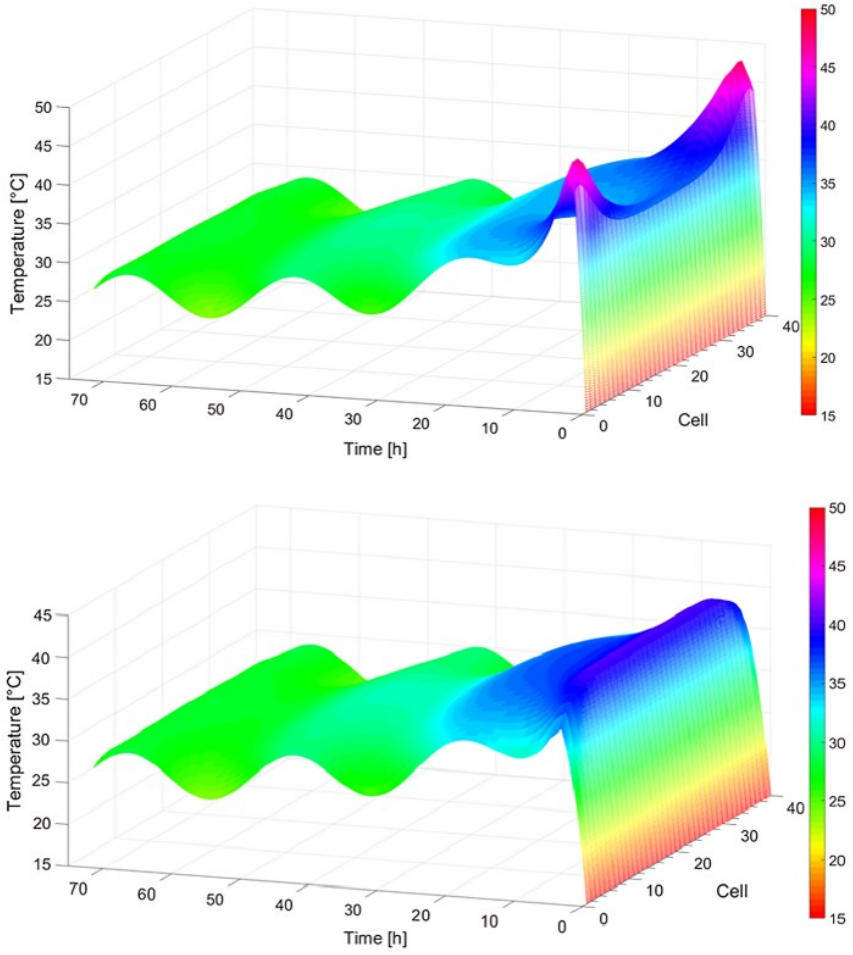

Figure 4.35: Simulation for cells temperatures with (above) and without (below) shunt current [18]

The numerical results precisely mirror the spatial temperature distribution noted in the measurements, with the coldest cells located at the center of the stack and the hottest at the extremities. This distribution is due to the cell-channel shunt currents, which are stronger in the cells at the ends. Conversely, the manifold shunt currents peak in the center, yet these hydraulic segments possess significantly lower electrical resistances, resulting in minimal Joule losses. It should be noted that the model accurately replicated the cell temperature distribution, with the elevated values near the terminal cells being solely attributable to the shunt current losses.

4.5 Shunt current and round-trip efficiency

The reduction of shunt current has a key role in increasing the overall efficiency, also called round-trip efficiency, of the VRFB systems. But it is also very important to understand that some solutions implemented to reduce shunt currents may lead to a decrease in the round-trip efficiency. This issue is crucial to critically analyze in the next chapter the considered patents.

A paper by Q. Ye et al. [19] provides a complete view of the design trade-offs in VRFBs. The authors present a detailed analysis of these design trade-offs using case studies of multi-stack VRFB systems, demonstrating how certain designs can minimize both shunt current and electrolyte flow resistance. The study's methodology is based on the development of an analog circuit model to simulate the electrochemical system and a flow network model to understand the fluid dynamics of the piping system. The research indicates that employing thicker and longer ducts may reduce shunt current and pressure drop, but it results in a bulkier system. Consequently, the design must have a middle ground between the system's compactness and its operational efficiency. A major hurdle in designing VRFB systems is the control of parasitic energy losses. While the round-trip energy efficiency of a standard VRFB stack might exceed 85%, the total system efficiency often falls below 60% due to cumulative losses from pumps, converters, power management, and thermal control systems. The energy loss from shunt currents can be significant, especially in large-scale systems where the series connection of many individual cells exacerbates the problem. Consequently, minimizing the shunt current becomes a primary goal in the design of VRFBs. The use of longer pipes reduces the cross-sectional area through which shunt currents can flow, but the increased length adds to the system's hydraulic resistance, leading to higher pumping losses and costs.

The analysis of shunt current and pumping loss is based on principles of fluid mechanics and circuit theory. The resistance a pipe presents to electrolyte flow is inversely related to the square of its diameter, while the pressure drop from laminar flow is inversely related to the diameter's fourth power. Consequently, minor variations in the pipe's diameter can greatly influence both shunt current and pumping loss. The electrical resistance R of a circular pipe is given by the equation:

$$R = \frac{4L}{\pi k D^2} \tag{4.33}$$

where L is the length of the pipe, k is the electrolyte conductivity, and D is the diameter of the pipe. The pressure drop ΔP is given by:

$$\Delta p = \frac{128 \mu Q L}{\pi D^4} \tag{4.34}$$

where μ is the viscosity of the electrolyte, and Q is the volume flow rate. These equations underscore the challenge of designing a piping system that balances the need for high electrical resistance to minimize shunt currents with low flow resistance to reduce pumping losses.

The study delves into the importance of flow distribution in multi-stack VRFB systems. Achieving optimal performance necessitates a uniform distribution of the electrolyte across all cells in each stack to prevent localized overcharging or undercharging, which can reduce both efficiency and the lifespan of the battery. The study presented in the paper indicates that a Z-type flow configuration, which positions the inlet and outlet manifolds on opposite sides of the stack, achieves a more even flow distribution than a U-type configuration, where both are on the same side. Simulations on a 15-kW VRFB module evaluated different piping designs, taking into account variables such as the number of stacks, ranging from 2 to 12 in this study, as well as the length and diameter of the pipes, and the electrolyte flow rate. The findings demonstrate that shunt current losses increase exponentially with the number of cells per stack (as seen in previous papers), thus underscoring the advantages of using smaller stacks. For instance, in a system comprising 120 cells in series, segmenting the cells into smaller stacks containing 15 to 30 cells each can markedly diminish shunt current losses. This method necessitates the creation of longer and more intricate piping networks, which could result in increased pressure drops and higher pump power requirements. A case study indicates that a system comprising eight stacks and broad pipes minimizes total energy loss, with shunt current losses at approximately 0.9% and pumping losses at 1.71%. However, this configuration leads to an increase in the system's size. On the other hand, a more compact design with fewer stacks and shorter pipes can decrease the overall size of the system, but it may also lead to an increase in shunt current losses of about 4%. Consequently, it is crucial to optimize the electrodes' geometry, since the size and thickness of the porous electrode greatly affects the voltage efficiency and pumping losses. In general, it is recommended to use thicker electrodes to minimize pressure drops and enhance the system's overall efficiency. An additional suggestion is to employ multi-stack configurations. Dividing the cells into several stacks, especially in larger systems, can diminish shunt current losses and thus improve performance. Additionally, selecting appropriate pipe dimensions is critical. While longer and thicker pipes can help balance shunt current and pumping losses, the system's overall size must be carefully considered. The paper also advises adjusting the flow rate based on operating conditions. Implementing variable flow rate schedules can diminish pumping losses while maintaining system performance, thus adding flexibility. The provided insights serve as valuable guidelines for attaining the best balance in VRFB piping system design. The study zeroes in on a VRFB system functioning at a standard current density of 60 mA/cm^2 and a vanadium concentration

of 2 mol/l. In an eight-stack configuration, shunt current losses are approximately 0.9%, leading to a total system efficiency loss of 2.64%. Increasing the stack count from two to eight cuts shunt current losses by almost half, though it results in greater system complexity. Pumping losses can potentially be decreased to around 1.71% by employing pipes that are both longer and wider, although this might result in a more cumbersome system. The following graphs shows the round-trip efficiency losses for different designs and different flow rates:

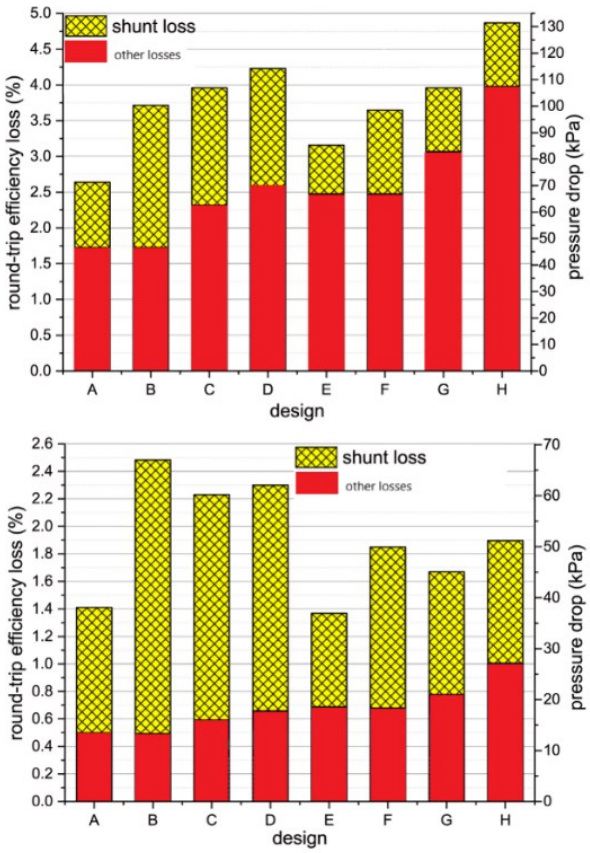

Figure 4.36: Shunt losses at normal flow (above) rate and at low flow rate (below) [19]

The designs B, C and D are the ones that least focus on shunt current reduction, but it is clear from figure 4.36 that it does not automatically mean that these designs have the lower round-trip efficiency. In fact, it is observable that for higher flow rates other designs that focus mainly on reducing shunt currents present higher overall losses, for example, design H.

The research highlights the intricate compromises required to enhance the performance of VRFB systems. Through careful examination of these design factors, one can develop a system that successfully harmonizes efficiency, size, and complexity.

5. Patents investigation

Analyzing patents is a critical step in the process of innovation and problem-solving, offering a wealth of valuable information that can lead to concrete solutions. By thoroughly examining these documents, it is possible to uncover existing technologies, methodologies, and approaches that have already been tried and tested. Moreover, patent analysis allows for the identification of gaps in the current knowledge base, revealing opportunities for new developments.

5.1 Shunt resistor

Patent US20120308856A1 by Craig R. Horne et al. [20] shows multiple devices implementable in the vanadium battery system. More precisely, these devices can be implemented in the position marked in red in figure 5.1.

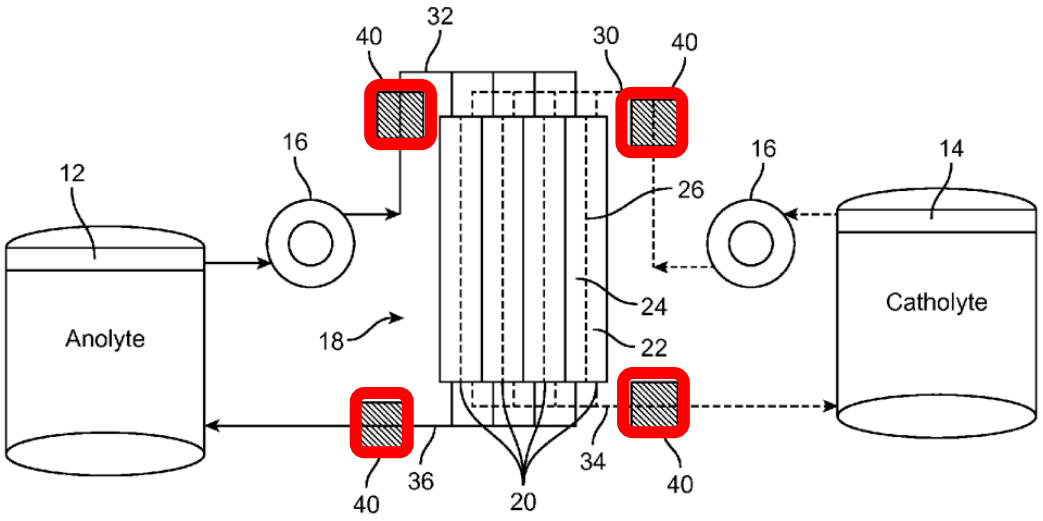

Figure 5.1: Layout of a flow battery [20]

Figure 5.1 provides useful information: the devices, called shunt current resistors, are located at the inlets and the outlets of the main flow channels of both electrolytes. Knowing this it's already possible to understand that these shunt current resistors increase the intrinsic electrical resistance of the electrolytes flow by altering the direction of the flow, without significantly decreasing the flow rate. As declared on the patent, the electrical resistance is increased by interrupting the physical continuity of the liquids through their length. Some of these devices can also be regulated with a feedback system in order to provide better flow control.

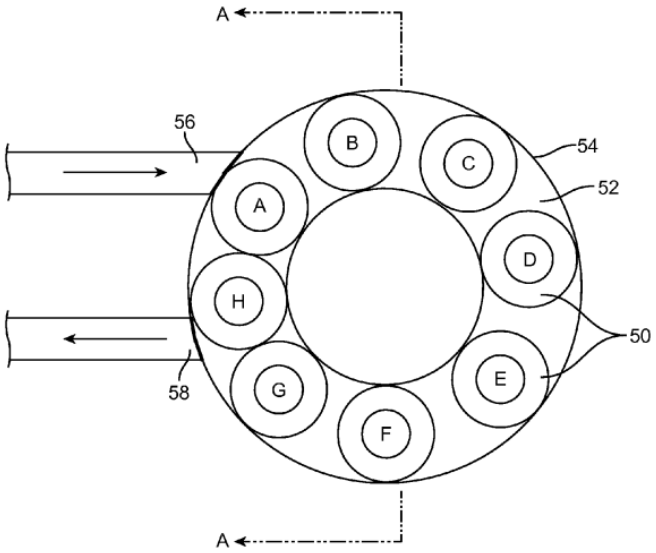

Figure 5.2: Toroidal shunt resistance cross-section [20]

The shunt resistor depicted in figure 5.2 functions by trapping fluid within the space bordered by dividers, labeled 50. The dividers in figure 5.2 are marked from “A” to “H” following a clockwise sequence. When fluid flows into the gap between the first pair of dividers, A and B, this space expands due to the rising fluid pressure at inlet, labeled 56, which propels dividers B to H clockwise. This expansion persists until the pressure downstream pushes divider A to also move clockwise. Consequently, the gap between A and H widens as it becomes filled with fluid. As divider H passes outlet port, labeled 58, the fluid confined between dividers H and G is discharged through outlet. Following this, the gap between H and G narrows until the dividers make contact. The dividers can be designed to fit within channel, labeled 52 with minimal clearance, thereby reducing the volume of fluid that can bypass the dividers. This reduction in clearance decreases the cross-sectional area of the liquid that is in shared communication between chambers, consequently increasing the electrical resistance (as seen in the equation (4.4)) across a divider within channel. Dividers can consist of freely moving solid objects, such as spheres or various shapes, constructed from materials that are electrically non-conductive and chemically non-reactive, guaranteeing they do not deteriorate in the electrolyte solution. These dividers might be hollow, with a wall thickness that is deemed appropriate. Additionally, the hollow dividers could be filled with an inert liquid or gas.

The device basically modifies two of the values of the defining equation (4.4) of the electric resistance, reported again below:

$$R = \frac{l}{\sigma A} \tag{4.4}$$

The length of the pathway l of the flow is increased with the passage through the toroidal device, whereas the cross-section A is decreased by the dividers.

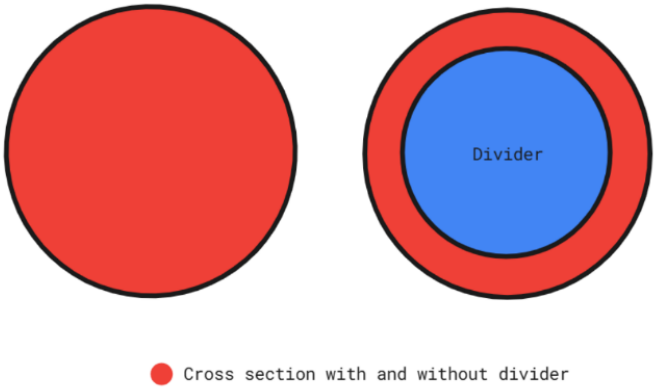

Figure 5.3: Cross-section of the toroidal embodiment with and without divider

Although this device offers a feasible solution, there are some technical problems that are not covered by the author of the patent. The dividers cannot be mechanically controlled, not allowing any sort of flow control within the device. For smaller dividers, there is a chance that they may exit the device through the flow outlet, leading to pipes blockages. In the patent an example is mentioned: it states that for a channel with a cross-sectional diameter of around 1 cm the device housing has a mean toroidal diameter of around 12.5 cm. In spite of the overall volume of the shunt resistor not being substantial, the clutter of the devices is not negligible, especially considering its implementation in large-scale VRFB systems. Also, the dividers have to be lightweight to avoid an excessive obstruction of the flow, leading to increased pumping losses.

Another shunt resistance, figure 5.4, very similar to the one just analyzed is proposed by the author. The concepts applied are the same as the shunt resistance in figure 5.2, however in this case the flow rate can be controlled.

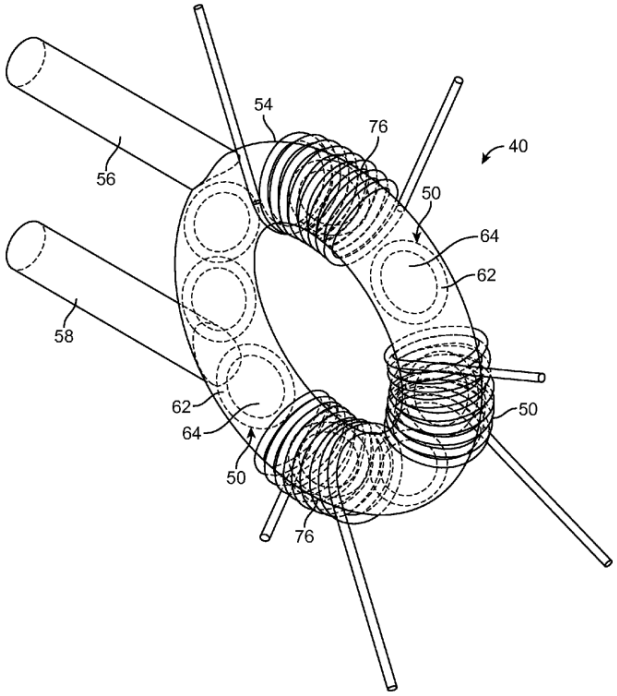

Figure 5.4: Toroidal shunt resistance with coils [20]

In this case, applying an electric current to one of the coils, labeled 76, will generate a magnetic field in accordance with the right-hand rule. This field will attract the opposite poles and repel similar poles of the magnetic cores in the adjacent dividers, labeled 50. By timing the electric currents to the coils, the resulting magnetic fields can be regulated to produce magnetic forces that create resistance to the forward motion of the dividers through channel, labeled 54. Altering the magnitude of the electric currents in the coils alters the intensity of the magnetic forces on the dividers. Therefore, by managing the timing and intensity of the electric currents, the device in figure 5.4 can regulate the flow rate of circulating electrolytes, thus controlling the back pressure of the fluid moving from inlet to outlet, labeled 56 and 58 respectively. In a similar manner, the device in figure 5.4 can function as a pump to enhance the flow rate of electrolytes from the inlet to the outlet.

Besides the fact that in this case the flow rate can be regulated, this design presents the same issues as the previous one. Not only that, but the device, compared to the previous one, has become more complex to manufacture and control, meaning that costs and the bulk of the device have increased.

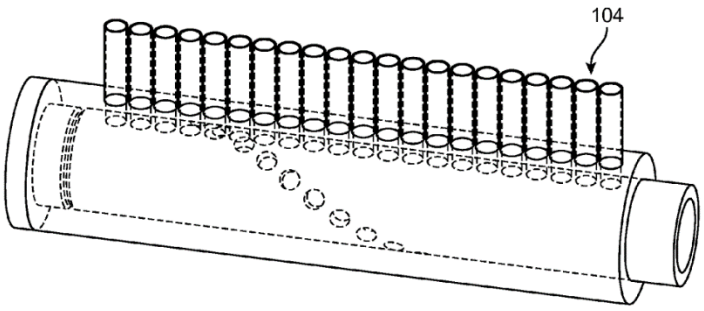

Figure 5.5: Shunt current valve [20]

A flow-resisting device can be designed to function as a shunt current resistor, managed by a flow controller that not only measures but also resists or actively pumps the flow. While flow resistors might share structural similarities with pumps, they differ in the fact that they don't necessarily generate positive pumping pressure from inlet to outlet. Instead, a flow resistor is any electromechanical device that generates back-pressure to counteract fluid flow. Some flow resistors can be adjusted to create variable backpressure, either manually or automatically, allowing for flow measurement and control alongside their shunt resistance capability. With these premises in mind, let’s see how the valve in figure 5.5 works.

Figure 5.5 depicts a unified shunt current valve design featuring a rotating cylinder set, marked as 104. The entry and exit valves are designed to open and close synchronously with the rotation of the cylinder. This rotating valve is specifically designed to direct electrolyte flow to only one cell at any given time. As the cylinder turns, a port on the valve lines up with a corresponding cell, permitting fluid to flow exclusively into that cell. With continued rotation, subsequent cells are sequentially injected with fluid. The speed of the valve's rotation governs the pulse duration, that is, the interval between fluid pulses delivered to a cell. A pump will regulate the system's volumetric flow rate. Alternative mechanical valve configurations can be engineered to achieve synchronous operation, isolating electrolyte flow to individual cells sequentially. All of these steps allow for a discontinuous flow of the electrolyte, called pulsed flow. Flow regulation can be significantly improved by installing multiple valves at the inlet and outlet of each cell. These valves can be controlled electronically or hydraulically to fine-tune the frequency of their opening and closing.

This concept is very interesting, since it offers a good solution with a simple and functional design. It allows for very precise and capillary flow control. Major drawbacks of this design include the pressure drops generated on the channels and the possibility of electrolyte spills

between the rotating cylinder and the stationary component. However, these issues can be easily solved by choosing the right materials and dimensions for the device.

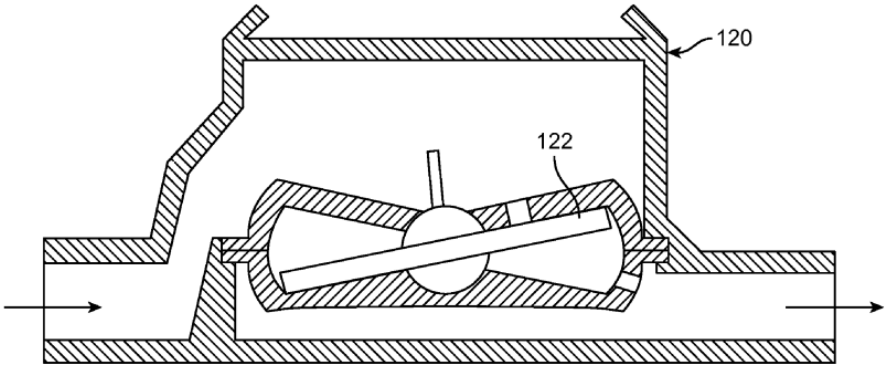

Figure 5.6: Cut-away view of a nutating disk flow meter [20]

Figure 5.6 presents another shunt resistor device example: a nutating disk flow meter, labeled 120. This meter comprises a nutating disk, tagged as 122, a disk set on a sphere that oscillates around an axis due to fluid flow, allowing a set volume of fluid to pass with each rotation. The nutating disk also acts as a physical barrier between the inlet and outlet, serving as a shunt resistor. As a result of the pressure exerted by the flowing electrolyte, the disk lowers, enabling the electrolyte to flow through a small outlet that was previously obstructed. Once the flow of the electrolyte ceases, the disk ascends back to its initial position, completely obstructing the passage and halting the flow of the liquid conductor.

In conclusion, although patent US20120308856A1 by Horne et al. is dated back to 2012 and may not have the most recent solutions to reduce shunt currents, it allows to understand the main principles behind the reduction of shunt currents, that we will find in the next patents. All the devices proposed allow us to understand one core principle: in VRFBs the electrolytes conduct shunt currents, but by modifying the course of the flow, it is possible to reduce the value of such currents.

The patent CN104241665A by Song Yongjiang et al. describes a device that serves as a shunt resistor. Its simplicity lies in its construction: vanes joined at a central hub. The device, marked in red in figure 5.7 and visible in figure 5.8, features these vanes made of non-conductive material, arranged into a wheel that almost equals the tube's cross-section in diameter. The vanes constrict the electrolyte flow path, thus raising the electrical resistance.

During battery operation, the movement of the electrolyte causes the vanes to spin. The device can be easily implemented in the tubing system, without requiring any extra space. The clamping structure, tagged as 2, comprises a mounting seat and a supporting frame. The supporting frame is positioned on the surface of an auxiliary plate, an adjusting structure, marked as 4, connected with the supporting frame is installed in the auxiliary plate, and the adjusting structure 4 is used for adjusting the position of the supporting frame. The clamping frame is installed on the stack, labeled 1. The clamping frame is L-shaped and is connected with the operating stack through a corner.

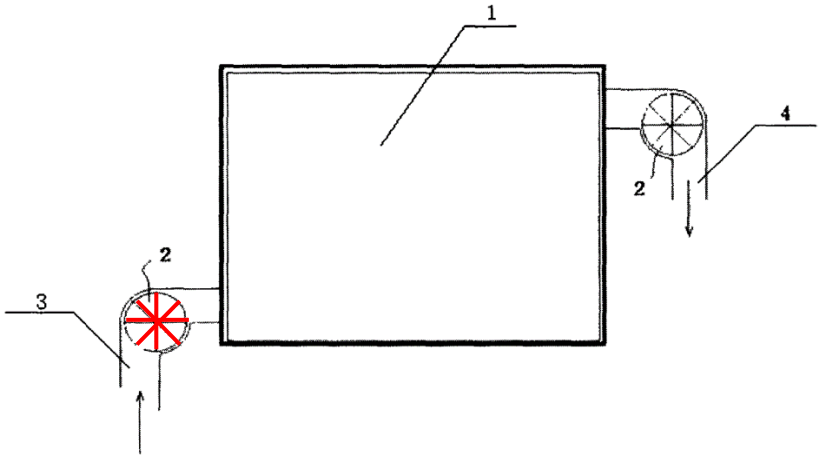

Figure 5.7: Implementation of the rotating vanes device [21]

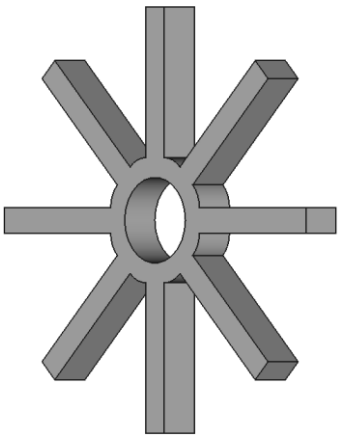

Figure 5.8: 3D model of the rotating vanes device

Other similar shunt resistors to the one just mentioned can be found on patent KR20150143185 by No Tae Geun et al. [22].

Another device that can be implemented to reduce shunt currents is found in patent KR20160075923A by Ha Tae Jeong et al. [23]. More specifically, the shunt resistor in question drastically reduces self-discharge attributed to shunt current. The device is shown in figure 5.9:

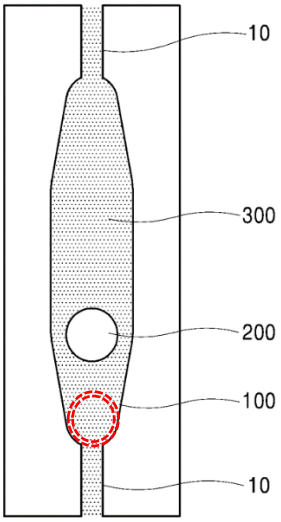

Figure 5.9: Tube section with blocking body, in the red area during stand-by [23]

The device features a tube with an expanded section where the electrolyte flow path width is enlarged. A floating body, labeled 200, is situated within this section and moves vertically in response to the flow velocity of the electrolyte. The ideal width ratio between the standard flow path and the expanded section should be between 1:2 and 1:10. If the width of the expanded flow path is less than twice that of the regular flow path, the floating body may increase flow resistance. On the other hand, if the width exceeds 10 times that of the regular flow path, it becomes difficult to control the flow. The body material is preferably a chemically resistant plastic, such as PP, PE, PVDF, or PTFE, suitable for use with electrolytes. The weight of the body needs to be a specific value in order to be balanced during operation and to avoid an excessive increase in the pumping required. The device can have different designs, as the one presented in figure 5.10:

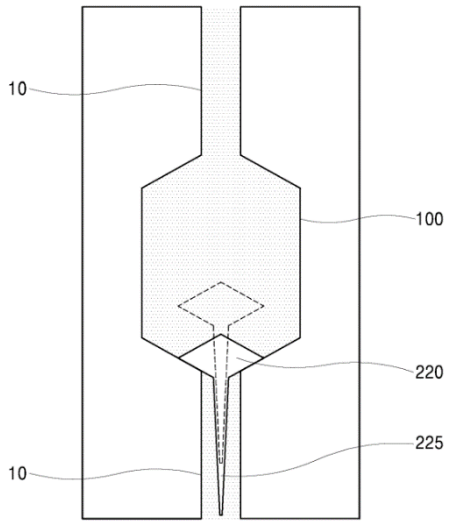

Figure 5.10: Alternative design for the obstructive body [23]

Overall, this device offers a simple solution to reduce standby shunt currents. However, without any constraints on the body, a flow rate variation might cause an unexpected blockage of the tubes.

Patent US10826101B2 by Chang et al. [24] provides a view of an apparatus dedicated to repressing shunt currents. The main goal of this invention is to inhibit shunted currents by obstructing the development of conductive channels for the working electrolytes among unit cells. This is accomplished by isolating the liquid flow streams of each unit cell with gas gaps, thereby reducing the electrical or ionic conduction of the working liquid through these gaps. The working liquid is permitted to cross the gas gap in the form of discrete droplets or bulk drops, which do not simultaneously contact both the upper and lower flow streams, thus allowing the liquid flow to continue without electrical or ionic conduction. This ensures that the working liquid supply reaches each unit cell effectively. The segregating gas gaps are strategically placed between diverging manifolds and subsidiary flow streams prior to the unit cell inlets, as well as between the flow streams post-unit cell outlets and converging manifolds, to guarantee that the liquid flow streams between any pair of unit cells remain distinct.

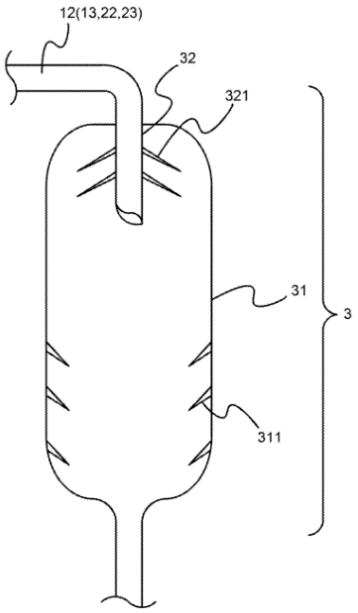

Figure 5.11: A view depicting the first state-of-use of the gas-gap device [24]

Gas-gap devices, marked as 3, shown in figure 5.11, consist of insulating materials and are positioned separately between the first and second branching channels, labeled 12, 13, 22, 23, as well as the inlet diverging manifolds, tagged as 14, 24, and outlet converging manifolds, labeled 15, 25 of the positive and negative electrodes 11, 21. Each branching channel has an inserting tube, labeled 32, designed to fit into the inserted vessels, labeled 31, of the gas-gap devices from above without touching the bottom. The diameters of the inserting tubes are smaller than those of the inserted vessels to prevent droplets from contacting the vessel walls. To enhance the prevention of conductive connections from splashed liquid, each inserting tube, extending from the branching channels, is equipped with multiple fins, tagged as 321 made of insulating material, located at the outer edge where the tube enters the vessel. Similarly, each inserted vessel has several fins, marked as 311, also made of insulating material, on its inner surface. The design of the gas-gap devices allows for different numbers and shapes of inserting tubes and inserted vessels, in order to accommodate different requirements and not limited to standard pipe shapes or diameters. The crucial aspect of these devices is to ensure that droplets from the inserting tubes do not create a conductive path.

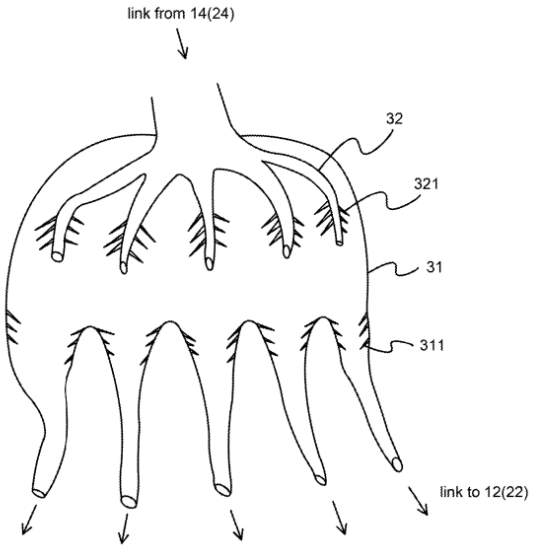

Figure 5.12: A view depicting the second state-of-use of the gas-gap device [24]

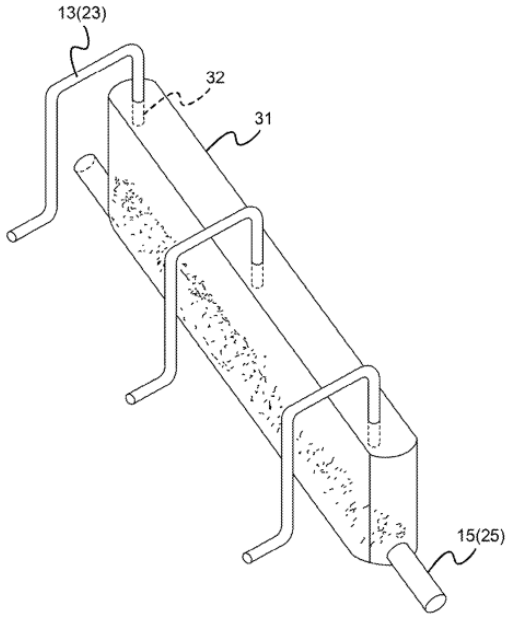

Figure 5.13: A view depicting the third state-of-use of the gas-gap device [24]

As depicted in figure 5.12, a gas-gap device in use features a shared vessel, labeled 31, that accommodates multiple insertion tubes, tagged as 32. This vessel is divided into several drainage chambers, each collecting droplets from the corresponding insertion tube above. This configuration yields results identical to those presented in figure 5.11. The advantage of this design is that it allows the gas-gap device to function as a compact diverging manifold with an integrated gas-gap, thereby reducing the overall size of flow batteries.

Similarly, figure 5.13 illustrates another operational state of gas-gap devices, where a shared vessel serves multiple insertion tubes. However, in this case, the vessel contains a single drainage chamber that collects droplets from all the insertion tubes situated above it.

Although this device is definitely effective in reducing shunt currents by branching the channels at the inlet and outlet, the main drawbacks of such apparatus are the complexity of the design, the mechanical endurance, especially of the fins, and lastly, the cost of such device, losing its cost effectiveness on bigger scale VRFB systems.

5.2 Pump

Until now the devices proposed have been extra component to add in the layout of the battery (figure 5.1), but the pumps can also function as shunt resistors if designed in a specific manner. The author of the patent presents some pump designs, figure 5.14, 5.15 and 5.16 shows some of them:

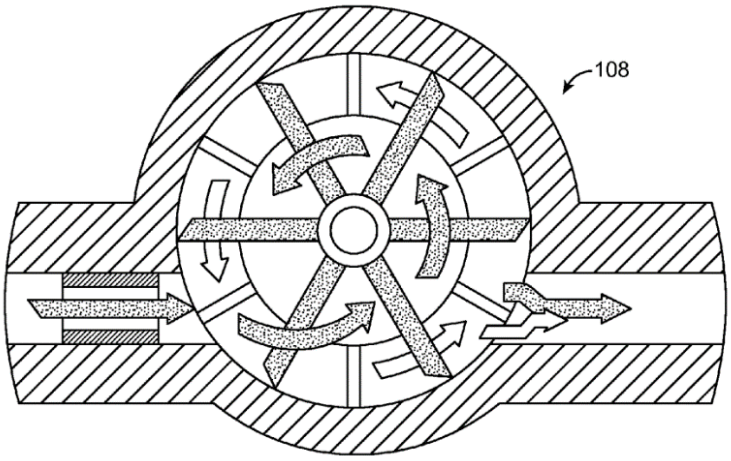

Figure 5.14: Cut-away view of a vane-type pump [20]

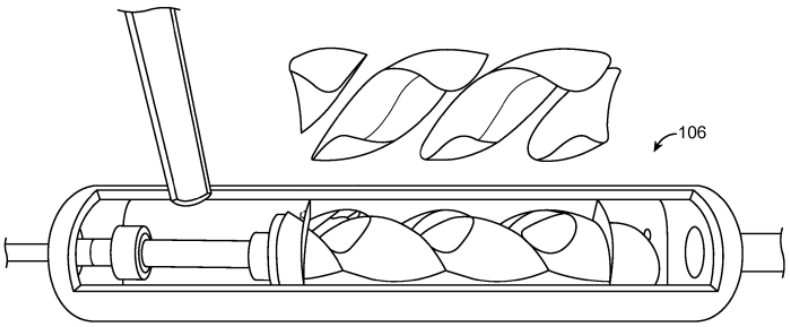

Figure 5.15: Cut-away view of a progressing cavity pump [20]

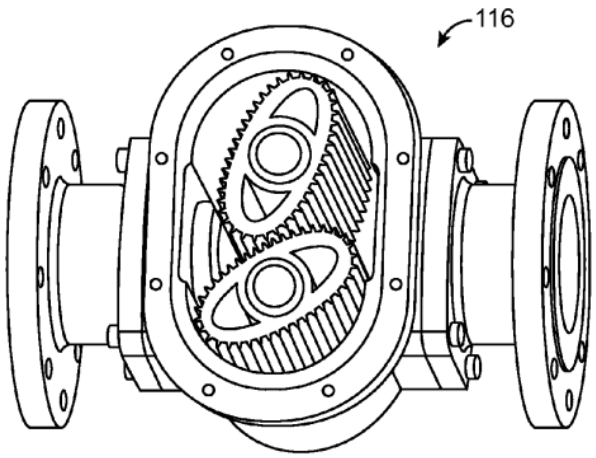

Figure 5.16: Cut-away view of a toothed oval gear pump [20]

The pumps above, due to their construction characteristics, have restrictions that can significantly increase the electrical resistance in the conduits, leading to a reduction (or even a complete elimination) of shunt currents.

Positive displacement pumps, such as pump, labeled 108, depicted in figure 5.14, can be configured to serve as shunt resistors. These pumps possess a shaft that conveys the rotation of a moving element, sealing off a volume within the flow path. As the electrolyte moves through the pump, the shaft rotates accordingly. In order for the pump to operate as a shunt resistor, the fluid volume contained by the pump's element must be sufficiently isolated effectively. This step makes sure that the cross-sectional area of any continuous fluid path across the pump elements, called bypass area, remains minimal. Preferably, the bypass area is small enough to ensure a high electrical resistance, thereby establishing a shunt resistance.

A shunt resistor can also include one or more peristaltic pumps. Figure 5.15 illustrates a progressing cavity pump, labeled 106. A peristaltic pump propels a non-compressible fluid through a flow channel by mechanically squeezing a segment of flexible tubing and moving the compression point along the tubing in the direction of the intended flow. The device includes a rotating helix affixed to a rotor within a tube, operating similarly to an endless screw. Vanes, extending the full width of the tube, partition the electrolyte and form spaces within the fluid. As the helix turns with the flow of the electrolyte, it permits the liquid to move through.

Figure 5.16 illustrates a toothed oval gear pump where two rotating oval gears with interlocking teeth propel or meter a specific volume of fluid with each revolution. Gears similar to those shown in figure 5.16 can also be used in positive displacement flow meters, with gear movement driven by the fluid pressure of the electrolyte passing through the pumps. Additionally, shunt resistor devices, including those with mechanical drives, can be designed to move the electrolyte with minimal resistance, without necessarily pumping or increasing the system's hydraulic pressure. Some positive displacement flow control devices may be designed to impede hydraulic flow by incorporating mechanical, electromechanical, or electromagnetic elements that introduce friction in the flow.

5.3 Pipes outline

Patent US10074859B2 published by Kell et al. [25] presents a shunt current suppression device that has also the functionality of reducing pump losses. As known from equation (4.4) and as seen in the previous patent analysis, a common method to reduce shunt currents is to increase the electrical resistance of the flow paths in the battery tubing system. This can be achieved by incorporating design features like flow restrictors or utilizing pumps that naturally offer more resistance. Although this method is effective at reducing shunt currents, it can also cause greater hydraulic losses. More resistance requires pumps to work harder to maintain the flow rate, which increases their energy consumption. If the extra energy needed to counteract this resistance surpasses the energy conserved by lowering shunt currents, it could detract from the system's overall efficiency. This situation highlights the need for a comprehensive approach to VRFBs design. It must be thoroughly assessed how shunt current reduction methods affect the whole system, considering both electrical and fluid dynamic factors. The objective is to find a balance where shunt currents are reduced without significantly raising pumping losses, and patent US10074859B2 offers such balance.

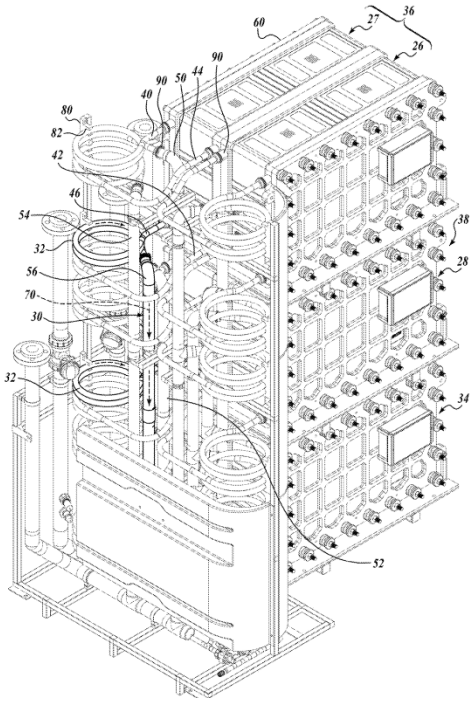

Figure 5.17: Overall system, with a focus on the tube system [25]

As illustrated in figure 5.17, shunt current suppression devices, tagged as 32, not only reduce shunt currents by lengthening the electrolyte flow paths but are also compactly designed. This allows for the use of multiple devices in a confined space to attain the required fluid flow path length without enlarging the housing of the overall system. The looping design of the devices significantly extends the flow path distance between stacks, marked as 36 and 38 through additional turns or increased loop diameters. Choosing the right length and diameter for the shunt current suppression devices strikes a balance between minimizing shunt current efficiency losses and reducing conduit flow losses, thus enhancing system optimization. Figure 5.17 shows that the electrolyte headers, labeled 50, 52, 54, 56, along with the shunt current suppression devices, are positioned to generate a mainly downward fluid flow, which helps in draining the electrolyte during the operation of the system. The shunt current suppression system may incorporate a support frame, labeled 80, which ensures spacing between the flexible tubing loops and sustains the downward flow. As depicted in figure 5.17, the support frame is a vertical structure equipped with multiple notches, labeled 82, to hold and stabilize the loops of the shunt current suppression device. Moreover, the system includes protective covers for the devices, whose inner surfaces feature grooves that provide additional support for the shunt current suppression devices. These devices may have different designs and shapes, as seen in figure 5.18:

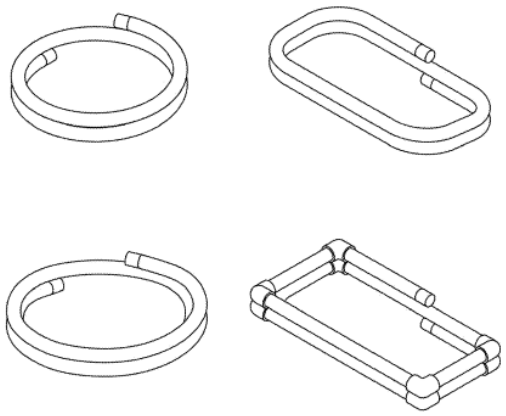

Figure 5.18: Different designs for the tube coils [25]

For each design, there are different pros and cons. The choice may differ depending, for example, on space restrictions in the housing of the system and so on. As seen in a previously analyzed paper [13], bends and junctions in the tubes tend to produce marked pressure drops, increasing pumping losses. So, considering the designs proposed in figure 5.18, the ones on the left have decreased pumping losses compared to the ones on the right. A simulation on SimScale was performed to visualize the pressure inside the tube designs. The considered liquid was water (entry velocity of 0.5 m/s), since, as mentioned in a publication by P.A. Prieto-Díaz et al. [26], the viscosity and density of vanadium electrolytes depend on multiple factors. The results provided by the simulation demonstrate the previous assumptions and are visible in figure 5.19:

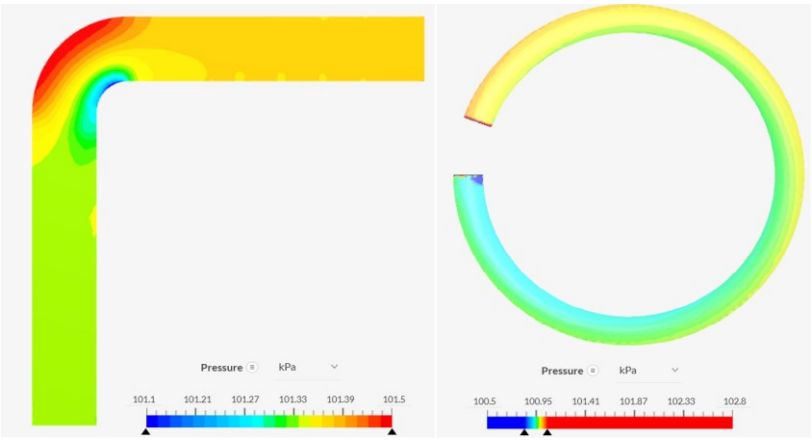

Figure 5.19: Pressure comparison in the different designs

The patent also shows a chart providing the trends of pumping and shunt losses depending on the length and dimensions of the tubes, useful to find a break-even point between pumping losses and shunt current losses.

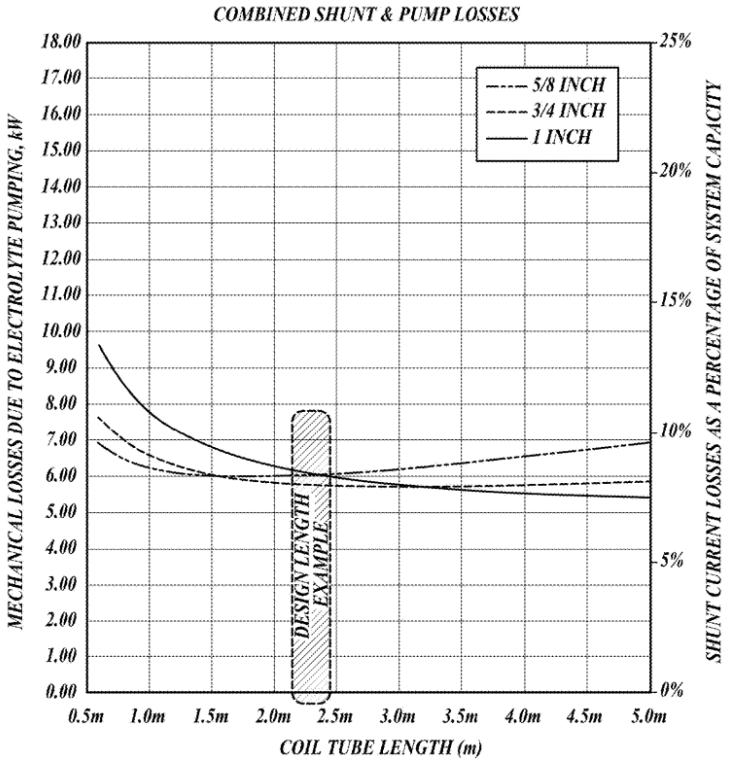

Figure 5.20: Trend of mechanical and shunt current losses [25]

The data in figure 5.20 depicts the theoretical application of the exemplary system, shown in figure 5.17, where the loops, when viewed from above, are essentially circular, and their overall shape is helical. In this particular model, the loop diameter, electrolyte flow rate, and physical properties of the electrolyte like viscosity and conductivity remain constant, while the circular cross-section and the length (as measured by the number of loops) can be altered. There are multiple methods for calculating the mechanical pumping losses and shunt current losses related to the loops.

Overall, this patent offers a great solution to mitigate shunt currents, a simple and cost-effective device that also takes into account mechanical losses. However, shunt currents passing through the tubing system with a coil-like shape might generate unwanted magnetic field, in agreement with the Curl right-hand rule.

Patent CN109155422B by Qianzhao Jiantai et al. [27] also offers a view of the tubes directing the electrolyte flow manufacturing and shaping to reduce shunt currents. The two layouts proposed are found in figure 5.21 and 5.22:

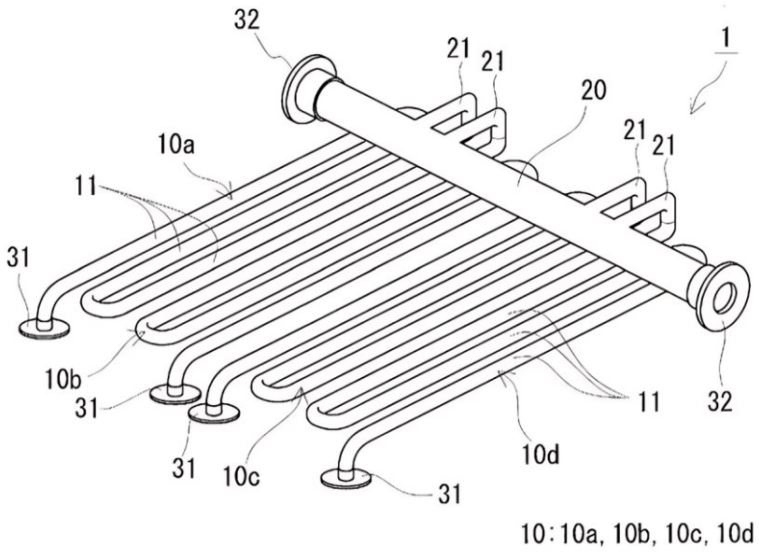

Figure 5.21: First tubing system design [27]

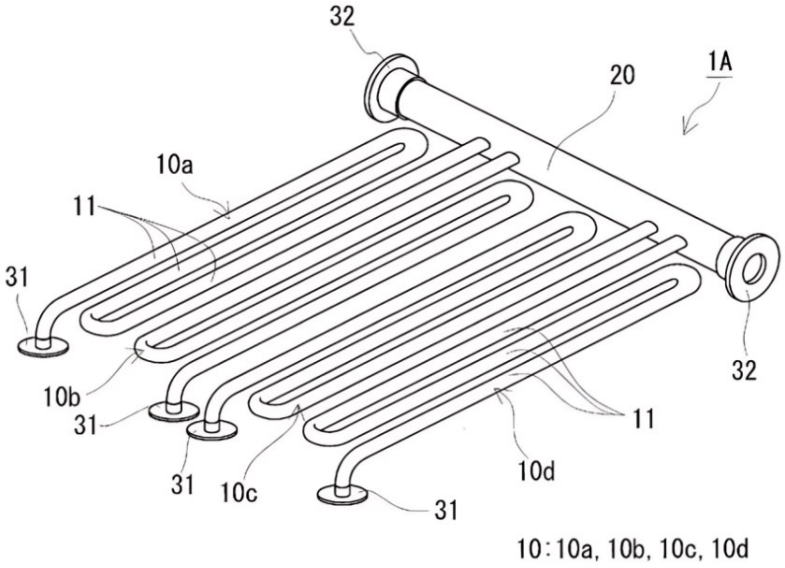

Figure 5.22: Second tubing system design [27]

Typically, a high-capacity redox flow battery comprises multiple battery elements (a battery cell stack) and is designed so that a tube, which allows the electrolyte to flow, branches out between a case and each battery element. This design facilitates the transport of the electrolyte from a single case to the multiple battery elements. In this configuration, a tube, also known as a "tube unit," forms the electrolyte flow path within the RF battery. This tube unit consists of a main trunk pipe connected to the case and several branch pipes that extend from the trunk pipe to the individual battery elements. The tube, being in direct contact with the electrolyte, is made of a resin that is inert to the electrolyte, commonly polyvinyl chloride resin (PVC). When this pipe system, comprising the main and branch pipes, is utilized as the electrolyte flow path in an RF battery, the electrolyte shared among the battery elements flows from the main pipe through the branch pipes. Consequently, the adjacent battery elements become electrically connected via the electrolyte. In a redox flow battery, manufacturing variations among the battery elements can lead to potential differences between adjacent elements. This potential difference causes a shunt current to flow through the electrolyte in the tubes (both main and branch), resulting in losses such as heat generation from the electrolyte. To mitigate this, increasing the resistance of the electrolyte within the pipes is beneficial. This can be achieved by reducing the cross-sectional area (diameter) of the branch pipes connected to the battery elements and by extending the total length of the branch pipes. Often, to minimize the installation space for tubes in redox flow batteries, a meandering (S-shaped) tube, also known as a "shunt limiting tube," has been employed. This design features a series of linear and curved sections alternately connected to compact the overall structure. The "zigzag" configuration includes at least one zigzag segment, comprising three parallel linear sections and two curved sections that connect adjacent parallel lines. At both ends of a zigzag tube, a curved section joins two straight sections, with the end of the third straight section positioned parallel to the others. In traditional branch piping, bends are created using joints between pipes or by bending the pipes themselves. Joints can increase the risk of liquid leakage due to potential assembly defects or flaws at the connection points. Additionally, using joints can be time-consuming in the manufacturing process. Bending, on the other hand, eliminates the need for joints, thereby reducing leakage risks. However, manual bending can be challenging to perform with high precision, often leading to increased costs. The growing demand for smaller redox flow batteries has led to a need for more compact tubing designs. To achieve a compact form, the straight sections of the branch tube must be brought closer together, minimizing the distance between the centers of adjacent straight sections. However, industrial limitations exist in reducing this distance by bending, as it involves decreasing the curvature radius of the bend. Consequently, manufacturing a zigzag branching pipe with a small center-to-center distance

relative to the pipe's outer diameter is challenging. When the center-to-center distance is reduced, the bent section that connects two straight sections and the end of the remaining straight section are in close proximity. This proximity can cause technical issues during the bending process, such as complications with the processing jig setup and unintended heating of the unbent straight section. Historically, to overcome this, zigzag branch pipes with small center-to-center distances have been created by connecting two J-shaped tubes with a joint to form an S-shape. This method, however, makes it difficult to simultaneously reduce liquid leakage risk and achieve a compact pipe design. The objective of this patent is to present a redox flow battery tube, and a tube unit designed to minimize the risk of liquid leakage and to be compact. Another goal is to describe a manufacturing method for a redox flow battery tube that can produce a zigzag tube with numerous parallel and bent portions, integrated in an alternating pattern with high precision. Additionally, it aims to provide a redox flow battery where the tube's risk of liquid leakage is low and requires less installation space. The manufacturing method enables the stable industrial production of a meandering tube with integrated parallel and bent portions, connected alternately with great accuracy. The redox flow battery itself offers a low risk of liquid leakage and a reduced need for installation space. The inventors have discovered that by using rotational molding to produce a redox flow battery tube, a zigzag tube with alternating parallel and bent portions can be integrally molded. Rotational molding allows for a smaller curvature radius in the bends, enabling a closer center-to-center distance between adjacent parallel portions relative to the tube's outer diameter. The redox flow battery tubing system features a bent portion, with numerous parallel and bent portions alternately connected in an integral formation. This design allows for an extended tube length, minimizing loss from shunt current. The seamless construction of the tube, without any joints or bonded connections, significantly reduces the risk of liquid leakage, thereby enhancing the battery's reliability. The parallel section could be a curved segment designed with a curved profile or a wavy line segment with a wavy shape, besides the linear segment which has a straight profile. A straight parallel section allows for a more compact tube design. Conversely, when the parallel section is curved or wavy, the tube's overall length can be increased compared to a straight section, which helps to further minimize shunt current loss. When the lateral pipe, labeled 10, possesses an outer diameter of 30 mm or greater, it ensures a sufficient flow path area for the electrolyte solution. If the outer diameter is 50 mm or smaller, it allows for a more compact design of the lateral pipe. Additionally, with an outer diameter of 50 mm or less, it is simpler to mitigate shunt current loss that occurs with an increased flow path area. Ideally, the outer diameter should be 40 mm or less. The parallel sections, labeled 11, of the branch pipes each have a length that is, for instance, no less than

900 mm and no more than 1500 mm. When the length of the parallel section is at least 900 mm, the overall length of the branch pipe is increased, which effectively reduces shunt current loss. Conversely, when the length of the parallel section does not exceed 1500 mm, the size of the branch pipe in the direction of the parallel section is minimized.

This patent offers a good design that can be implemented in any configuration, to increase the length of the tubes, in order to increase the resistance met by shunt currents. However, as visible in figures 5.21 and 5.22, it presents a significant number of narrow bends, which may cause increased pumping losses.

5.4 Bipolar plate, flow frame and cell frame design

Bipolar plates, flow frames and cell frames are crucial components of VRFBs since the electrolyte flows through channels and manifolds and interacts with these components. Therefore, it is important to evaluate the design of such components, to reduce shunt currents.

Patent GB2085475A by Balko and Moulthrop [28] propose a specific design of the channels that interconnect the bipolar plates of the different cells. The hollow is designed to reduce shunt currents.

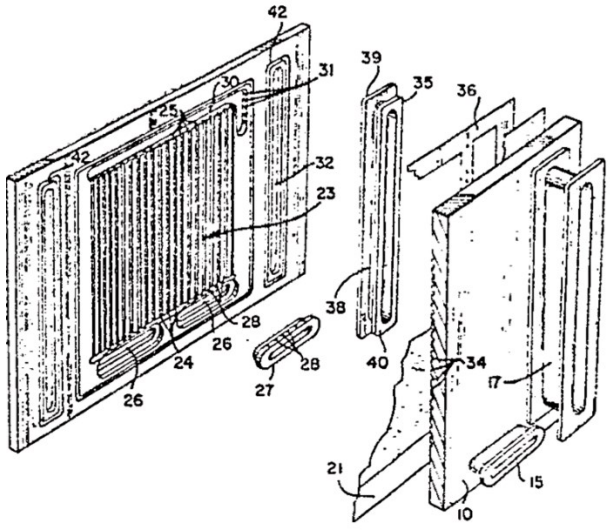

Figure 5.23: General overview of the bipolar plates and the connections between them [28]

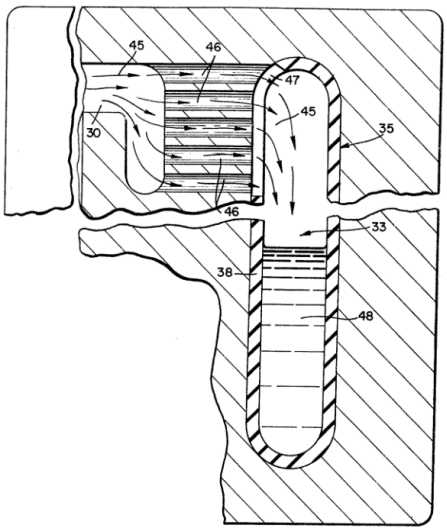

Figure 5.24: Design of the channels interconnecting bipolar plates [28]

Shunt currents, which flow between the electrodes of adjacent cells through the conductive fluid and the fluid pool in a bipolar cell assembly's manifold, are reduced by introducing the conductive fluid at the top of an elongated outlet manifold, tagged as 33. This creates a cascading flow that disrupts the current path. Insulating the manifold walls with insulating, elastomeric sealing grommets, labeled 35, minimizes shunt currents across the fluid manifold and all conductive bipolar elements in the series-connected electrochemical cell assemblies. This insulation prevents current flow between the manifold walls through the conductive fluid and provides an edge seal between bipolar plates. The present invention pertains to a process and apparatus for electrochemical cell assemblies, specifically for reducing shunt current in series-connected bipolar assemblies. Figure 5.24 demonstrates how shunt currents, potentially flowing between the conductive electrodes of adjacent cells through the moving fluid and the conductive fluid pool at the bottom outlet manifold, are minimized. This aspect of the invention is explained in relation to the anolyte outlet manifold of an electrolyzer but is equally applicable to the catholyte outlet manifold of any electrochemical cell assembly that uses conductive fluids and bipolar elements. In this process, the depleted conductive anolyte fluid, and the fluid stream from the anode chamber of each cell, enter the collection channel, labeled 30, pass through passages, marked as 46, in the bipolar plates, and openings, tagged as 47, in grommet, to the top of the anolyte outlet manifold. The fluid stream then cascades from the top of the manifold into the fluid pool, labeled 48, at the bottom. By directing the conductive fluid to fall vertically from the top of the manifold into the pool, the conductive current path is interrupted, thereby increasing the resistance.

The fluid stream through passages can be analyzed with a representation of its electrical resistance. Let's consider the following values: electrical conductivity of vanadium $\sigma = 5 * 10^4$ S/cm, the length of the pathway l = 3 cm and the cross section of the pathway A = 2 cm^2 we utilize equation (4.4), $R = l / A\,\sigma$. As the first case we consider a bipolar plate, without the passage 46 not separated in five different pathways. In that case the resistance of the uniform fluid stream is simply equal to a single resistance calculated with the values provided before, so R = 30 μΩ. Now let's consider the case of figure 5.24 assuming that the overall cross section stays equal, in order to avoid increased pressure. In the passage there are five pathways, each with a cross section equal to A / 5. At the openings the cascades have a fluid stream still separated for a portion of the fall, for example 1 cm. This means that the resistance of the passage will have a higher value of l for each pathway of l^* = 4 cm.

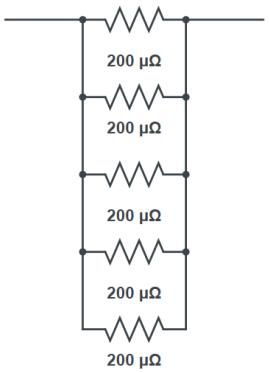

Figure 5.25: Electrical resistance of the passage in figure 5.24

The equivalent resistance is R_{eq} = 40 μΩ, higher than the previous one. In reality this difference is higher since the cross-sectional area is also reduced.

So, by separating the passage in different pathways not only the cross section is reduced but also the length of the pathway is artificially increased, increasing the resistance of the electrolyte, reducing the value of shunt currents.

Patent US10381667B2 by Thomsen et al. [29] describes a specific design of flow frames and bipolar plates developed to increase the overall efficiency of the stack, dependent on shunt currents as well.

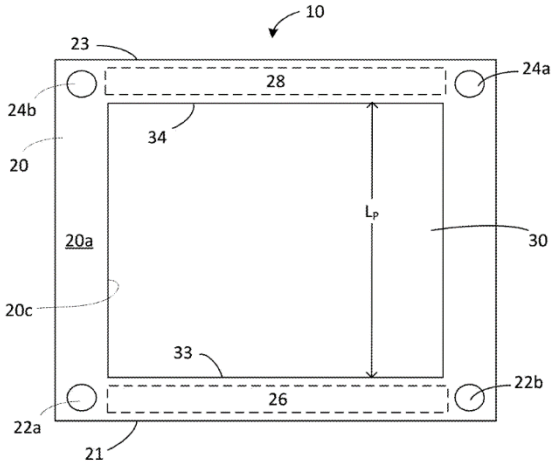

Figure 5.26: Top view of the stack flow frames [29]

As depicted in figure 5.26, the support frame includes a first side, labeled 21, an opposing side, labeled 23, a facing surface, labeled 20a, and an opposing surface. The inner edge of the support frame 20 delineates an opening sized to accommodate the bipolar plate, labeled 30, with the inner edge making contact with the bipolar plate. Subsequent figures provide details of the bipolar plate. The bipolar plate can be adhesively attached to the support frame, or a gasket (not shown) might be employed to seal the edges of the bipolar plate to the support frame. Additionally, the support frame includes inlet ports, marked as 22a, 22b on the first side and outlet ports, tagged as 24a, 24b on the opposing side. An inlet manifold and an outlet manifold, labeled 26 and 28 respectively are integrated into the lower surface of the support frame 20, as further described below. The support frame can be made from any appropriate insulative material. For instance, one version of the support frame is made of polyvinylchloride, while another is made of glass fiber reinforced vinyl ester, which is suitable for compression and/or injection molding.

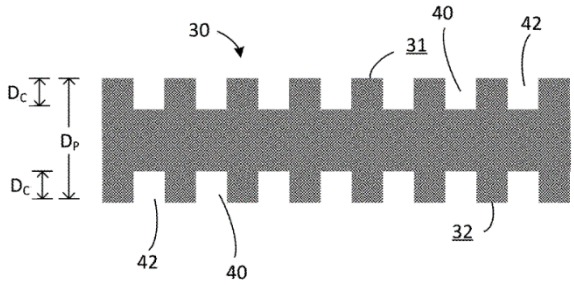

Figure 5.27: Cross-sectional view of a monolithic bipolar plate [29]

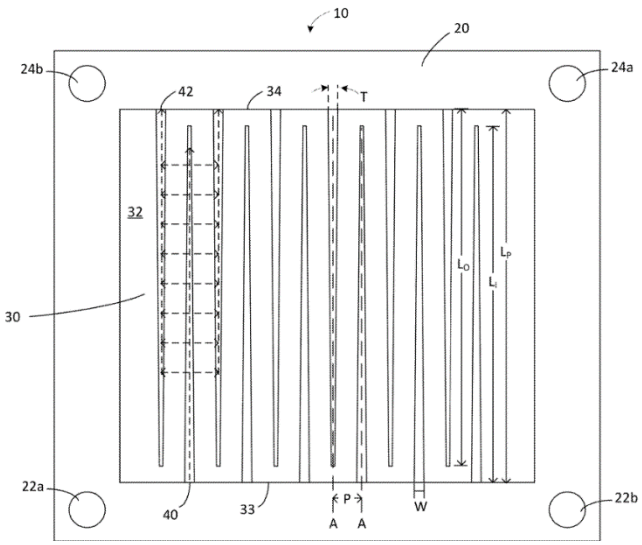

Figure 5.28: Top view of the flow frame in figure 5.26 with channels [29]

Referring to figures 5.27 and 5.28, the quadrilateral, monolithic bipolar plate features a first surface, labeled 31, an opposing surface, a first side edge, tagged as 33, an opposing side edge, and a length L_p between the first and opposing side edges. The bipolar plate advantageously possesses a surface area (length x width) that is greater than or equal to the size (length x width) of an adjacent electrode. A series of parallel flow channels, which include alternating inlet flow channels and outlet flow channels, labeled 40 and 42 respectively, are formed on the first surface. In certain designs, a similar series of parallel flow channels are also present on the opposing surface of the bipolar plate. These flow channels can be created using any appropriate method, such as machining or pressing into the bipolar plate. The bipolar plate can be made from any suitable electrically conductive material, including but not limited to metals, pure graphite, and graphite powders combined with resins like graphite-loaded phenolic, epoxy, polyester, and vinyl ester resins. All these materials al chosen also with the objective of reducing shunt currents. As illustrated in figure 5.27, each flow channel, has a depth D_c that is less than half of D_p, where D_p represents the depth of the bipolar plate, measured from the first surface to the opposing surface. In certain designs, the bipolar plate has a depth D_p ranging from 3 mm to 9 mm, typically between 4 mm and 6 mm, while each flow channel, has a depth D_c ranging from 1 mm to 3 mm, often between 1 mm and 2 mm. Detailed in figure 5.28, the inlet flow channels originate from the first side edge of the bipolar plate and have a length L that is shorter than the distance L_p between the first side edge and the opposing side edge, resulting in a closed distal end. Similarly, the outlet flow channels start from the opposing side edge and also have a length L_o that is shorter than L_p, providing a closed distal end. The inlet

and outlet manifolds are omitted in figure 5.28 for clarity. Each inlet and outlet flow channel aligns with a central lengthwise axis A. Some models feature each inlet and outlet flow channel with an opening width W ranging from 1 mm to 15 mm, and a taper T along axis A within 0 to 5 degrees. The narrow design of flow channels reduces ohmic loss caused by extended current paths, which can lead to a significant pressure gradient along their length. The tapered design of flow channels addresses this issue by maintaining a consistent pressure gradient along the channel at higher flow rates, thus enhancing velocity uniformity and allowing for higher flow rates. The pitch P, the spacing between each inlet or outlet flow channel and the adjacent channel, is set between 2 to 8 times the opening width W of the channel. Pitch P is defined as the distance between the central lengthwise axis A of one channel and the central axis A of the adjacent channel. Figure 5.29 (below) details the construction of an inlet manifold integrated into the lower surface of the support frame's first side. This manifold consists of several fluid inlet distribution channels, labeled 27, arranged in a serpentine pattern. Each channel begins at the inlet port and runs parallel to the first side's outer edge for a certain distance before diverging. The channel's outlet is designed to align and communicate with a single inlet flow channel on the bipolar plate. This design is distinct from other inlet manifolds, which typically have one fluid inlet distribution channel serving multiple inlet flow channels on the bipolar plate. In a stack configuration, alternating redox flow battery stack flow frames are positioned so that the inlet manifold is adjacent to an electrode that contacts the bipolar plate.

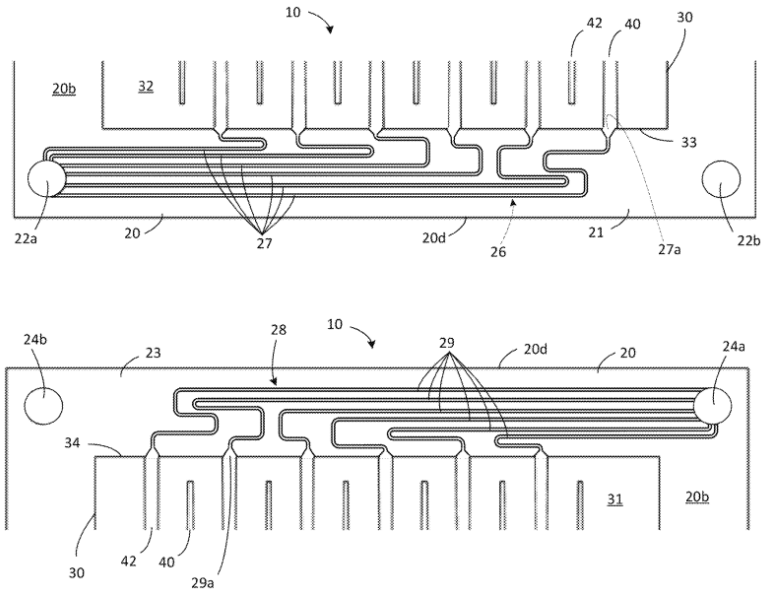

Figure 5.29: Detailed view of the inlet and outlet manifolds [29]

Some of the common issues in redox flow battery stacks include shunt currents in the cells and between cells, as well as pressure drops across the manifold and the bipolar plate. So, when it comes to managing shunt currents, it can be achieved by using long, narrow cross-section flow channels. Such measures increase electrical resistance and reduce shunt currents. However, these channels also cause a pressure drop, leading to higher pumping requirements and system fluid pressures. The need for low electrolyte pumping loss (e.g., larger cross-section channels with short lengths) conflicts with the need for low shunt currents (e.g., narrow cross-section channels with long lengths). The proposed inlet and outlet manifolds resolve these demands by balancing shunt current and pressure drop to optimize the overall stack efficiency, by finding a break-even point. Also, the parallel flow channels in the bipolar plates help reduce pressure drop compared to plates without such channels, where electrolyte flows over the plate's surface. In certain designs, each fluid inlet distribution channel may have a semicircular, semi-oval, V-shaped, rectangular, or other polygonal cross-section. Generally, a circular or nearly circular cross-section offers lower resistance than a cross-section with a large aspect ratio. However, pumping losses can be somewhat reduced by altering the cross-sectional shape while maintaining the same area, thus preserving the shunt current. Shunt power loss is roughly linear to both the channel length and area. This suggests that while the required pumping power is proportional to the channel length-to-area ratio, the shunt power loss is proportional to the channel area-to-length ratio. For minimal pumping losses, some embodiments feature fluid inlet distribution channels with a square cross-section. The cross-sectional area and length of each channel are tailored to achieve a specific manifold electrical resistance and shunt current profile. The manifolds design embodiments depicted in figure 5.29 result in a reduced shunt current and/or a decreased pressure drop compared to a manifold design that features a single fluid inlet distribution channel for distributing electrolyte to all inlet flow channels, or a single outlet collection channel for gathering electrolyte from all outlet flow channels. This enhancement leads to improved efficiency of the redox flow battery stack flow frames. In certain embodiments, the shunt loss (ratio of shunt current to load current) is limited to no more than 1-2% for a stack comprising 1-40 stack cells.

The last two studied patents offer a key consideration: the methods used to reduce shunt currents in bipolar plates and flow frames are the same as the ones used for the tubing system.

Patent US20170229715A1 by Chou et al. [30] describes the fabrication processes and designs of bipolar plates that minimize leakages and shunt currents. To reduce shunt currents, branch channels are created in the frame via injection molding. The use of the resulting bipolar plate not only lowers the risk of electrolyte leakage but also decreases the number of components

and the assembly processing time. This effectively reduces the costs of processing and assembly. Thus, the invention streamlines the bipolar plate's structure while also cutting costs.

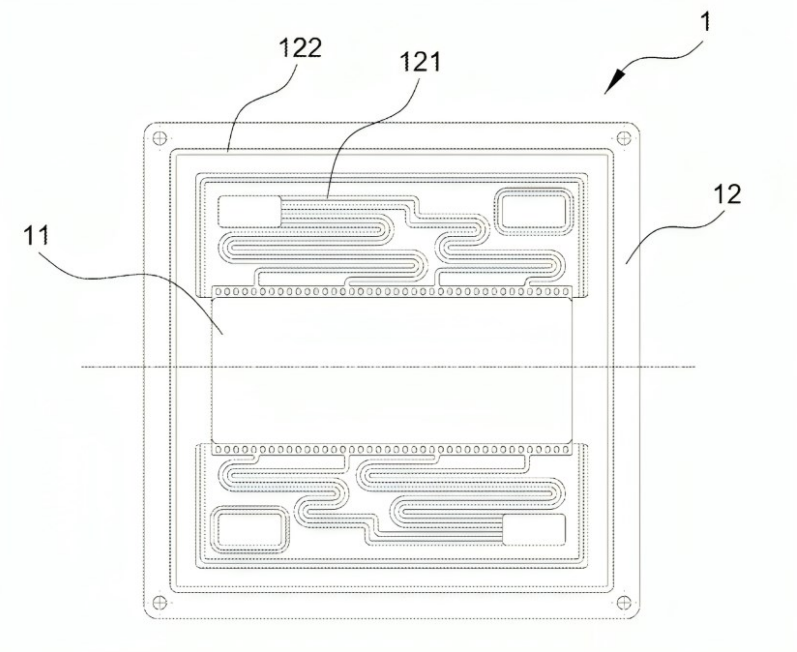

Figure 5.30: Structural view of the integrated bipolar plate [30]

The current invention creates an integrated bipolar plate by injection-molding an acid-resistant insulating material around a graphite plate rather than encasing the graphite plate with two insulating frames. Composite grooves on the frame surrounding the graphite plate enhance the bond between the insulating material and the graphite plate, minimizing the risk of electrolyte leakage. Additionally, branch channels are incorporated into the frame to reduce shunt currents. The adoption of an integrated bipolar plate in a cell stack not only diminishes the risk of electrolyte leakage but also decreases the quantity of components and the time required for assembly, thereby significantly cutting down on processing and assembly costs. Compared to conventional bipolar plate designs, the integrated bipolar plate is more efficient and necessitates significantly fewer components. This innovation streamlines the architecture and reduces costs, providing a benefit for all-vanadium redox flow batteries in energy storage applications. As described in figure 5.30, this invention incorporates two initial leak-proof grooves outside the reaction area of frame, labeled 12 and graphite plate, labeled 11. This design enhances the connection between the graphite plate and the acid-resistant insulating material, thereby preventing electrolyte flow on both sides of the integrated bipolar plate. This invention features two initial leak-proof grooves that surround the graphite plates, which assist in securing the injection molding jig. The upper positioning block is crafted to match the first

leak-proof groove on the inner edge of the graphite plate's top surface and is held in place by the lower mold. In a similar fashion, the lower positioning block fits into the first leak-proof groove on the inner edge of the graphite plate's bottom surface and is held by the upper mold. As a result, the upper and lower molds encapsulate the graphite plate, guaranteeing its stable positioning. Moreover, the invention employs cover plates over the branch channels, tagged as 121, to prevent electrolytes within these channels from coming into direct contact with a proton exchange membrane. This design choice preserves the lifespan of the membrane and prevents it from falling into the branch channels, which could obstruct the electrolytes. Additionally, a second leak-proof groove is established on the contact surface between the cover plate and frame to avert electrolyte leakage from the cover plate.

The next patents regarding the different cell frames designs will be briefly described, to avoid redundancies of the concepts already mentioned above. For example, patent KR101742980B1 by Jo Beom Hui et al. [31] propose different designs for cell frames, all of them visible in figure 5.31:

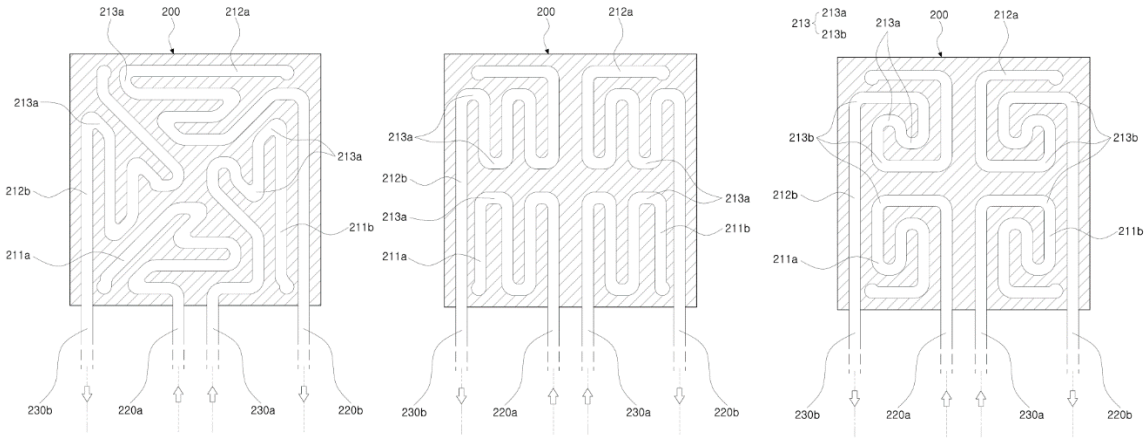

Figure 5.31: Three different cell frame designs [31]

All of the proposed designs, as in previous patents, maximize the use of the surface available on cell frames to lengthen the flow path, increasing shunt current resistance.

Other patents [32],[33],[34] offer others simple, yet functional flow frames concepts, with different flow paths, 3D models of such designs are observable in figure 5.32:

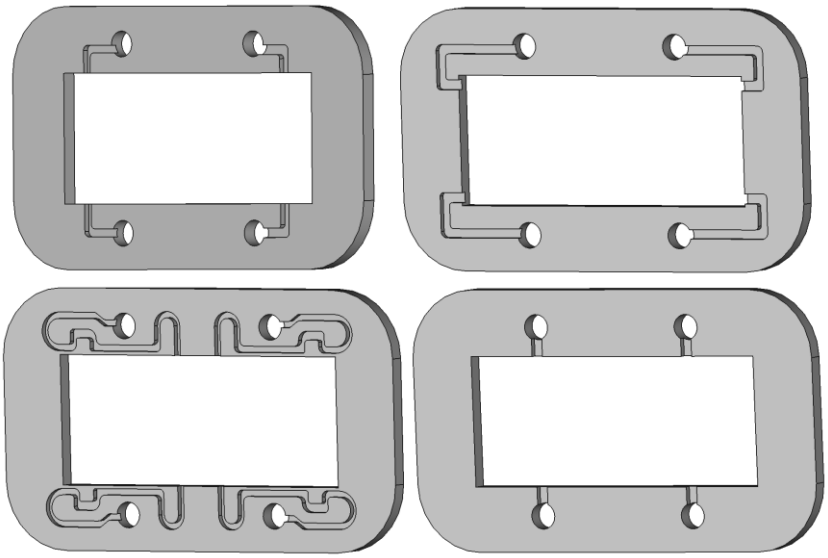

Figure 5.32: 3D models of different flow channel designs

In general, like in figure 5.32, the designs with longer channels, have more bends, increasing pressure drops. A good compromise can be, for example, the design on the top right in figure 5.32. Each design of bipolar plate, flow frame and cell frame should be individually studied by experimental measurements in order to evaluate their influence on the round-trip efficiency.

5.5 Tank design

The positive and negative electrolytes tanks can contribute to the depletion of shunt current, if integrated with some specific devices. A crucial role is played by the inlet of the tanks, which allows to disrupt the electrolyte flow, for example, by simply implementing a shower head, as shown in figure 5.33:

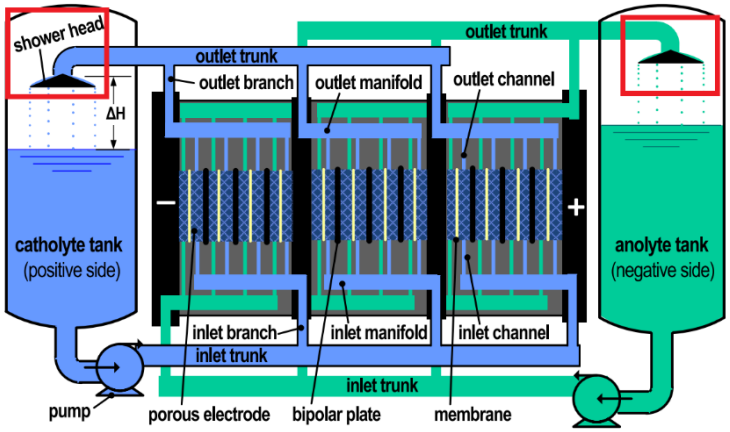

Figure 5.33: VRFB with implemented shower heads, highlighted in red [19]

This device allows to divide the main flow into many smaller ones, disrupting the flow, increasing shunt current resistance. Patent CN201383523Y by Cheng Jie et al. [35] offers different concepts from the classic shower head, the designs are proposed in figure 5.34:

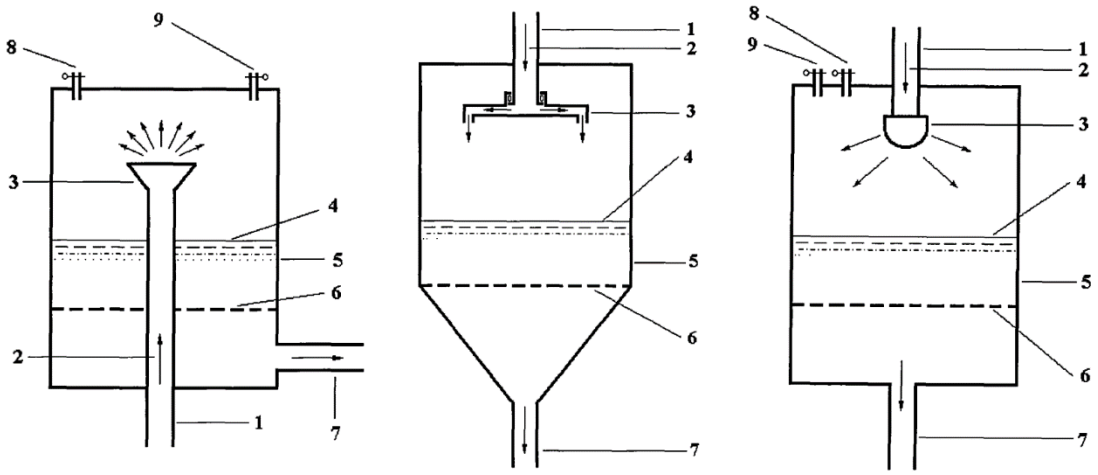

Figure 5.34: Different shower head concepts [35]

Shower heads are easy to implement in already existing configurations, especially in industrial scale applications, where tanks have considerable dimensions and the tanks are not fully filled with electrolyte. Depending on the design, different values of pressure drop might be present in the shower heads.

Another patent, KR102161420B1 by Seong Mun Ja et al. [36] suggests a different approach to the issue. The author proposes to add a grid on top of the tank, as shown in figure 5.35:

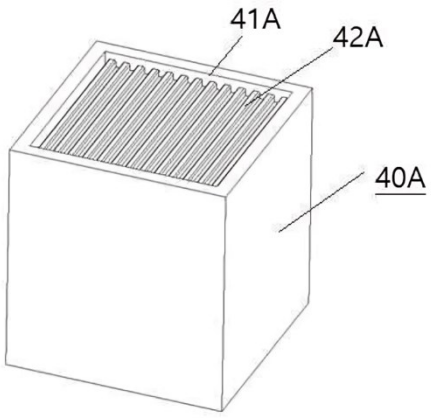

Figure 5.35: Tank with integrated grid [36]

Although the grid is not fully utilized and the flow is not separated effectively, the main advantage of this solution is the complete absence of any significant pressure drops, keeping pumping losses unchanged.

5.6 System configuration and layout

In VRFB, the system's configuration and layout, especially the interconnections among various stacks, are critical in reducing shunt currents. Effective system design necessitates the optimization of electrical connections, flow paths, and component arrangements to manage these currents. Minimizing the effect of shunt currents is achievable through careful arrangement of the layout and configuration.

Patent WO2014145788A1 by Sha and Lin [37] studies different configurations in order to minimize shunt currents. The authors highlight how voltage difference between different cells or stacks may increase and favor the presence of shunt currents in the manifolds.

Two are the configurations proposed, in figures 5.36 and 5.37:

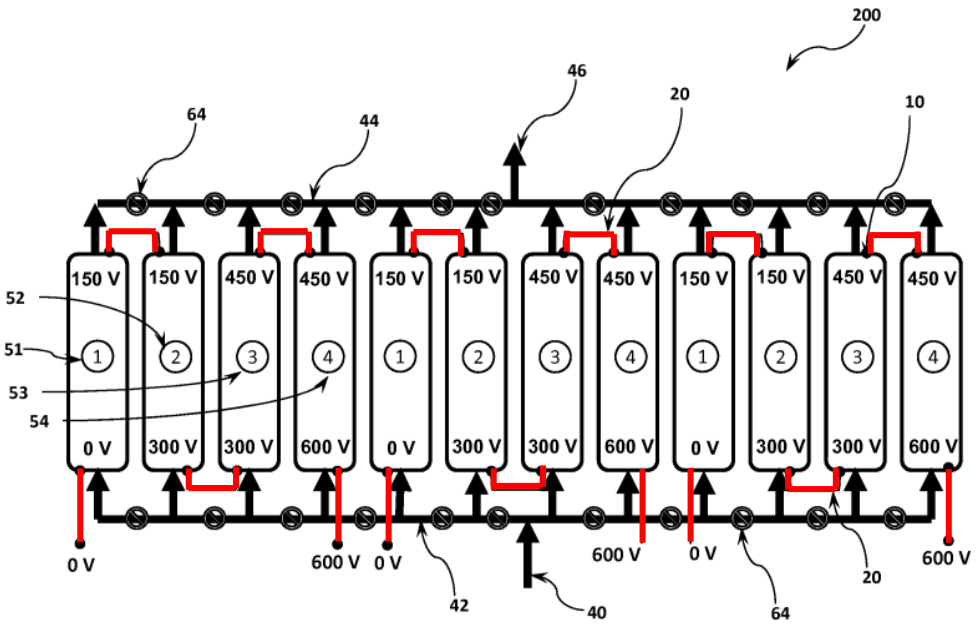

Figure 5.36: Stack assembly having multi-block strings [37]

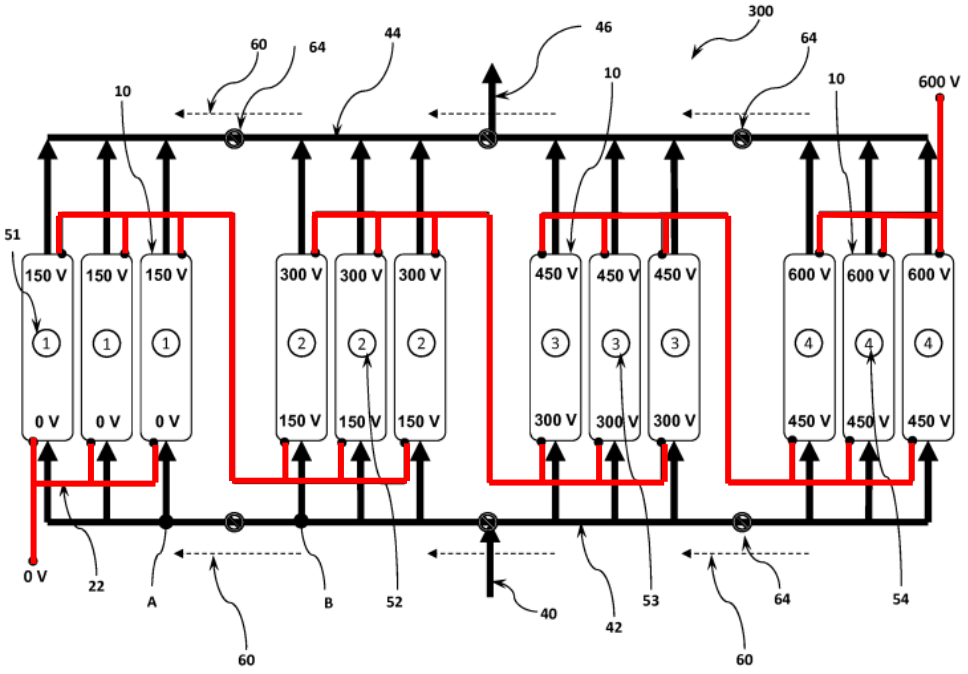

Figure 5.37: Stack assembly having multi-block strings with strings physically separated [37]

Figure 5.36 presents embodiments of a multi-block flow battery stack assembly, labeled 200, comprising three strings. For instance, the first string could include the blocks situated between electrical terminals labeled 22 and 24, the second string could encompass the blocks between terminals marked as 26 and 28, and the third string could consist of the blocks between terminals tagged as 32 and 34. Each "string" might be composed of several blocks, identified as 10, linked together in an electrical series. The blocks can be arranged in fluidic parallel, allowing a fluid electrolyte to flow through an inlet, distributed by an inlet manifold, into the blocks. As depicted in figure 5.36, the electrolyte can be directed simultaneously from a common conduit or manifold into multiple blocks, which may belong to different strings. Once the electrolyte has passed through the blocks, it can be channeled into a common outlet via an outlet manifold. The inlet manifold and the outlet manifold can be configured using any suitable combination of structures, such as various lengths of pipes with branch connectors, or a unitary or multi-component manifold assembly. The stack assembly can incorporate blocks designed to function across varying electric potentials. For instance, blocks of “type 1” are intended to work between 0V and 150V, while blocks of “type 2” operate from 150V to 300V. Similarly, blocks of “type 3” function from 300V to 450V, and blocks of “type 4” from 450V to 600V. Typically, a string will include at least one block designed for each voltage range. Therefore, a string might contain one or more blocks of each type. In certain designs, the three strings of figure 5.36 can be electrically interconnected in parallel to enhance the power

capacity of the entire stack assembly. While figure 5.36 depicts three strings, each with four blocks, a flow battery stack assembly utilizing the principles described can be configured into any number of strings with any number of blocks. These specifics can be tailored according to the needs of a specific application. Likewise, although the blocks in the illustration are marked with a 150V potential difference, alternative cell blocks can be designed with varying electrical characteristics to suit different applications. For instance, if each unit is designed to handle a potential difference of 150V and the units are connected in series to yield 600V, significant shunt currents could arise due to the substantial voltage disparities between electrolytes in a shared manifold. Shunt currents of various magnitudes may also flow through different sections of the electrolyte conduit, linking units with disparate potentials. The size of a shunt current between any two points in an electrolyte conduit is proportional to the voltage difference across those points, and the electrical resistance of the conduit, as governed by Ohm's law, depend on the composition of the electrolyte since conduits are generally made from electrically non-conductive materials. In this configuration, shunt current resistors, like mechanical shunt current resistors (like the ones seen in previous patents), numbered 64, can be placed in electrolyte flow lines situated between blocks, which may have significant potential differences.

Figure 5.37 depicts various configurations of a stack assembly, numbered 300, where strings can be separated, and blocks, always labeled 10, are organized according to voltage levels. In certain scenarios, blocks that operate at similar voltages might be grouped together, either physically or in another manner, to minimize shunt currents. For instance, “type 1” blocks and designed for operation between 0 to 150 volts, could be clustered together. Concurrently, “type 2” blocks and intended to work from 150V to 300V, could be organized into a second group next to the first. In a similar fashion, “type 3” blocks could form a third group, and “type 4” blocks a fourth group. Consequently, the only shunt currents present in the shared electrolyte conduits would be those among block groups of the same type. Given the voltage values provided as examples, the maximum voltage difference between any two points (for instance, points A and B) within a shared electrolyte conduit would be limited to 150V. Therefore, organizing blocks by shared voltage levels can significantly diminish shunt currents within the shared electrolyte conduits. Shunt currents between block groups can be further reduced by incorporating active or passive shunt current resistors, or by installing lengthy conduit sections between the block groups. For instance, conduits spanning two to three meters between groups of blocks might be adequate to diminish shunt currents to a tolerable level. Typically, flow battery electrolytes exhibit a quantifiable electrical resistance for each unit length of conduit with a specified cross-sectional area. The necessary length of conduit to lower shunt currents

to an acceptable degree can be determined using Ohm's law and the known resistance per unit length. In certain scenarios, shunt currents might be lessened as a proportion of the stack's output power; for example, a reduction to less than approximately 1% of the total stack power could be considered sufficiently minimal. Alternatively, shunt currents may be decreased to nearly zero if feasible, while adhering to other limitations. Blocks operating at uniform voltage levels can be grouped by either physical proximity or by fluidic coupling to reduce the magnitude of voltage drops across conduit segments. Although grouping blocks of a similar type in close physical proximity can help cut down on material costs, such grouping is not absolutely necessary. Moreover, while blocks within a common group are depicted as being electrically connected in parallel, they may also be organized into separate series, with one or more blocks of each type per series.

Thanks to the analysis of this patent, it is evident that in industrial-scale applications of VRFBs, the connection and configuration of different stacks must be carefully evaluated for each specific case, as voltage differences can amplify shunt currents.

Patent US20120202127A1 by Friesen et al. [38] proposes a cell system with integrated shunt current interruption methods. Figures 5.38, 5.39 and 5.40 offer a detailed view of the system:

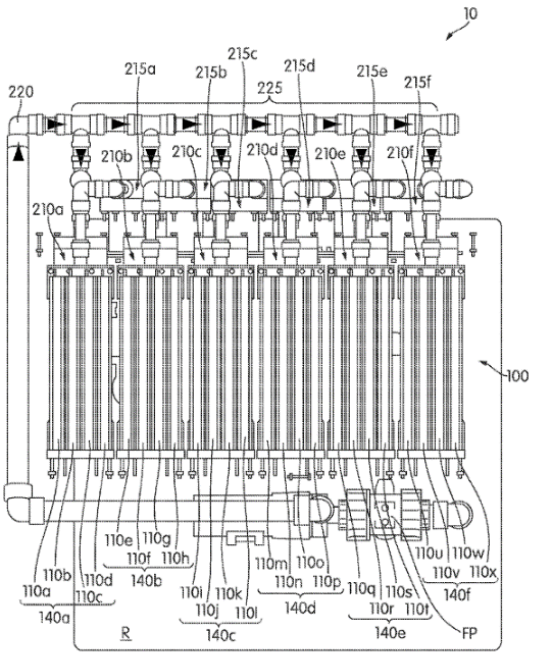

Figure 5.38: Analyzed electrochemical cell system [38]

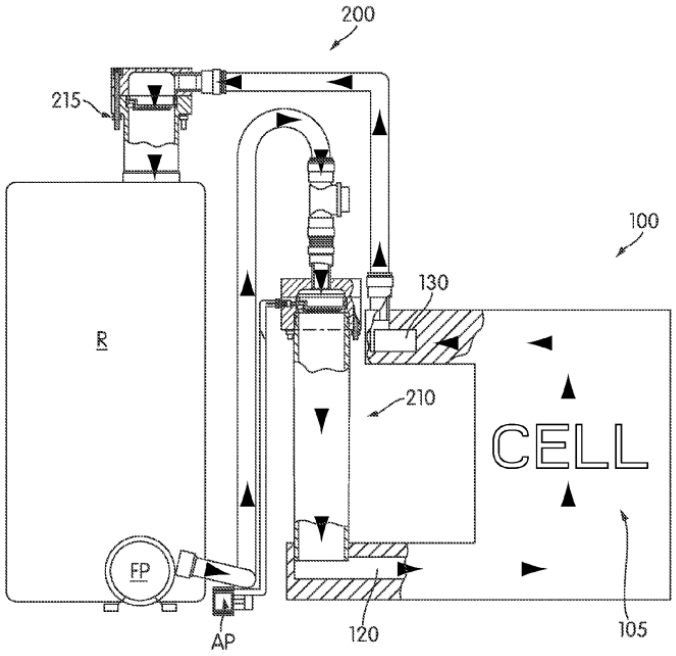

Figure 5.39: Scheme highlighting the cell module and the disperser system [38]

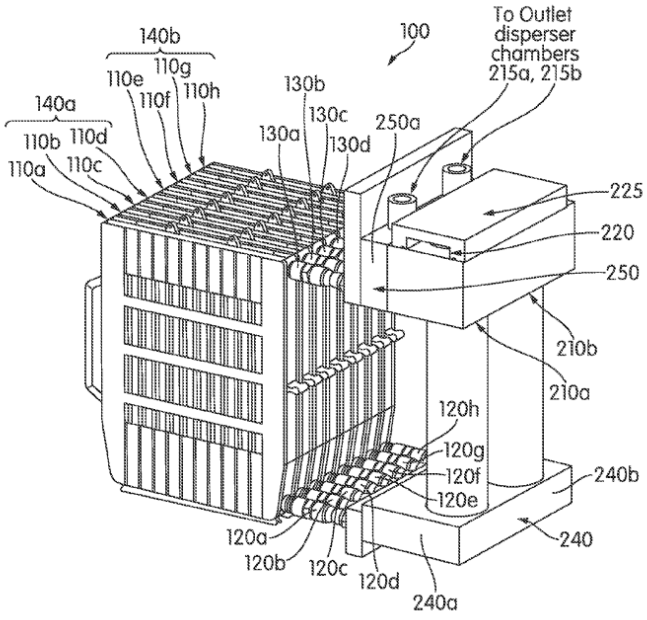

Figure 5.40: External perspective of the cell module and the disperser system [38]

The ionically conductive medium can produce shunt currents due to its electrical conductivity as it passes through multiple cells, labeled 105. These parasitic currents move within the cell system, transferring between electrodes of different cells, which results in a decreased overall potential difference across the cell module, denoted as 100. Interrupting the shunt current can be accomplished by physically isolating the ionically conductive medium, severing the detrimental electrical connections and establishing a level of current isolation. To this end, the cell system, designated as 10, integrates a flow disperser system, numbered 200, to facilitate this separation. The flow disperser system comprises an inlet disperser chamber, labeled 210 designed to disperse the ionically conductive medium's flow before it enters the cell module via the cell inlet and an outlet disperser chamber, tagged as 215 to disrupt the flow after it exits the cell module through the cell outlet. While some embodiments may include either the inlet disperser chamber or the outlet disperser chamber, having both is beneficial since shunt current can be bi-directional, making current isolation on both sides of the cells in the ionically conductive medium's flow path advantageous. While shunt current may still occur between cells within a bicell, numbered 110 or a set, its impact is most significant between the first and last cells in the cell module. To more effectively prevent shunt current, some embodiments may consider the use of inlet manifolds and outlet manifolds, like the ones in figure 5.40, allowing each cell or bicell to have its own inlet disperser chamber and/or outlet disperser chamber. Alternatively, a minimal level of shunt current might be acceptable, and the disperser system could include as few as one inlet disperser chamber and/or outlet disperser chamber to mitigate shunt current between the series' first and last cells in cell module. The configuration of bicells, as well as the association of multiple cells with each inlet and outlet disperser chamber, is optional and not restrictive. Consequently, cells or bicells can be fluidly connected in series, parallel, or a combination of both. The design of cells or bicells aims to minimize current leakage to an acceptable level. For series-connected cells, a serpentine path featuring a high-resistance electrolyte can be used, whereas modules with parallel-connected flow might use inlet and outlet disperser chambers to achieve isolation. Located beneath the lower section of the pre-dispersal chamber, there may be a disperser, labeled 300. This disperser could be designed to fragment the flow of the ionically conductive medium into a shower or spray. The purpose is to disrupt any electrical connections, such as shunt currents, that are formed within the ionically conductive medium by the separation between the individual droplets.

This patent was included in the study since it provided a visual and concrete implementation of many features seen in previous patents in one system.

Although patent US11973254B2 by Su et al. [39] main subject are aqueous polysulfide-based electrochemical cells it proposes a specific configuration to connect different stacks, as shown in picture 5.41:

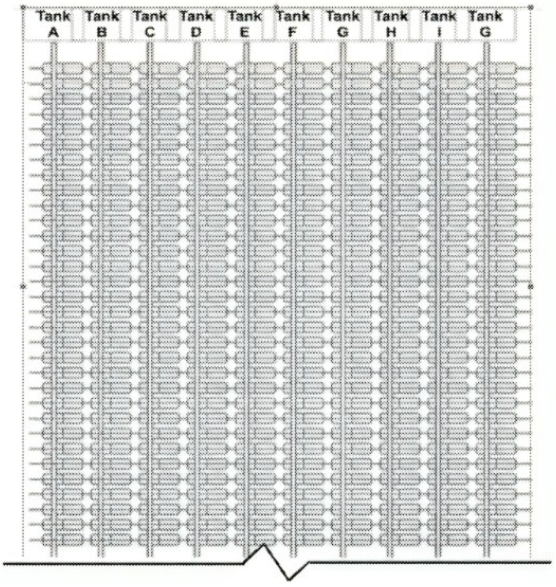

Figure 5.41: Schematic representation of connections, with a stack having multiple tanks connected [39]

In conventional flow battery systems, a tank containing catholyte or anolyte is linked to a stack of electrically connected cells, which can lead to shunt currents in the electrolyte conduit due to the movement of the electrolyte. These shunt currents can decrease system capacity by causing electrical discharge of the electrolyte components. The new electrolyte manifold design detailed here seeks to reduce or prevent the occurrence of shunt currents. As illustrated in the accompanying figure, each anolyte tank supplies cells at identical positions across different stacks. Cells in series within a stack do not share electrolyte from the same tank. Figure 5.41 depicts a flow battery system designed to mitigate shunt currents, as per various embodiments described herein. Referring to figure 5.41, the system comprises columns of flow cells connected to individual electrolyte tanks labeled A-G. Cells adjacent to each other in different columns may be electrically connected in series or parallel, meaning they are fluidly connected by column and electrically by row. Thus, the cells electrically connected in each row receive electrolyte from the different tanks A-G. This configuration ensures that the cells in each row do not share electrolyte from the same tank A-F, minimizing the generation of shunt currents. While not depicted, the electrolyte discharged from each cell column can be channeled back to its respective tank A-G, or to one or more separate tanks.

The solution proposed, in the case of VRFB would drastically increase the costs and bulk of the overall system, therefore, although such solution might be useful for experimental devices, it is not feasible in industrial applications. However, the idea of implementing multiple tanks, instead of just two, like in the classic configuration, might be of inspiration for future development.

Patent DE102020122478B4 by Holger Fink [40] provides a specific cell stack structure and compositions which has some benefits, one of them being the reduction of shunt currents. To integrate the various flow openings with a fluid system or an external reservoir, the openings are ideally linked to a fluid distributor. This distributor may be a plate produced through injection molding or milling or a thermoformed component. For instance, the distributor plate might feature a multi-layered design with primary and secondary channels for the electrolyte, independent of the cell stack, and possibly comprising multiple individual plates. The distributor plate might be designed with an open side, enabling the cell stack's outer wall to seal off the secondary channels. The thermoformed component could include multiple channels that connect, at least in part, to the flow openings. Alternatively, the fluid system could take the form of a pipeline network of any size, with its free ends affixed to the cell stack's outer wall, the distributor plate, or the thermoformed component. The fluid distributor's channels are narrow in diameter but long, increasing the electrical resistance within the fluid columns to prevent the creation of shunt currents, thereby enhancing the battery's efficiency and longevity.

The fluid distributor is ideally welded to the cell stack's outer wall, eliminating the need for additional sealing. For example, when the fluid distributor is a distributor plate, it may be mounted to the outer wall over a broad area. This alignment of the distributor plate's flow channels with the flow openings facilitates the movement of the electrolyte from the distributor plate into the reaction cavity, or the reverse. If the fluid distributor is a thermoformed component, it will have a design at its end near the flow opening that facilitates a watertight weld to the cell stack's outer wall. This freedom in design allows for optimal cascading, combining flow channels or designing flow ducts to significantly suppress shunt currents with minimal hydraulic losses. Moreover, this reduces corrosion stress from shunt currents, enhancing the service life. Additionally, the substantial shunt current suppression by the external fluid distributor, positioned outside the cell stack and especially beyond the cell frame elements, enables the technical realization of a high-voltage stack exceeding 100 V, ideally over 500 V, and more preferably over 1000 V, potentially reducing the need for power electronics.

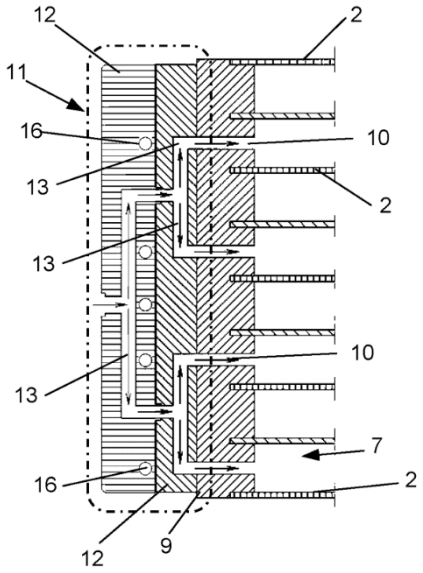

Figure 5.42: A representation of the cell stack with an attached fluid distributor [40]

The fluid system's design allows for the creation of four distinct fluid circuits within a single distributor for both electrolytes, ensuring efficient flow and return. This setup guarantees that cells from two or more cell stacks, electrically connected in parallel, are also interconnected. The fluid system's design and dimensions are tailored to reduce shunt currents, thus expanding the effective reaction area and boosting efficiency by reducing losses from these currents. Figure 5.42 depicts a fluid distributor, identified as item 11, firmly affixed to the outer wall, item 9, to guarantee a watertight seal. The fluid distributor consists of two plates, item 12, which are outfitted with flow channels, labeled 13. The plate-shaped fluid distributor is affixed to the cell stack's outer wall, labeled 1, aligning its flow channels with the flow openings, numbered 10, using methods such as laser, infrared, heating element, or ultrasonic welding. The fluid distributor is designed with comparatively lengthy flow channel lengths and narrow flow channel cross-sections to diminish shunt flow. Additionally, fluid distributor may include one or more circuits for various electrolytes, each equipped with a designated flow and return path.

5.7 Personal suggestions

All the analyzed patents offered insights on how to minimize shunt currents, offering food for thought. That is why this paragraph presents personal suggestions. The first developed design is an improved shower head, developed considering pumping losses due to pressure drops. The concept has, compared to a classic shower head, an increased pathway of the flow and

reduced pressure drops, due to the featured shape. The device is easy to implement and easy to manufacture.

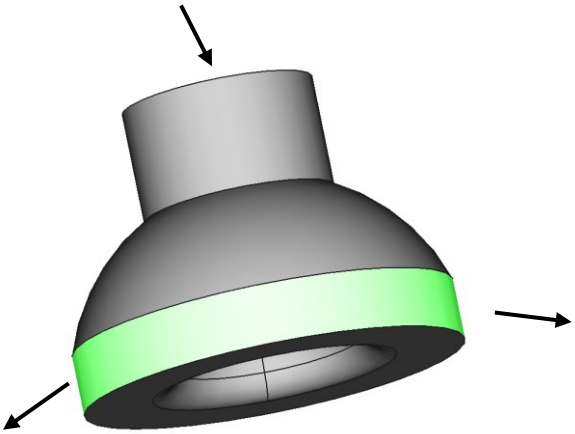

Figure 5.43: Shower head “bell” shaped

Figure 5.43 shows the shape of the suggested shower head, and the highlighted green ring is where the holes are located. The holes can be of any shape, whether circular, rectangular, like in figure 5.44, or any other shape.

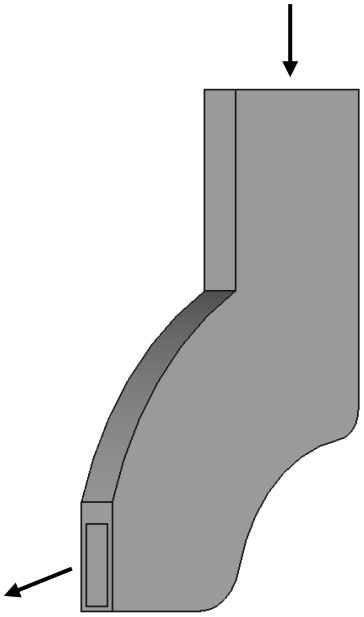

Figure 5.44: Cut plane view of the device, featuring a rectangular hole

Inside the shower head, flaps could be implemented to guide the flow, reducing the pressure drops in proximity to the holes. However, such a feature would increase the complexity of the device. Such location of the holes allows to have a parabolic flow instead of a vertical one, increasing the disruption of shunt currents, as demonstrated in figure 5.45:

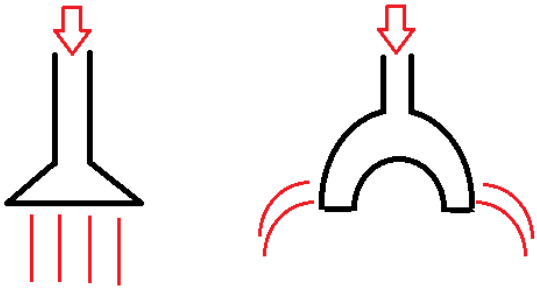

Figure 5.45: Different flow paths for the different designs

A simulation on SimScale was performed to visualize the pressure difference between the two designs. The considered liquid was water (entry velocity of 0.5 m/s).

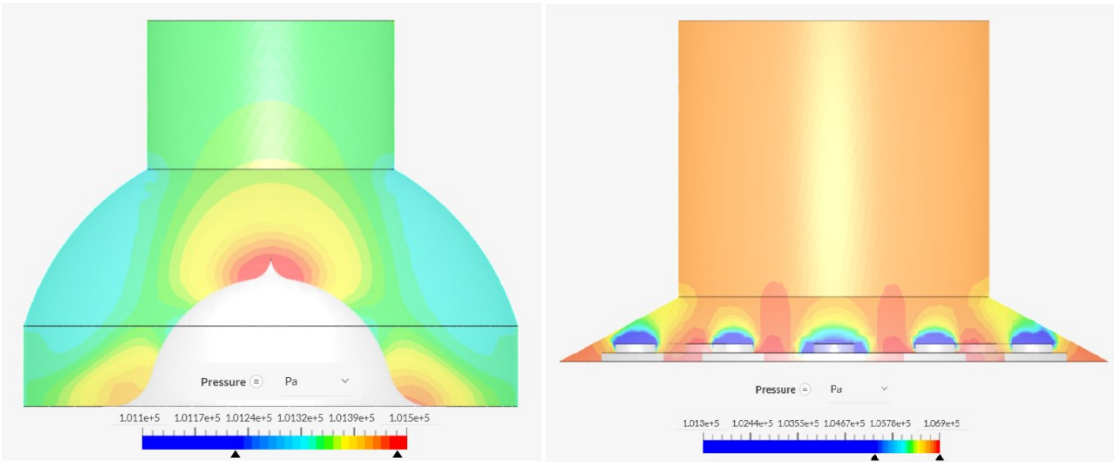

Figure 5.46: Pressure analysis for the compared designs

As mentioned above, pressure drops are more marked in the classic shower head, whereas in the suggested design the pressure drops are reduced.

Another idea is a simple circular device that can be implemented in the pipes to reduce shunt currents in stand-by conditions. The device is presented in figure 5.47:

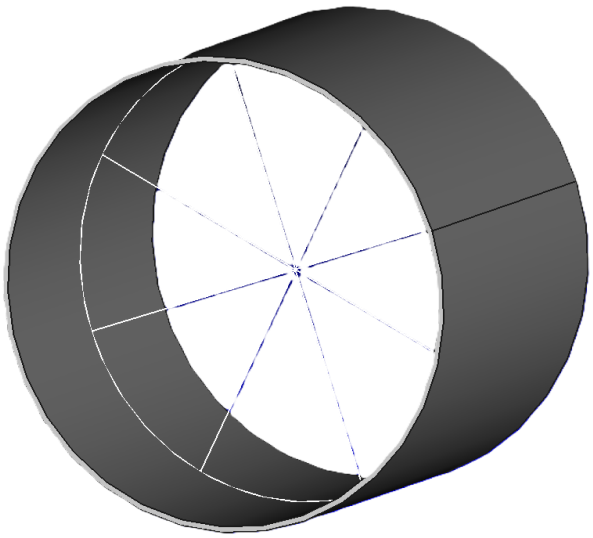

Figure 5.47: Design featuring 8 flaps (transparent for clarity) composing a valve

This device works like a heart valve, it is composed of multiple flaps that during normal operation of the VRFB leave the pathway open, whereas during standby conditions close the pathway. The flaps can be either elastic or rigid, the latter need a spring to return to the initial position. The flaps must be materials that are chemically resistant to acidic vanadium electrolyte solutions. The device is further explained in figure 5.48:

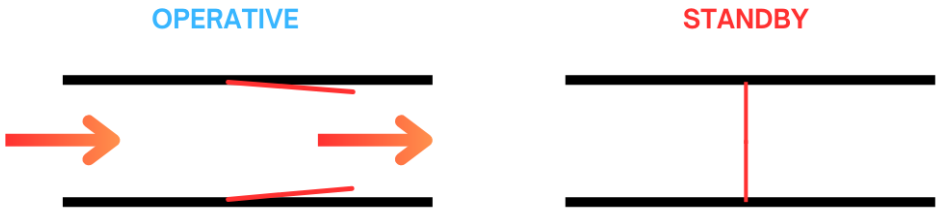

Figure 5.48: Flaps position depending on the different states of the VRFB

The drawbacks of such a device are increased pumping losses during startup due to the electrolyte's flow encountering initially the closed flaps and possible leakages in between the flaps during standby. A solution to this last problem could be to implement a second layer of flaps with a different angulation. The advantages of this device are its simplicity and easy implementation.

6. Conclusion

The objective of this thesis is to investigate shunt currents in flow batteries (FBs) and to identify effective solutions for mitigating their impact on battery efficiency. Shunt currents, which are parasitic electrical currents that flow into the internal hydraulic path in a FB, can significantly affect the performance and efficiency of FBs. This study delves into many aspects of shunt currents, examining their generation, behavior, and the subsequent consequences they pose for battery design and operation.

To achieve this, a thorough review of various scientific literature was conducted, providing a solid foundation of existing knowledge on the topic. This literature review was complemented by an in-depth analysis of relevant patents and commercial solutions, aiming to identify viable solutions for mitigating shunt currents. These solutions range from simple, straightforward devices to more complex and innovative technologies. Each patent was scrutinized in detail, assessing not only the proposed methods for shunt current mitigation but also their practical applicability in industrial applications.

A key finding of this research is the critical need to establish a break-even point between pumping losses and shunt current losses. Typically, an increase in resistance to shunt currents correlates with an increase in pumping losses, which can undermine the benefits of mitigation strategies. This delicate balance is essential for optimizing the overall efficiency of FBs, as both types of losses directly impact the performance and cost-effectiveness of the battery systems.

Through the analysis of various patents, this thesis offers valuable insights into potential solutions for addressing shunt currents. By highlighting innovative approaches and evaluating their practicality, the research not only contributes to the existing body of knowledge but also inspires further exploration into the overall efficiency of FBs. In line with this, some new solutions proposed by the author are also described. The findings can serve as a guide for future studies focused on implementing the identified devices and strategies, ultimately advancing the development of more efficient energy storage systems based on FBs.

Bibliography

[1] International Energy Agency, “World Energy Investment 2024”, June 2024.

[2] Kim, Ki & Park, Min-Sik & Kim, Young & Kim, Jung Ho & Dou, Shi & Skyllas-Kazacos, Maria, “A technology review of electrodes and reaction mechanisms in vanadium redox flow batteries”, *Journal of Materials Chemistry A*, vol.3, n.33, pp.16913−16933, July 2015.

[3] Jungmyung Kim, Heesung Park., “Recent advances in porous electrodes for vanadium redox flow batteries in grid-scale energy storage systems: A mass transfer perspective”, *Journal of Power Sources*, vol.545, n.231904, October 2022.

[4] P. Trogadas, O.O. Taiwo, B. Tjaden, T.P. Neville, S. Yun, J. Parrondo, V. Ramani, M.O. Coppens, D.J.L. Brett, P.R. Shearing, “X-ray micro-tomography as a diagnostic tool for the electrode degradation in vanadium redox flow batteries”, *Electrochemistry Communications*, vol.48, pp.155–159, November 2014.

[5] C.H.L. Tempelman, J.F. Jacobs, R.M. Balzer, V. Degirmenci, “Membranes for all vanadium redox flow batteries”, *Journal of Energy Storage*, vol.32, n. 101754, December 2020.

[6] X. Zhao, Y. B. Kim, and S. Jung, “Shunt current analysis of vanadium redox flow battery system with multi-stack connections”, *Journal of Energy Storage*, vol. 73, December 2023

[7] A. Crawford and V. Viswanathan, “RFB Side Effects—Shunt Currents,” in *Encyclopedia of Energy Storage: Volume 1-4*, vol. 1–4, pp. 535–544, January 2022.

[8] Y. S. Chen, S. Y. Ho, H. W. Chou, and H. J. Wei, “Modeling the effect of shunt current on the charge transfer efficiency of an all-vanadium redox flow battery,” *Journal of Power Sources*, vol. 390, pp. 168–175, June 2018.

[9] C. Yin, S. Guo, H. Fang, J. Liu, Y. Li, and H. Tang, “Numerical and experimental studies of stack shunt current for vanadium redox flow battery,” *Applied Energy*, vol. 151, pp. 237–248, August 2015.

[10] F. T. Wandschneider, S. Röhm, P. Fischer, K. Pinkwart, J. Tübke, and H. Nirschl, “A multi-stack simulation of shunt currents in vanadium redox flow batteries,” *Journal of Power Sources*, vol. 261, pp. 64–74, September 2014.

[11] W. R. Bennett, M. A. Hoberecht, and V. F. Lvovich, “Analysis of shunt currents and associated corrosion of bipolar plates in PEM fuel cells,” *Journal of Electroanalytical Chemistry*, vol. 737, pp. 162–173, January 2015.

[12] F. Xing, H. Zhang, and X. Ma, “Shunt current loss of the vanadium redox flow battery,” *Journal of Power Sources*, vol. 196, no. 24, pp. 10753–10757, December 2011.

[13] S. König, M. R. Suriyah, and T. Leibfried, “Model based examination on influence of stack series connection and pipe diameters on efficiency of vanadium redox flow batteries under consideration of shunt currents,” *Journal of Power Sources*, vol. 281, pp. 272–284, May 2015.

[14] A. Trovò, F. Picano, and M. Guarnieri, “Comparison of energy losses in a 9 kW vanadium redox flow battery,” *Journal of Power Sources*, vol. 440, November 2019.

[15] H. Fink and M. Remy, “Shunt currents in vanadium flow batteries: Measurement, modelling and implications for efficiency,” *Journal of Power Sources*, vol. 284, pp. 547–553, June 2015.

[16] N. M. Delgado, R. Monteiro, J. Cruz, A. Bentien, and A. Mendes, “Shunt currents in vanadium redox flow batteries – a parametric and optimization study,” *Electrochimica Acta*, vol. 403, January 2022.

[17] A. Tang, J. McCann, J. Bao, and M. Skyllas-Kazacos, “Investigation of the effect of shunt current on battery efficiency and stack temperature in vanadium redox flow battery,” *Journal of Power Sources*, vol. 242, pp. 349–356, November 2013.

[18] A. Trovò *et al.*, “Standby thermal model of a vanadium redox flow battery stack with crossover and shunt-current effects,” *Applied Energy*, vol. 240, pp. 893–906, April 2019.

[19] Q. Ye, J. Hu, P. Cheng, and Z. Ma, “Design trade-offs among shunt current, pumping loss and compactness in the piping system of a multi-stack vanadium flow battery,” *Journal of Power Sources*, vol. 296, pp. 352–364, August 2015.

[20] Craig R. Horne, Jay E. Sha, Ronald J. Mosso, William D. Lyle, “Shunt current resistors for flow battery systems”, US20120308856A1, December 2012.

[21] Song Yongjiang et al., “Electrolyte breakover and electricity leakage prevention device of liquid flow battery pack”, CN104241665A, June 2013.

[22] Ha Tae Jeong et al., “Flow battery and battery module comprising thereof”, KR20160075923A, January 2015.

[23] Ha Tae Jeong et al., “Redox flow battery having reduced shunt loss”, KR20160075923A, January 2015.

[24] Hwei-Liang Chang, Ning-Yih Hsu, Yao-Sheng Hsu, Zone-Sure Chang, “Flow battery apparatus with shunted current repressed and method thereof”, US10826101B2, November 2020.

[25] Bradley Kell, Jon Horner, Rick Winter, “Systems and methods for shunt current and mechanical loss mitigation in electrochemical systems”, US10074859B2, September 2018.

[26] P. A. Prieto-Díaz, A. A. Maurice, and M. Vera, “Measuring density and viscosity of vanadium electrolytes: A database with multivariate polynomial fits,” *Journal of Energy Storage*, vol. 94, July 2024.

[27] Qianzhao Jiantai et al., “Redox flow battery tube, method for manufacturing redox flow battery tube, tube unit, and redox flow battery”, CN109155422B, October 2021.

[28] E. N. Balko and L. C. Moulthrop, “Reduction of shunt current in bipolar electrochemical cell assemblies”, GB2085475A, August 1981.

[29] Thomsen et al., “High performance redox flow battery stack”, US10381667B2, August 2019.

[30] Chou et al., “Method of fabricating bipolar pate flow cell”, US20170229715A1, August 2017.

[31] Jo Beom Hui et al., “Redox flow battery for reducing shunt current”, KR101742980B1, May 2017.

[32] T. Kanno et al., “Frame body, cell frame for redox flow cell, and redox flow cell”, JP2017041452A, February 2017.

[33] Y. Hanye et al., “Frame body, unit frame for redox flow battery, and redox flow battery”, TWI678020B, November 2019.

[34] K. Yano et al., “Cell stack and redox flow battery”, JP5831747B2, November 2015.

[35] J. Cheng et al., “Current breaker for shunt current of flow battery”, CN201383523Y, September 2008.

[36] Seong Mun Ja et al., “Redox flow battery having a function of preventing shunt current and leakage”, KR102161420B1, October 2020.

[37] J. Sha, B. Lin, “Redox flow battery system configuration for minimizing shunt currents”, WO2014145788A1, September 2014.

[38] C. A. Friesen et al., “Electrochemical cell system with shunt current interrupt”, US20120202127A1, January 2012.

[39] L. Su et al., “Aqueous polysulfide-based electrochemical cell”, US11973254B2, January 2020.

[40] H. Fink, “Cell stack with one cell and method for producing a cell stack”, DE102020122478B4, March 2022.